Collective Behaviour of Chemotactic Microorganisms in a Viscous Environment

Anatolij Gelimson

Balliol College

University of Oxford

A thesis submitted for the degree of

Doctor of Philosophy

Trinity 2016

Acknowledgements

First, I would like to express my deepest gratitude to my supervisor, Prof. Ramin Golestanian, for his guidance and support throughout my Master's and DPhil. I am more than lucky to have had him as my DPhil advisor and I could always count on his support and advice. Not only did I benefit from his helpful ideas, but also from his generous help in every aspect of research (like funding applications, conferences and seminars). Writing this thesis, there were times of breakthroughs and times of frustration, and I could count on him in both.

My DPhil was funded by the Ernst Ludwig Ehrlich Studienwerk PhD Scholarship and by the EPSRC DTA Scholarship. It was due to their generous – both financial and intellectual – support that I was able to pursue my DPhil.

I greatly enjoyed working with Dr. Till Kranz on the autochemotaxis paper and I am grateful for our mutually beneficial collaboration on the Pseudomonas project. He is kind and fun to work with and his comments on the work were always on point.

I also would like to thank our experimentalist colleagues from UCLA, in particular Dr. Kun Zhao, Prof. Gerard Wong and Calvin Lee. They supplied us with experimental data, clarified questions and misconceptions and even re-ran some experiments. Their great understanding of the experimental system helped make our theories better, their insights were invaluable for my work and our publications. They also helped me and Ramin find the right tone of the paper, to make sure that we capture the interest of a broad audience, both in the theoretical and experimental community.

I am grateful to my colleagues, former colleagues and office mates for the time we had together. I would like to thank Dr. Jack Cohen, Dr. Abhishek Chaudhuri, Dr. Douwe Bonthuis, Dr. Agnes Noy, Dr. Rachel Bennett, Mira Zorkot, Dr. Pierre Illien, Dr. Mitya Pushkin, Dr. Arnold Mathijsen and Matthew Andrew for the time we spent together during College lunches, seminars, conferences and pubs.

I give my deep and heartfelt thanks to the love of my life, Sara, who is always there for me and believes in me. I am incredibly grateful to have her in my life. Her love,

encouragement and kindness bring me joy every day. My family, and in particular my mother, has always been very supportive of my decision to pursue a DPhil and helped me where they could, be it by taking some non-physics-related duties from me, by providing a place to stay over the summer or just by providing moral support. Sara's family has welcomed me as one of their own and they have been loving and kind in every way. My College has been a place where I have found many good friends and I loved being part of it. My friends have been there for me throughout these years and I would not do anyone justice by highlighting them, but I would like to highlight Chai, Bud and Chashka – Chashka has been very timid in expressing his scientific opinions but Chai's contributions were vocal and manifold. Bud's love for carrots inspired me to look at (somewhat) carrot-shaped Pseudomonas Aeruginosa bacteria and his comments were always spot-on.

Abstract

The aim of this DPhil thesis is the investigation of collective effects that can occur in a colony of interacting bacteria. The non-equilibrium dynamics of living organisms can lead to fascinating patterns and behaviours which cannot be found in equilibrium systems. It is our goal to obtain a better understanding of bacterial colonies and to develop a general theoretical description for living systems undergoing chemotaxis.

Some types of bacteria are able to release chemical attractants to their environment, which enables them to sense each other and to form biofilms in a coordinated way. *E. Coli*, for example, secrete aspartate if succinate is present, which diffuses in their environment and enables interactions. In the first part of the thesis we will derive a general model for bacteria or cells that interact with each other via chemotaxis and also undergo divisions. Using Renormalization Group calculations we will show that division and chemotactic terms are of the same relevance, and that the competition between them can lead to a rich phase diagram and a transition from controlled behaviour to uncontrolled growth.

In the second chapter, we will examine microorganism interaction in the limit where the secreted particles are effectively non-diffusive. On a surface, *Pseudomonas aeruginosa* bacteria leave a trail of polysaccharides behind them, which is followed by other P. aeruginosa bacteria [1, 2]. These interactions between individuals can lead to a local accumulation and spatial correlations of bacteria [3, 4], which are important at the early stages of the biofilm formation. Starting with a generic single microorganism, we will derive the underlying equations of motion. As an important qualitative feature, we will obtain trail alignment with the gradient in addition to a trail-dependent velocity in conventional chemotaxis. Using a simplified version of the model, we will analytically investigate the effects of autochemotaxis with a self-deposited trail and show that it can lead to enhanced rotational diffusion and even trapping. However, if a microorganism is following an existing trail, it can also lead to oscillatory behaviour and to perpendicular trail escapes. We will then compare the full model to experimental results and find that it can both explain

single-bacteria behaviour and collective microcolony formation of P. aeruginosa. The collective polysaccharide distributions can also be understood within the framework of a simple calculation inspired by network theory, which gives surprisingly good results.

Contents

Chapter 1

Introduction

1.1 Pattern Formation and Chemotaxis

The study of pattern formation in active systems has recently been subject to extensive research, due its importance for living organisms and due to the fascinating effects only seen in such systems [3, 5–11]. Studies include the behaviour of suspensions of active filaments [12, 13], the polar and nematic ordering of self-propelled rods [14, 15], thermally active colloids [16], as well as chemotactic pattern formation in living systems [3], following experimental observations [5, 6].

Microscopically seen, the variety of propulsion mechanisms is very large, and yet macroscopic pattern formation often depends on very generic symmetries and rules – it shows universality for large lengthscales [9, 10, 17–21]. This is best illustrated by the universal quantitative theory of flocking derived by Toner and Tu, who coarse-

grained short-range interactions between the individual active particles ("birds") into an active hydrodynamic model [18].

Coarse-grained hydrodynamic theories for active colloids have been shown to apply to a whole variety of – seemingly unrelated – collective phenomena in biology, like flocks of birds, schools of fish or aggregations of molecular motors [17–24]. For example, *E. Coli* bacteria are known to explore attractants in their environment using a run-and-tumble strategy that couples to a chemical sensing mechanism, which feeds back on the rotation of flagella motors [25–28]. The complex underlying mechanisms have been extensively studied in previous literature [29]. And yet, on a coarse-grained level, such a motion can often be just modeled as directed mobility in response to a chemical gradient [3, 30, 31].

In chemotaxis the interactions between individual microorganisms are typically of a long-ranged nature – diffusion of emitted nutrients or chemicals in an aquaeous solution leads to a long-range chemical concentration gradient, which attracts or repels other bacteria [32]. This mechanism for long-range interactions is known to play an important role at the early stages of bacterial biofilm formation [4, 8, 33]. In addition to this, pattern formation is often also influenced by growth and death processes [34, 35]. A general investigation of the interplay of long-range chemotactic interactions and growth-death processes could provide interesting insights into cellular tissues and biofilm dynamics.

On a solid surface and in the limit of a slowly-diffusing chemoattractant, on the

other hand, chemical trail depositon effectively introduces a memory of previously visited spaces into the system. The opportunistic pathogen *Pseudomonas aeruginosa*, for example, secretes the exopolysaccharide Psl on surfaces [1,2]. The Psl trails promote surface attachment [2] but they also act as an attractant for other P. aeruginosa bacteria and have been shown to be crucial for aggregation in the early stages of biofilm formation [1]. Bacteria tend to follow Psl trails of other bacteria, which, due to their own Psl deposition, constitutes a self-feedback mechanism. In this way, some surface sites will be much more frequently visited than others – a "rich get richer" mechanism which results in a power-law distribution of visit frequencies per surface site [1]. The frequently visited sites then become the places of microcolony development [1].

1.2 Scope of This Work

In this thesis we will briefly review of central concepts of bacterial motion and chemotaxis. Following that, we will study the effects of chemotaxis in the case of fast-diffusing chemicals interacting and a system of dividing (cancer) cells or bacteria. For this study, we have used Dynamical Renormalization Group methods [36], which we will briefly introduce. As an important result, we will find an abrupt transition between a phase of limited chemotaxis and growth and a phase of uncontrolled growth and death processes.

In the third chapter we will study the motion and formation of microcolonies for

bacteria depositing slowly-diffusing chemotactic trails on a surface. Based on recent experimental results, we will start by deriving the stochastic equations of motion microscopically and then analyse the equations for the motion of a single bacterium. As important behaviours of surface-mediated motion we will find oscillations, enhanced rotational diffusion and run-and-tumble behaviour. We will discuss the theoretical angle distribution and show agreement with experiments on a single-particle level.

We will then go over to the collective case of microcolony formation. In agreement with experiments, we will show that the trail-following mechanism collectively leads to a rich-get-richer behavior characterized by the power-law structure of bacterial surface coverage. We will show that the same parameters extracted from the single-bacteria experiments can also reproduce the experimental collective microcolony formation, suggesting that trail alignment is the central mechanism for accumulation in P. aeruginosa. To better understand the origin of the rich-get-richer alignment we will then study the mechanism using methods from network theory and confirm that preferential visits are sufficient to explain the collective experimental power-law distributions.

1.3 Significance and Basic Concepts of Chemotaxis

Chemotaxis is the ability of cells and microorganisms to bias their motion apparatus in reaction to chemicals in the extracellular environment [37]. Depending on the organism, it can be evolututionarily favourable to move towards a higher substance

concentration (chemoattractant), or to avoid a different substance as much as possible (chemorepellent). Often, in aqaeous environments, chemical concentration gradients are very low and difficult to sense along a bacterial length scale of just a few microns [37]. To overcome these difficulties, bacteria and cells often use a complicated system of membrane receptors and signalling feedback to sense and react to temporal changes in concentration [37, 38].

As an example, in absence of chemoattractants/repellents, E. Coli bacteria explore their environment by alternating periods of directed motion (runs) and rapid changes of direction (tumbles) [25, 37]. Chemical stimuli, however, induce complex biochemical cascades [fig. 1.1], which feed back on the function of the flagellar swimming apparatus. Attractive chemicals in the environment enhance counterclockwise flagellar motion, thus favouring runs, whereas repulsive chemicals enhance clockwise motion and fast directional changes (tumbles) [38].

Chemotactic mechanisms allow microorganisms to explore their environment and bias their motion in response to signaling molecules, effectively constituting a gradient-following mechanism [30, 38]. Importantly, however, chemotaxis is also a pivotal mechanism for the formation of patterns like biofilms [25], i.e. dense aggregates of microorganisms which often adhere to each other, as well as to surfaces, via extracellular polymeric substance [39]. Chemotaxis is a fundamental mechanism of bacteria and cells and a deeper, more generic understanding of collective effects could be of utmost significance in medical research and industry [38, 40], as it might allow for better predictions of patterns as well as new methods to promote desirable pattern

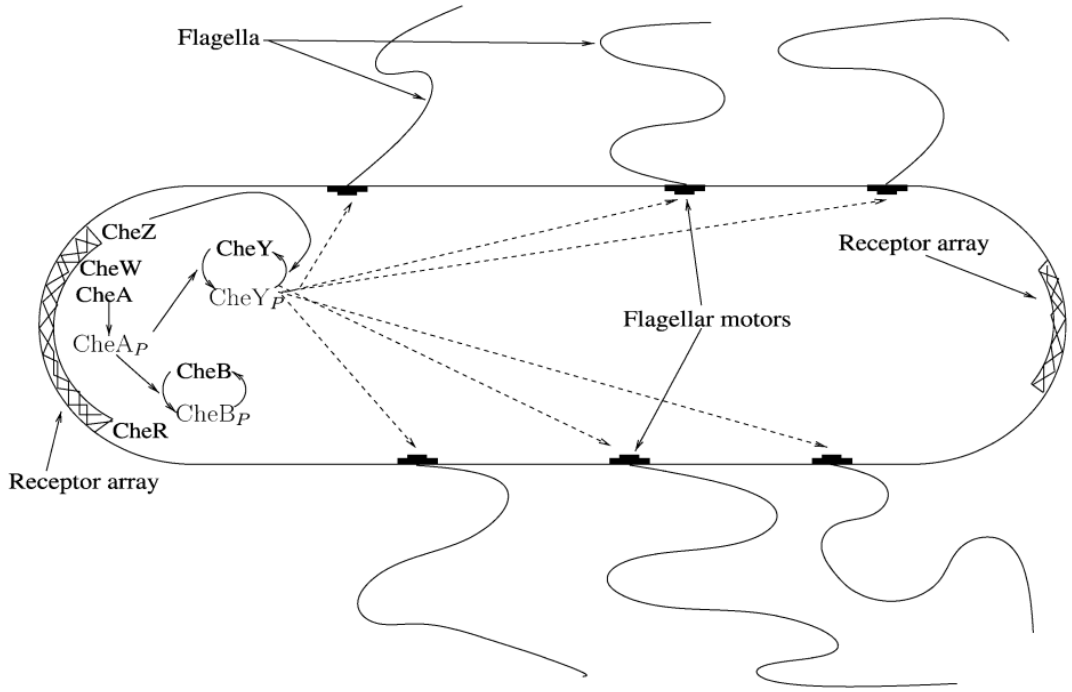

Figure 1.1: Schematic illustration of E. Coli signaling cascades, taken with permission from [38]. If a chemoattractant is absent, or if a repellent is present in the environment, CheA autophosphorylizes. The phosphorylation is transfered to CheY, which promotes clockwise rotation of the flagella, leading to tumbling. CheR and CheB control the methylation of the receptors and they are in a dynamic equilibrium in absence of an attractant gradient. In the presence of a chemoattractant gradient CheA autophosphorylation is suppressed, which suppresses CheY phosphorylation and favours counter-clockwise flagella rotations leading to chemotactic runs. Methylation of the receptors re-activates the CheA autophosphorylation, thus re-setting the system to the pre-stimulus state [38]. The E. Coli signaling framework is an example of how motion in response to a gradient is realised in nature. Taken with permission from [38]

formation and disrupt undesirable aggregations.

1.4 Dynamical Renomalization Group Methods

Chapter 2 of this thesis will apply Dynamical Renormalization group methods [36,41] to study the long-range and large-time properties of a solution of dividing chemotactic cells or bacteria.

Dynamical Renormalization groups provide methods to analyze the infrared (large-scale) and long-time behaviour of physical systems [36, 41] near a phase transition point. Two generic notions are of central importance here: universality and scale-invariance.

Universality is the observation that, on a large scale, complex systems often exhibit similar patterns, which are dependent on fundamental symmetries rather than on interaction details. Often, complex details of interaction (like run-and-tumble behaviour coupled to the flagellar apparatus in E. Coli), when observed over larger and larger scales, do not need to be taken in consideration as much as the emergent behaviour (like directed motion towards/away from a gradient) that they produce. Mathematically, the observation of systems on larger scales corresponds to integrating out smaller scales in the equations of motion, as a result of which complex equations with many interaction details can often be reduced to few fundamental equations [36, 41, 42].

Related to this, scale-invariance signifies the absence of a defining length- or time-scale of a system, such that a system looks similar to its coarse-grained self. Close to a continuous phase-transition point in a statistical system one observes a divergence in characteristic length-and timescales, where the divergence is dependent on control parameters via a characteristic power law [41]. As an example, in the Ising model for dimension $d \geq 2$ one observes a continuous transition between a disordered phase with a finite correlation length between spins (i.e. a finite size of a magnetic domain) to a phase where the spins are aligned with each other over the whole systems length, controlled the temperature T. At the phase transition point itself, the correlation length behaves as $\xi \sim |T - T_c|^{-\nu}$, where T_c is the critical temperature and ν is a dimension-dependent critical exponent. Under the assumption of scale-invariance near a phase-transition point, the phase diagram structure can be studied by observing the change (flow) of coupling constants under continuous rescaling. Of particular interest are fixed points in the flow, points at which coupling constants do not change, which could indicate a phase separation or a stable phase with often non-trivial critical exponents [36, 41, 42].

In chapter 2 we will derive an equation for the collective chemotaxis of dividing cells or bacteria and then apply the Dynamical Renormalization Group method as outlined by [41], by Fourier transforming the equation and (1) coarse-graining integrating out large wavelengths $|\mathbf{k}| \in [e^{-\ell}\Lambda, \Lambda]$ (with Λ as the highest momentum of the Brillouin zone and $e^{-\ell}$ a scaling factor), which modifies the coupling constants of the equation, (2) re-scaling the resulting equation by re-scaling the momenta $\mathbf{k} \to \mathbf{k}e^{-\ell}$

and (3) finding conditions under which coupling constants are fixed and analyzing the flow around them to make statements about the phase structure and critical exponents [41].

Chapter 2

Long-range and large-time interactions in dividing chemotactic cells

2.1 Introduction

The generic biological mechanism of chemotaxis is of crucial importance in a wide variety of biological processes, including cancer growth [43], wound healing and embryogenesis [44]. On a coarse-grained level, chemotaxis has successfully been modelled as directed motion towards (or away from) a chemical concentration gradient [30]. One known effect found on this description level is the chemotactic collapse of a cell population due to a self-generated attractive chemical concentration field [30, 45], similar

to a gravitational collapse in self-gravitating Langevin particles [46, 47]. Other than in many popular hydrodynamic theories for flocking [18, 22, 48], chemotactic interactions are of a long-range nature since the diffusion of chemoattractants/repellents by the cells leads to a power-law decay of the chemical concentration field [49]. In addition to that, number conservation in general does not hold due to birth and death events of cells, which can have a profound effect on the collective behaviour [34, 49]. This chapter, which is based on the results of Gelimson and Golestanian published in Physics Review Letters [49] will discuss the interplay of chemotaxis and growth/death processes.

2.2 Model Equations

A schematic representation of our model is shown in fig. 2.1 and [49]. Each cell releases chemicals and thus creates a long-range concentration field $\phi(\mathbf{r}, t)$ [49] around them [see fig. 2.1 (a)]. Other cells will sense the gradient $\nabla\phi(\mathbf{r}, t)$ and move towards increasing concentrations (or towards decreasing concentrations if the secreted chemicals are chemorepellents). As an approximation we will assume that the response in motion is linear with respect to $\nabla\phi(\mathbf{r}, t)$ [49]. In addition to that, in a microscopic environment, each cell is subject to fluctuations in motion, which we will model as Brownian. In a dissipative environment where inertial effects are negligible, the single-bacterium equation reads [49]:

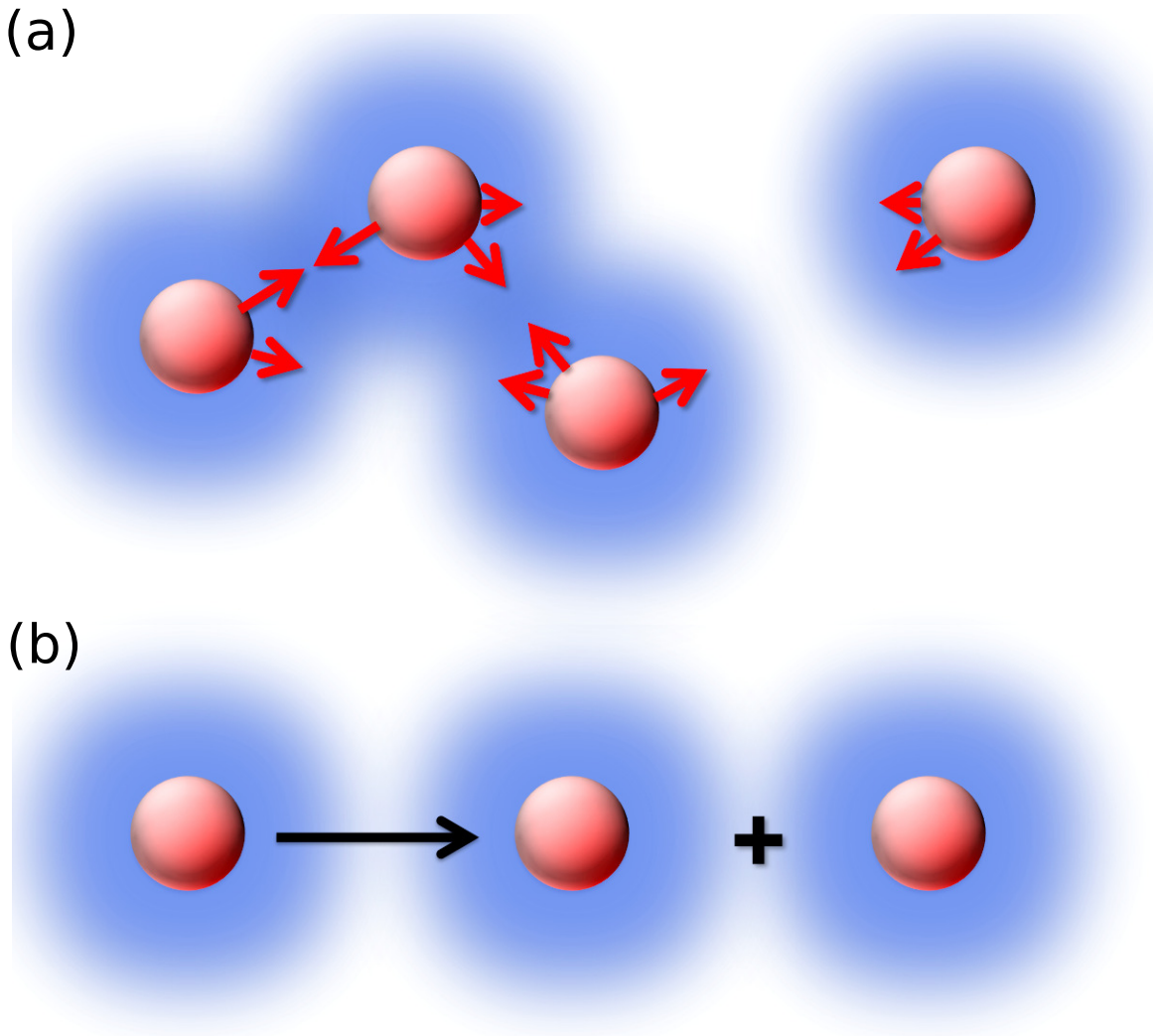

Figure 2.1: Model schematics: (a) cells secrete chemicals into their environment, and thus create a long-range concentration field of chemicals (blue). The cells effectively interact via the created chemotactic field (red arrows). (b) in addition, they also undergo cell division and death processes, such that their number is not conserved. Taken with permission from [49]

$$\partial_t \mathbf{r}_i = -\mu \, \nabla\phi|_{\mathbf{r}=\mathbf{r}_i(t)} + \sqrt{2D}\eta_i(t) \tag{2.1}$$

where μ is the mobility coefficient of the cell, which is positive in case of a chemorepellent and negative in case of a chemoattractant.Its unit is [length]$^{2+d}$/[time] in d dimensions [49].

In general, the constants μ and D are determined by microscopic details of the chemotactic motion and do not obey the Fluctuation-Dissipation theorem for equilibrium systems [50] because living systems are open systems with non-thermal behaviour, like feedback between flagella and chemical pathways. However, as [50] have shown, the more general Fluctuation-Response Theorem applies to those systems, that is the chemotactic response and correlation function of a spontaneous excitation are linearly related via a constant that may depend on genetic background, functional details and growth conditions [50].

The chemical secreted by a single bacterium i obeys a diffusion equation with a source term, $\frac{1}{D_{\text{chem}}}\partial_t\phi_i = \nabla^2\phi_i + \alpha_0\delta\left(\mathbf{r} - \mathbf{r}_i(t)\right)$, where α_0 is the chemical release rate, normalized by the diffusion constant D_{chem}. In the case of many cells releasing chemicals, the equation for the chemical concentration would read $\frac{1}{D_{\text{chem}}}\partial_t\phi = \nabla^2\phi + \alpha_0 C(\mathbf{r}, t)$, where $C(\mathbf{r}, t) = \sum_i \delta\left(\mathbf{r} - \mathbf{r}_i(t)\right)$ is the density of cells. In our analysis we will be interested in the long-time behaviour of the system. And due to the small size of the released chemicals compared to the cell size, we can assume that ϕ adapts to changes in $C(\mathbf{r}, t)$ very fast. For this limit we will neglect $\partial_t\phi$ and hence the field of

chemicals ϕ will effectively act as a Coulomb-like potential [49]: $-\nabla^2\phi = \alpha_0 C(\mathbf{r},t)$ or

$$\phi = -\frac{1}{\nabla^2}\alpha_0 C(\mathbf{r},t) \tag{2.2}$$

defined in Fourier space. If we rewrite $D_{\text{chem}} \sim \frac{\ell^2_{\text{chem}}}{\tau_{\text{chem}}}$ and are interested in time scales much larger than the diffusion time τ_{chem}, we can approximate eq. (2.2) as above. A similar approximation for the chemical diffusion equation has been applied in [45, 51, 52], among others.

With this, one can derive an equation for the time evolution of the cell density $\partial_t C(\mathbf{r},t) = \partial_t \sum_i \delta\left(\mathbf{r} - \mathbf{r}_i(t)\right)$ in analogy with [53] as:

$$\partial_t C = D\nabla^2 C + \mu\nabla\cdot(C\nabla\phi) + \nabla\cdot\left[\sqrt{2DC}\,\mathbf{f}(\mathbf{r},t)\right] \tag{2.3}$$

where $\langle f_\alpha(\mathbf{r},t) f_\beta(\mathbf{r}',t')\rangle = \delta_{\alpha\beta}\delta(\mathbf{r}-\mathbf{r}')\delta(t-t')$ is Gaussian white noise [49]. This equation is an exact N-body stochastic equation for the process described in eq. (2.1) and does not contain any further approximations. But it is also possible to use the same scheme for a continuous coarse-grained cell density $C(\mathbf{r},t)$ even when it cannot be exactly described as a sum of δ-functions [47, 49].

In addition to chemotactic effects, we also want to consider the effect of changes in the number of cells by adding growth and number fluctuation terms to eq. (2.3):

$$\begin{aligned}\partial_t C &= D\nabla^2 C + \mu\nabla\cdot(C\nabla\phi) + \nabla\cdot\left[\sqrt{2DC}\,\mathbf{f}(\mathbf{r},t)\right] \\ &\quad + L(C) + \sqrt{2M(C)}\,g(\mathbf{r},t),\end{aligned} \tag{2.4}$$

where $\langle g(\mathbf{r},t)g(\mathbf{r}',t')\rangle = \delta(\mathbf{r}-\mathbf{r}')\delta(t-t')$. The most natural choice for $L(C)$ is logistic growth, $L(C) = \lambda C(C_0 - C)$ [54], where C_0 is the carrying capacity of the system and λ is an effective growth rate (with the unit λ: [length]^d/[time] [49]). However, possible growth terms can be more generic as long as there is $C_0 > 0$ with $L(C_0) = 0$ and $L'(C)|_{C_0} < 0$ [34], since higher order terms in growth would renormalise to zero in the following calculations [49]. The noise strength $M(C)$ will depend on the microscopic growth rule. In the appendix we will show one possible derivation for the stochastic growth and coagulation process resulting in $M(C) = \lambda C(C_0 + C)/2$. The same derivation can also be found in the supplement of [49].

For this study we will regard the case where the density of cells fluctuates around a constant background concentration C_0 by defining $C(\mathbf{r},t) = C_0 + \rho(\mathbf{r},t)$. The equation for the density fluctuations then becomes

$$\partial_t\rho = D\nabla^2\rho - \theta\rho - \nu_1\nabla\cdot\left[\rho\nabla\left(\frac{1}{\nabla^2}\right)\rho\right] - \frac{\nu_2}{2}\rho^2 + \eta, \tag{2.5}$$

where $\nu_1 = \mu\alpha_0$, $\nu_2 = 2\lambda$, $\theta = (\mu\alpha_0 + \lambda)C_0$, $D_0 = \lambda C_0^2$, and $D_2 = DC_0$ are the unrenormalized parameters directly related to microscopic constants. $\frac{1}{\nabla^2}$ is defined

as the inverse Laplacian in Fourier space and the noise correlator in Fourier space is given as $\langle \eta(\mathbf{k},\omega)\eta(\mathbf{k}',\omega')\rangle = 2\left[D_0 + D_2 k^2\right](2\pi)^{d+1}\delta(\mathbf{k}+\mathbf{k}')\delta(\omega+\omega')$ [49]. It should be noted that with this approximation we went from a multiplicative to an additive noise, which significantly simplifies the problem. We have made this approximation because $\nabla\cdot\left[\sqrt{2D(C_0+\rho)}\,\mathbf{f}(\mathbf{r},t)\right] \approx \nabla\cdot\left[\sqrt{2DC_0}(1+\frac{1}{2}\rho/C_0)\,\mathbf{f}(\mathbf{r},t)\right]$, i.e. the noise corrections are finite and of order of ρ/C_0. Thus, this corrections should stay finite and small even under rescaling.

2.3 Perturbative Expansion

If we ignore nonlinear terms, we can expect a chemotactic collapse at $\theta < 0$, i.e. $\mu < \lambda/\alpha_0$ for dividing cells. This is a shift from a predicted chemotactic collapse at $\mu = 0$ for the Keller-Segel model [30, 49]. To further study the different phases of the system we perturbatively expand the nonlinearities proportional to ν_1, ν_2 in eq. (2.5) and perform a dynamical Renormalization Group analysis, as described in section 1.4.

Fourier transforming Eq. (2.5) gives [49]

$$\begin{aligned} i\omega\rho(\mathbf{k},\omega) &= -Dk^2\rho(\hat{k}) - \theta\rho(\hat{k}) + \eta(\hat{k}) - \frac{1}{2}\int \frac{d^{d+1}\hat{k}_1}{(2\pi)^{d+1}}\rho(\hat{k}_1)\rho(\hat{k}-\hat{k}_1) \\ &\times\left[\nu_1\mathbf{k}\cdot(\mathbf{k}-\mathbf{k}_1)/(\mathbf{k}-\mathbf{k}_1)^2 + \nu_1\mathbf{k}\cdot\mathbf{k}_1/\mathbf{k}_1^2 + \nu_2\right], \end{aligned} \tag{2.6}$$

where we used the convention $\rho(\mathbf{r},t) = \int d\hat{k}/(2\pi)^{d+1}\rho(\hat{k})e^{i\omega t - i\mathbf{kx}}$ and defined $\hat{k} :=$

$(\mathbf{k}, \omega)$ [49]. For our Renormalization Group analysis we will use this equation to derive a perturbative expansion for the Green's function $G(\hat{k})$, the noise correlator $\mathcal{D}(\mathbf{k})$ and the vertex function $\Gamma(\mathbf{k}, \mathbf{q})$. In absence of nonlinearities, the bare value of the Green's function is $G_0(\hat{k}) = [i\omega + Dk^2 + \theta]^{-1}$, the bare noise correlator is $\mathcal{D}_0(\mathbf{k}) = D_0 + D_2 k^2$ and the bare vertex is $\Gamma_0(\mathbf{k}, \mathbf{q}) = \Gamma_0(\mathbf{k}, \mathbf{k}-\mathbf{q}) = -\frac{1}{2}(\nu_1 \mathbf{k}\cdot\mathbf{q}/(\mathbf{q})^2 + \nu_1 \mathbf{k}\cdot(\mathbf{k}-\mathbf{q})(\mathbf{k}-\mathbf{q})^2 + \nu_2)$ [49]. If $\theta \to 0$, we see a divergence of $G_0(\hat{k}) = [i\omega + Dk^2 + \theta]^{-1}$ for large times and long ranges ($\hat{k} \to 0$), indicating a phase transition which shows self-similar behaviour. We therefore expect the renormalization group analysis to hold in the limit $\theta \to 0$.

We can rewrite eq. (2.6) as

$$\begin{aligned} \rho(\hat{k}) =& G_0(\hat{k})\eta(\hat{k}) - \frac{1}{2} G_0(\hat{k}) \int \frac{d^{d+1}\hat{k}_1}{(2\pi)^{d+1}} \rho(\hat{k}_1)\rho(\hat{k} - \hat{k}_1) \\ & \times \left[\nu_1 \mathbf{k}(\mathbf{k} - \mathbf{k}_1)/(\mathbf{k} - \mathbf{k}_1)^2 + \nu_1 \mathbf{k}\mathbf{k}_1/(\mathbf{k}_1)^2 + \nu_2\right] \end{aligned} \tag{2.7}$$

and use it as a starting point to find the diagrammatic expansion of Green's function, noise correlation and vertex function in terms of $\nu_{1,2}$. The resulting expressions can be concisely visualised in Feynman diagrams (fig. 2.2) and are:

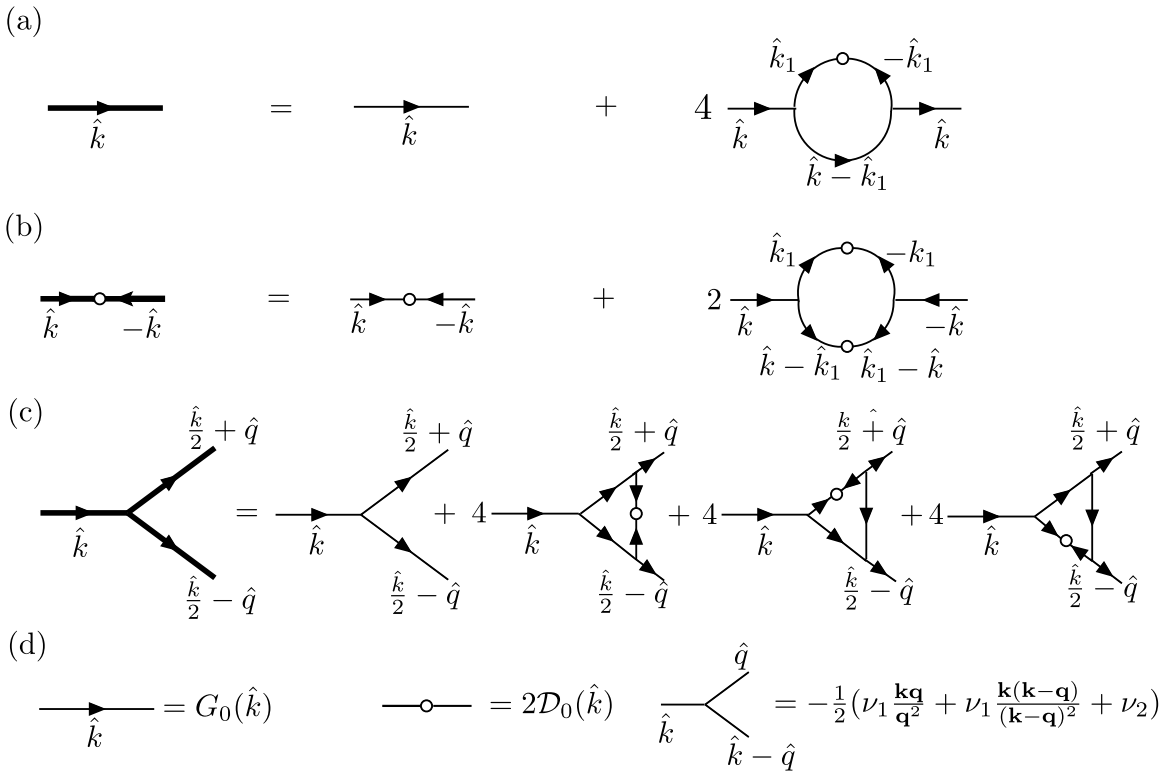

Figure 2.2: Feynman diagrams for (a) the Green's function $G(\hat{k})$, (b) the noise correlation strength $\mathcal{D}(k)$ and (c) the vertex function, expressed in terms of the bare Green's function $G_0(\hat{k}) = [i\omega + Dk^2 + \theta]^{-1}$ and bare noise correlator $\mathcal{D}_0(k) = D_0 + D_2 k^2$, where $\hat{k} := (\mathbf{k}, \omega)$. Taken with permission from [49].

$$G(\hat{k})^{-1} = G_0(\hat{k})^{-1} - \int \frac{d^{d+1}\hat{k}_1}{(2\pi)^{d+1}} \Big\{ \mathcal{D}(\mathbf{k}_1) \big[\nu_1 \mathbf{k} \cdot (\mathbf{k} - \mathbf{k}_1)/(\mathbf{k} - \mathbf{k}_1)^2 + \nu_1 \mathbf{k} \cdot \mathbf{k}_1/(\mathbf{k}_1)^2 + \nu_2 \big]$$
$$\times \big[\nu_1 (\mathbf{k} - \mathbf{k}_1) \cdot \mathbf{k}/(\mathbf{k})^2 - \nu_1 (\mathbf{k} - \mathbf{k}_1) \cdot \mathbf{k}_1/(\mathbf{k}_1)^2 + \nu_2 \big] |G_0(\hat{k}_1)|^2 G_0(\hat{k} - \hat{k}_1)$$
$$+ \mathcal{D}(\mathbf{k} - \mathbf{k}_1) \big[\nu_1 \mathbf{k} \cdot (\mathbf{k} - \mathbf{k}_1)/(\mathbf{k} - \mathbf{k}_1)^2 + \nu_1 \mathbf{k} \cdot \mathbf{k}_1/(\mathbf{k}_1)^2 + \nu_2 \big]$$
$$\times \big[\nu_1 \mathbf{k}_1 \cdot \mathbf{k} A(\mathbf{k}) - \nu_1 \mathbf{k}_1 \cdot (\mathbf{k} - \mathbf{k}_1)/(\mathbf{k} - \mathbf{k}_1)^2 + \nu_2 \big] |G_0(\hat{k} - \hat{k}_1)|^2 G_0(\hat{k}_1) \Big\} \tag{2.8a}$$

$$2\mathcal{D}(\mathbf{k}) = 2\mathcal{D}_0(\mathbf{k}) + \frac{1}{2} \int \frac{d^{d+1}\hat{k}_1}{(2\pi)^{d+1}} \Big\{ 2\mathcal{D}_0(\mathbf{k}_1) 2\mathcal{D}_0(\mathbf{k} - \mathbf{k}_1)$$
$$\big[\nu_1 \mathbf{k} \cdot (\mathbf{k} - \mathbf{k}_1)/(\mathbf{k} - \mathbf{k}_1)^2 + \nu_1 \mathbf{k} \cdot \mathbf{k}_1/(\mathbf{k}_1)^2 + \nu_2 \big] \tag{2.8b}$$
$$\times \big[\nu_1 \mathbf{k} \cdot (\mathbf{k} - \mathbf{k}_1)/(\mathbf{k} - \mathbf{k}_1)^2 + \nu_1 \mathbf{k} \cdot \mathbf{k}_1/(\mathbf{k}_1)^2 + \nu_2 \big] |G_0(\hat{k}_1)|^2 |G_0(\hat{k} - \hat{k}_1)|^2 \Big\}$$

$$\Gamma(\mathbf{k}, \mathbf{k}/2 + \mathbf{q}) = \Gamma_0(\mathbf{k}, \mathbf{k}/2 + \mathbf{q}) - \int \frac{d^{d+1}\hat{q}_1}{(2\pi)^{d+1}} \Big\{$$
$$\mathcal{D}(\mathbf{q} - \mathbf{q}_1) G_0(\hat{k}/2 + \hat{q}_1) G_0(\hat{k}/2 - \hat{q}_1) |G_0(\hat{q} - \hat{q}_1)|^2$$
$$\times \big[\nu_1 \frac{\mathbf{k} \cdot (\mathbf{k}/2 + \mathbf{q}_1)}{(\mathbf{k}/2 + \mathbf{q}_1)^2} + \nu_1 \frac{\mathbf{k} \cdot (\mathbf{k}/2 - \mathbf{q}_1)}{(\mathbf{k}/2 - \mathbf{q}_1)^2} + \nu_2 \big]$$
$$\times \big[\nu_1 \frac{(\mathbf{k}/2 + \mathbf{q}_1) \cdot (\mathbf{k}/2 + \mathbf{q})}{(\mathbf{k}/2 + \mathbf{q})^2} + \nu_1 \frac{(\mathbf{k}/2 + \mathbf{q}_1) \cdot (\mathbf{q}_1 - \mathbf{q})}{(\mathbf{q}_1 - \mathbf{q})^2} + \nu_2 \big] \times$$
$$\big[\nu_1 \frac{(\mathbf{k}/2 - \mathbf{q}_1) \cdot (\mathbf{k}/2 - \mathbf{q})}{(\mathbf{k}/2 - \mathbf{q})^2} + \nu_1 | \frac{(\mathbf{k}/2 - \mathbf{q}_1) \cdot (\mathbf{q} - \mathbf{q}_1)}{(\mathbf{q} - \mathbf{q}_1)^2} + \nu_2 \big] \tag{2.8c}$$
$$+$$
$$2 \times \mathcal{D}(\mathbf{k}/2 + \mathbf{q}_1) G_0(\hat{k}/2 + \hat{q}_1) |G_0(\hat{k}/2 - \hat{q}_1)|^2 G_0(\hat{q} - \hat{q}_1)$$
$$\times \big[\nu_1 \frac{\mathbf{k} \cdot (\mathbf{k}_2 + \mathbf{q}_1)}{(\mathbf{k}/2 + \mathbf{q}_1)^2} + \nu_1 \frac{\mathbf{k} \cdot (\mathbf{k}/2 - \mathbf{q}_1)}{(\mathbf{k}/2 - \mathbf{q}_1)^2} + \nu_2 \big]$$
$$\times \big[\nu_1 \frac{(\mathbf{q} - \mathbf{q}_1) \cdot (\mathbf{k}/2 + \mathbf{q})}{(\mathbf{k}/2 + \mathbf{q})^2} + \nu_1 \frac{(\mathbf{q} - \mathbf{q}_1) \cdot (-k/2 - \mathbf{q}_1)}{(\mathbf{k}/2 + \mathbf{q}_1)^2} + \nu_2 \big]$$
$$\times \big[\nu_1 \frac{(\mathbf{k}/2 - \mathbf{q}_1) \cdot (\mathbf{k}/2 - \mathbf{q})}{(\mathbf{k}/2 - \mathbf{q})^2} + \nu_1 \frac{(\mathbf{k}/2 - \mathbf{q}_1) \cdot (\mathbf{q} - \mathbf{q}_1)}{(\mathbf{q} - \mathbf{q}_1)^2} + \nu_2 \big] \Big\}$$

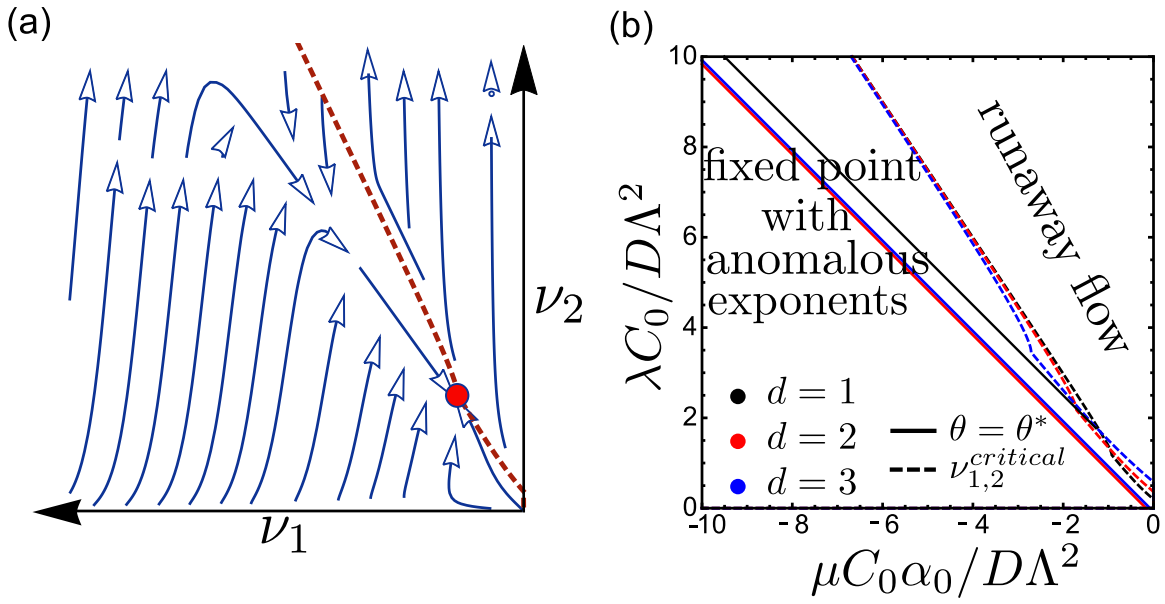

Figure 2.3: (a) shows the Renormalization Group flow in (ν_1, ν_2) space. There are two parameter regions with a separatrix in-between (red dotted line). Below the separatrix, the flow runs into a perturbatively accessible fixed point (red) with finite chemotaxis strength and growth. Above the separatrix, however, one can see that the flow goes towards a region where growth and death processes dominate over chemotaxis. Hence, the system in this case becomes similar to the Fisher equation and is expected to show instabilities, chaos and nonlinear fronts [55–57]. (b) shows the phase separation for different spatial dimensions ($d = 1$, 2, 3). Taken with permission from [49].

2.4 Renormalization and Flow Diagrams

As described in section 1.4, one of the characteristics at a phase transition point is scale-invariance associated with the divergence of length- and timescales. Expecting a critical phase transition, we will therefore rescale length- and timescales to find criteria under which the system is scale-invariant. We choose a continuous scaling factor $b = e^{\ell}$ to rescale space as $\mathbf{r} \to e^{\ell}\mathbf{r}$) and time as $t \to e^{\ell z}t$ [49]. The corrections due to rescaling can then be obtained by integrating out large wavelength between $\Lambda e^{-\ell}$ to Λ, where $\Lambda = 2\pi/a$ is an upper cutoff in Fourier space determined by the cell

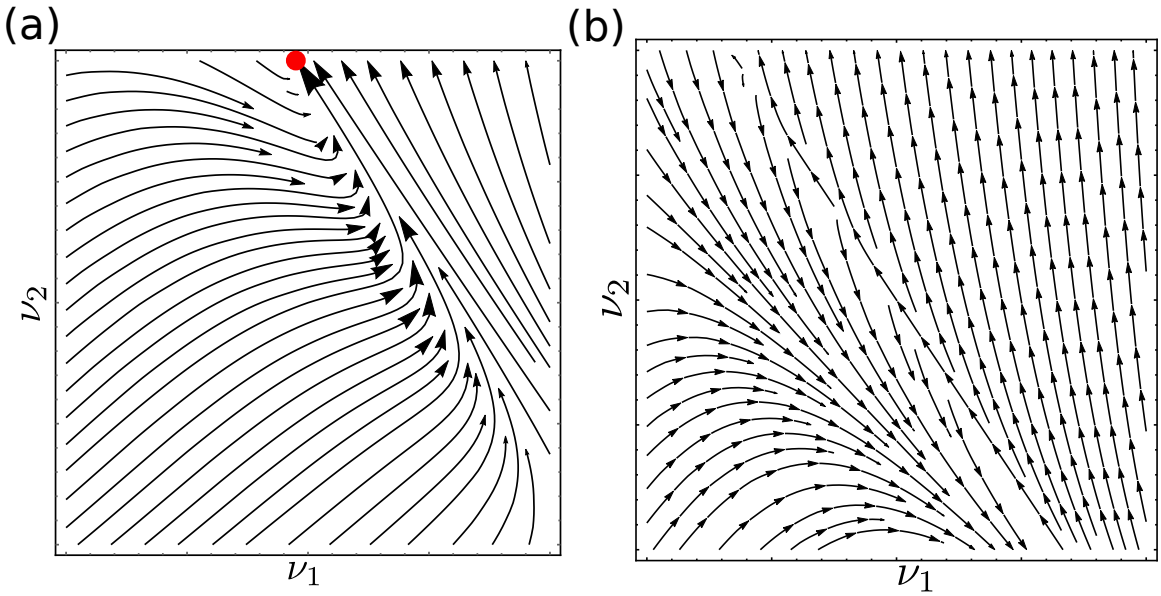

Figure 2.4: Enlarged flow around the separatrix in 2.3 (a) Below the fixed point, the flow directions are aligned with each other on both sides of the saparatrix. However, while the flow below the separatrix is going towards the fixed point, the flow above is a runaway flow, see 2.3. Directly on the separatrix, the flow goes directly into the fixed point. (b) On the other hand, above the fixed point the flow completely reverses directions along the separatrix. Below the separatrix, the flow goes into the fixed point, while above it becomes a runaway flow towards large ν_2.

size a [49].

Forster et al. [36] discuss an expansion in terms of coupling constants (here: ν_1 and ν_2): while it in general would be problematic to assume that ν_1, ν_2 are small parameters, the expansion is here done to assess the small contributions of large wavelenghts/short lengthscales on the existing coupling constants of the system. In other words, while ν_1 and ν_2 are nonvanishing parameters, the corrections to the coupling constants due to large wavelengths $\Lambda e^{-\ell}$ to Λ are $\mathcal{O}(\ell)$ and small if ℓ if $\ell \ll 1$ (or even treated as infinitesimal, as below) [36].

Rescaling the above equations also emphasises the importance of universality: in general, cells will also experience a variety of short-range interactions between them, which could for example be due to contact between flagella or due to excluded volume effects. We can take these interactions into account by also adding a short-range potential $\Psi(\mathbf{r}, t)$ in addition to the long-range chemical field $\phi(\mathbf{r}, t) = \int d^d\mathbf{r}' C(\mathbf{r}_0, t) G(\mathbf{r} - \mathbf{r}'))$ with a short-range kernel $\int G(\mathbf{r}) d\mathbf{r} = \text{const.}$. In equation 2.4 this is reflected by adding a term $\xi\nabla(C\nabla\Psi)$. However, while the chemotactic and the growth term scale as $b^{2\chi}$, the short-range term will only scale as $b^{2\chi-2}$, indicating that it becomes irrelevant under rescaling, indicating that 2.4 is a universal equation that is robust under changes of short-term interaction [49].

Following rescaling and integrating out large wavelengths we obtain the following flow equations under in infinitesimal rescaling with a scaling factor $b = e^{\ell}$:

$$\frac{d\theta}{d\ell} = z\theta - \frac{\nu_2 K_d \Lambda^{d-4}}{2D^2}\Big\{D_0\Big[(3+2/d)\nu_1 + 2\nu_2\Big] + 3\nu_1 D_2\Lambda^2\Big\}, \tag{2.9a}$$

$$\frac{d\nu_1}{d\ell} = \nu_1\left\{\chi + z + \frac{\nu_2 \pi K_d \Lambda^{d-6}}{4D^3}\Big[3\nu_1 + 2\nu_2\Big](D_0 + D_2\Lambda^2)\right\}, \tag{2.9b}$$

$$\frac{d\nu_2}{d\ell} = \nu_2\left\{\chi + z + \frac{\pi K_d \Lambda^{d-6}}{D^3}\Big[3\nu_1 + 2\nu_2\Big]\Big[\nu_1 + \nu_2\Big](D_0 + D_2\Lambda^2)\right\}, \tag{2.9c}$$

$$\begin{aligned}\frac{dD}{d\ell} = D\Bigg(z - 2 - \frac{K_d\Lambda^{d-6}}{8D^3}\Bigg\{&\frac{(2d-4)}{d}D_2\Lambda^2\Big[3\nu_1 - 2\nu_2\Big]\Big[2\nu_1 + \nu_2\Big] \\ &+ 4D_0\nu_2\Big[\frac{(17-5d)}{d}\nu_1 + 2\nu_2\Big]\Bigg\}\Bigg),\end{aligned} \tag{2.9d}$$

$$\frac{dD_0}{d\ell} = D_0(z - d - 2\chi) + \frac{\nu_2^2 K_d \Lambda^{d-6}}{2D^3}(D_0 + D_2\Lambda^2)^2, \tag{2.9e}$$

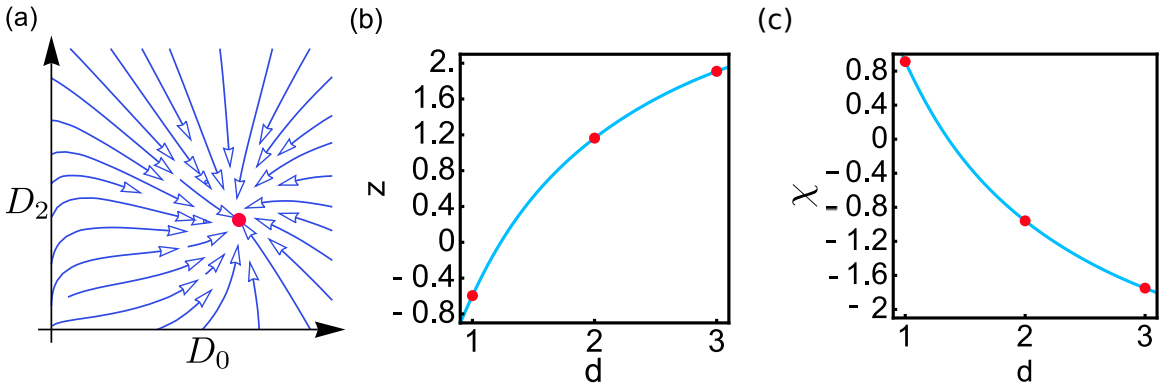

Figure 2.5: (a) shows that for spatial dimensions $d \leq 4$, the perturbatively accessible fixed point is stable in D_0-D_2 space. In addition to that, one can see that $D_0 \neq 0$ at the fixed point, implying that particle fluctuation noise is always generated through renormalization, even if it was not initially present. (b) shows the values for the critical exponent z associated with time and diffusion, in dependence of the dimension d. (c) shows the values for the critical exponent χ associated with density and number fluctuations, in dependence of the dimension d [49]. The values for $d = (1, 2, 3)$ – denoted with red dots in (b) and (c) – are also listed in Table 2.1 and [49]. Taken with permission from [49].

$$\frac{dD_2}{d\ell} = D_2(z - d - 2 - 2\chi) - \frac{\nu_2 K_d \Lambda^{d-8}}{8dD^3}\Big\{7\nu_1\Big[D_0^2 + \frac{(8d-2)}{7}D_0 D_2 \Lambda^2 + D_2^2\Lambda^4\Big] + \nu_2(D_0 + D_2\Lambda^2)\Big[(3d-14)D_0 + (d-2)D_2\Lambda^2\Big]\Big\}, \tag{2.9f}$$

where $K_d = S_d/(2\pi)^d$ and $S_d = 2\pi^{d/2}/\Gamma(d/2)$ is the area of unit sphere in d dimensions [49].

2.5 Critical Behaviour

At a critical point we require that the system is scale invariant and hence that infinitesimal corrections to the coupling constants (2.5) vanish [49]. This condition is fulfilled for the fixed point values $\nu_1^* = -3\sqrt{D^3(\chi+z)/\left[\pi K_d(D_0+D_2\Lambda^2)\right]}$ and $\nu_2^* = -\frac{4}{3}\nu_1^*$. Figure 2.3(a) visualises the flow given by eqs. (2.9b) and (2.9c) around these fixed points and fig. 2.4 shows an enlargement below and above the separatrix. If the initial value of ν_1 and ν_2 is above a dimension-dependent critical value indicated by the separatrix in 2.3(a), we have a runaway flow indicating a perturbatively non-accessible fixed point. A runaway flow commonly hints at a first-order phase transition [58] but a more careful analysis would be needed to establish this [59]. Most remarkably, however, the runaway flow here moves the system to a region where the chemotactic term is irrelelevant and growth and death processes dominate [49]. This suggests that the equation belongs to the universality class of Fisher equations above the threshold. The Fisher equation is known to show instabilities, chaos and nonlinear fronts [55–57]. If the initial value of ν_1 and ν_2 is below a dimension-dependent threshold in ν_1 and ν_2, however, rescaling will lead the system towards the fixed point ν_1^* and ν_2^* [49]. Below this threshold we also find a fixed point value $\theta^* = -\frac{2D}{\pi}\Lambda^2\left(\frac{\chi+z}{z}\right)\left[1+\frac{6}{d}\frac{D_0}{D_0+D_2\Lambda^2}\right]$, as well as fixed point values for D_0 and D_2. This gives the phase diagram shown in fig. 2.3 (b) for different dimensions d [49]. For D_0 and D_2 we always find a perturbatively accessible nontrivial stable fixed point in the dimensions $d \leq 4$. This stable fixed point is shown in fig. 2.5 (a). Remarkably, the fixed point has both diffusive and particle fluctuation noise, indicating that particle fluctuation noise will be generated through

the renormalization process – even if the particle fluctuation noise $M(C)$ was initially zero. The stable fixed point also enables us to perturbatively calculate the critical exponents z and χ for the dimensions $d = (1, 2, 3)$, as shown in Table 2.1 [49]. The fractionality of these exponents implies anomalous diffusion and density fluctuations. The mean squared displacement behaves as $\Delta L^2(t) = \langle[\mathbf{r}(t) - \mathbf{r}(0)]^2\rangle \sim t^{2/z} = t^{\alpha}$, which implies superdiffusivity in two and three dimensions. This superdiffusive behaviour is likely a combination of Fisher-type and gradient-following components in the underlying equations: noisy Fisher-type equations are known for to produce wave-like excitations over large time scales [56]. But – maybe even more importantly – Lubashevsky et al. [60] have found that extremely large fluctuations in the particle velocity pattern can effectively constitute a Levy-like flight and lead to superdiffusive behaviour. In this case, the particle velocity is linearly dependent on the chemical concentration gradient $\nabla\phi$, which can become large due to fluctuations and random aggregations. We can speculate that the combination of Fisher-like density waves and the resulting velocity fluctuations can motivate the strongly superdiffusive behaviour seen here.

The density correlations $\langle\rho(\mathbf{r}, t)\rho(\mathbf{r}', t)\rangle \sim |\mathbf{r} - \mathbf{r}'|^{2\chi}$ imply number fluctuations since $\Delta N^2 = \int d^d\mathbf{r} d^d\mathbf{r}' \langle\rho(\mathbf{r}, t)\rho(\mathbf{r}', t)\rangle$. In total, the number fluctuations will scale as $\Delta N \sim L^{d+\chi} = L^{\beta}$ [49]. Again, these number fluctuations and the subsequent fluctuations in production of chemicals have a bearing on the particle velocity and could enhance superdiffusion. In absence of growth of chemotaxis, we would have $\chi = -d$ and $z = 2$, which, as expected, implies normal diffusion and no number

Table 2.1: This table summarizes the critical exponents found at the critical fixed point.

	$d=1$	$d=2$	$d=3$
z	-0.60	1.16	1.90
χ	0.91	-0.95	-1.75
$\alpha = 2/z$	-3.33	1.72	1.05
$\beta = d + \chi$	1.91	1.05	1.25

fluctuations in the system. For one dimension the exponent for z is negative, which would imply finite mean square displacement and localizations [49].

2.6 Discussion

In this chapter we have applied the technique of Dynamical Renormalization Groups to study the influence of chemotaxis and growth on cells. We have derived a generic model and shown that it is robust under coarse-graining and short-range interactions. Interestingly, we have found that chemotaxis and growth are of the same order of relevance in a renormalization group sense and shown that their interplay leads to a rich phase diagram [49]. We find a phase with a runaway flow, as well as a stable phase where we can calculate the critical exponents.

Experimentally, our results could be tested in a controlled cellular system where parameters such as the cell carrying capacity C_0, the cell growth rate λ and the diffusion constant D can be varied [49]. From the phase diagram in fig. 2.3 (b) we expect that the phase transition could be observed if the average time a cell takes to move a distance of the order of its own size is comparable to the cell division

time [49]. This is for example plausible for tumor cells where the cell division rates are of the order of $10^{-5}/s$ [49, 61]. With an estimated viscosity of 1 Pa s and hence a diffusion constant of the order of $\sim 10^{-4}$ μm^2/s and a tumor cell size of the order of ~ 10 μm, this condition could be fulfilled. Even though a more thorough analysis of the runaway fixed point is needed, from the picture in fig. 2.3 (a) we can speculate that the separatrix correnspponds to a transition beween a phase of controlled chemotaxis and growth to a phase where growth and death processes dominate. Interestingly, the initial values of chemotaxis and growth tightly control the macroscopic behaviour of the (tumor) cells [49].

As a possible application, our results could help understand the interplay between chemotaxis and growth in cancer cells, in particular the sharp transition between controlled growth and cancer metastasis and how cancer cells in a metacommunity can show coordination despite large spatial separations [43, 49].

Chapter 3

Trail Deposition and Microcolony Formation in *P. Aeruginosa*

3.1 Introduction

In the last chapter we investigated the effects of chemotaxis in the limit of a fast diffusion of a chemoattractant, but now we will focus on the opposite limit: microorganism-secreted chemicals that are diffusing so slowly that their diffusion coefficient can effectively be neglected. In biology, such a trail deposition mechanism is of particular importance on two-dimensional surfaces. Self-deposited trails of pheromones can effectively act as traffic lanes that guide ants to a food source and provide a means of collective cognition [62, 63]. Pheromone trails can be effectively sensed using odor receptors in the ants' antennae [62, 63]. However, recent experiments [1] suggest that

also much simpler microorganisms show motion in reaction to self-secreted sticky, slowly-diffusing trails [64]. But to sense these trails, it seems that nature prefers a mechanistic approach over a much more complex chemical sensing cascade: For *Pseudomonas Aeruginosa* bacteria it has been shown that Type IV pili (TFP) play a pivotal role in social motility by preferentially attaching to surface regions coated with exopolysaccharides (EPS) and pulling the cells towards these regions. In the context of tumor growth and wound healing, such a mechanism is commonly referred to as *haptotaxis*, i.e. motion generated in response to a gradient in attachment strength [65–67]. However its effects have so far remained mostly unstudied for pili-propelled bacteria.

Pseudomonas aeruginosa bacteria secrete a trail of the exopolysaccharide Psl [1, 68, 69] and they are known to pull themselves forward and sense Psl using Type IV pili i.e. hair-like appendages with the ability to attach to a surface and generate propulsion forces through retraction [1, 2, 70–73]. The secreted Psl trails promote surface attachment and act as attractants for other pseudomonas bacteria [2, 74]. They also have been shown to be crucial at the early stages of pseudomonas biofilm formation [1]. Bacteria tend to follow Psl trails of other bacteria, which, due to their own Psl deposition, constitutes positive self-feedback attracting more bacteria. In this way, some surface sites will be much more frequently visited than others, which is characterized by a power-law distribution in Psl concentration and surface visits [1, 75, 76]. In the later development stages the frequently visited sites become the places of microcolony development [1].

We will highlight the key observations on P. Aeruginosa from Zhao et al. [1], as well as new experimenal results obtained by Kun Zhao, Calvin K. Lee and Gerard C. L. Wong [77, 78]. Based on these observations, we will construct a model for P. Aeruginosa and derive stochastic equations of motion for single bacteria reacting to a trail of polysaccharides. As a crucial consequence we find that pili not only give rise to gradient-dependent displacement but also to a gradient-dependent alignment term which stabilizes the bacterial trajectory [77, 78]. We study the effects of the alignment term and show that it can lead to a rich behavour including oscillations, trail escape events and enhanced rotational diffusion. After carrying out multi-bacteria simulations with the same model, we then find that it also quantitatively predicts hallmarks of the early stages of biofilm formation observed in experiments [1], like surface visit distributions, power law behaviour and a self-feedback mechanism for bacterial aggregation.

3.2 Key experimental observations

The Pseudomonas Aeruginosa wild-type strain PAO1 deposits an *extracellular matrix* which mostly consists of exopolysaccharides, proteins and DNA [1] of primarily two types: Psl and Pel [1]. In the initial stages of the biofilm formation, it is known that mostly Psl is used to promote adhesion and surface exploration [1]. In their experimental work, Zhao et al. have examined the effects of Psl deposition at the early stages of biofilm formation using single-bacteria tracking algorithms [1].

The PAO1 $\Delta pslD$ strain (which does not produce Psl) showed a $35 \pm 10\%$ decrease in surface attachment compared to the wild-type, confirming that Psl can promote adhesion [1]. But importantly, Psl secretion also fundamentally alters the way in which bacteria explore the surface: Tracking the bacterial locations on a $67\mu\text{m} \times 67\mu\text{m}$ field of view over 11h (with a time resolution of 3s) revealed that the surface coverage for the Psl-secreting wild-type is much lower than for the non-secreting mutant $\Delta pslD$ [1]. After 11h, approximately 55% of the field was visited by the wild type, whereas the $\Delta pslD$ mutant covered about 79% of the field [1].

A confirmation that wild-type bacteria deposit Psl along their trajectory was obtained by visualising the deposited Psl field using a TRITC-conjugated, Psl-specific lectin [1]. Figures 3.1 (e) and (f) show a clear correlation between the trajectories and lectin-stained trails [1]. Extracellular DNA, on the other hand, was not found in the trails [1].

Using cell-tracking algorithms, Zhao et al. determined the frequency of bacterial visits per surface pixel for the entire colony over the period of 15.7h [1]. For the wild-type a considerable fraction of the surface never got visited, or got visited only once. The histogram of visit frequencies per pixel, fig. 3.2 (c) underlines this trend: the distribution of visit frequencies behaves like a power-law with most of the pixels having only few visits and only few pixels with many visits [1]. The experimentalists examined the dependence of the power-law exponent on Psl secretion using the $\Delta P_{psl}/P_{BAD} - psl$ mutant, which produces Psl in dependence of arabinose in the growth medium [1]. With increasing arabinose concentration (and thus in-

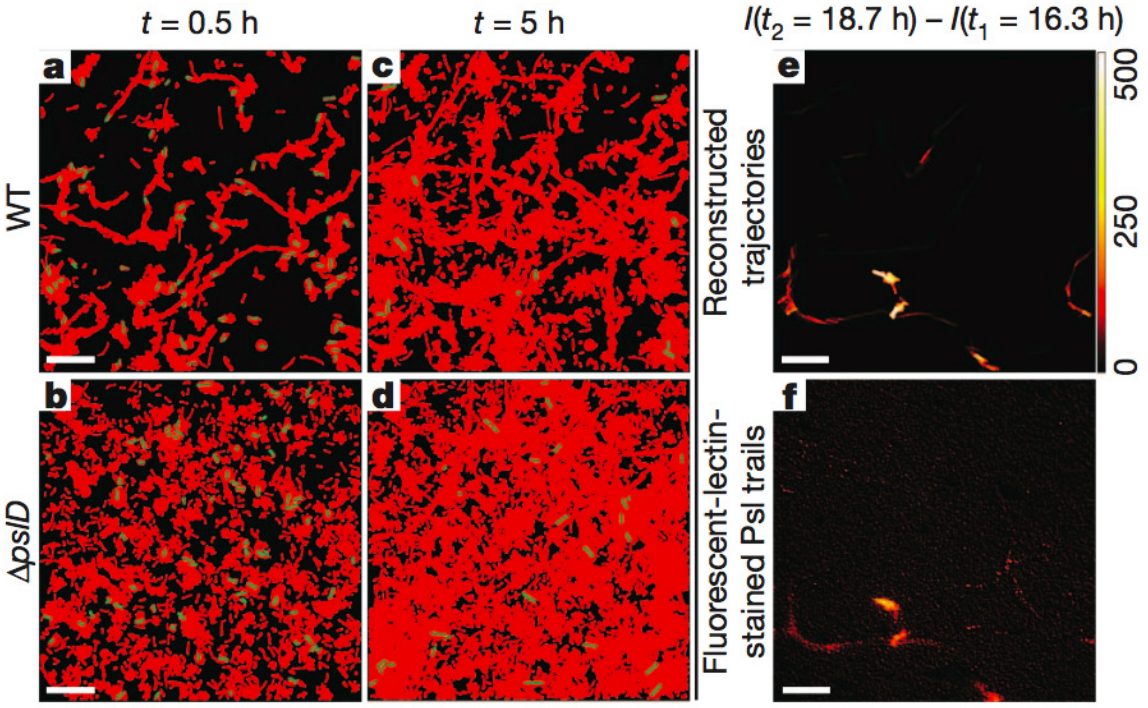

Figure 3.1: Figure taken with permission from [1]. (a-d) Typical surface area visited by bacteria after 0.5h (a,b) and 5h (c,d). Red indicates that the surface pixel has been visited within the time frame. Bacteria at the specific time points are shown in green [1]. $\Delta pslD$ mutants, which are unable to produce Psl, show a significantly higher surface coverage than wild-type bacteria, hinting that Psl facilitates accumulation of bacteria in a smaller area [1]. (e) shows the reconstructed wild type trajectories within the time frame between 16.3h and 18.7h after inoculation, whereas (f) shows a fluorescent visualization of the Psl left within the same time frame [1]. One can see that wild type bacteria have deposited Psl along their trajectory. Scale bars correspond to 10μm

creasing Psl production), the power-law distribution went from a more uniform to a more hierarchical one, corresponding to an increase in the power-law exponent from -3.3 ± 0.1 to -1.9 ± 0.1 [1]. Fig. 3.2 (g) and (h) show this increase. This implies an increasing accumulation of bacterial visits in a smaller surface area, suggesting that higher Psl concentrations lead to increased visits by the bacteria, thus increasing the Psl concentration even more and providing a self-feedback mechanism for bacterial accumulation [1].

Zhao et al. have identified Type IV pili as essential for this mechanism, as they help the bacteria explore the surface, associate with Psl-rich surface regions and preferentially pull the bacteria towards them [1]. The authors point out that trail-following is just one possible manifestation and that the bacteria do not always align themselves with existing tracks [1].

Kun Zhao, Calvin K, Lee and Gerard C. L. Wong also experimentally measured movement characteristics of single bacteria under the influence of Psl [77,78]. Figures 3.3 (c) and (d) show analyzed results from data obtained at 0% arabinose and 1% arabinose at the early stages before the formation of microcolonies. The figures. 3.17 (c) and (d) show the distributions of the change in bacterial body orientation $\Delta\alpha$ (see schematics fig. 3.3 (b)) within a 3s time frame. It should be noted from figs. 3.17 (c) and (d) that the distribution for $\Delta\alpha$ is very narrow and seems to be mostly independent of the Psl deposition strength. This suggests a small and largely Psl-independent rotational diffusion.

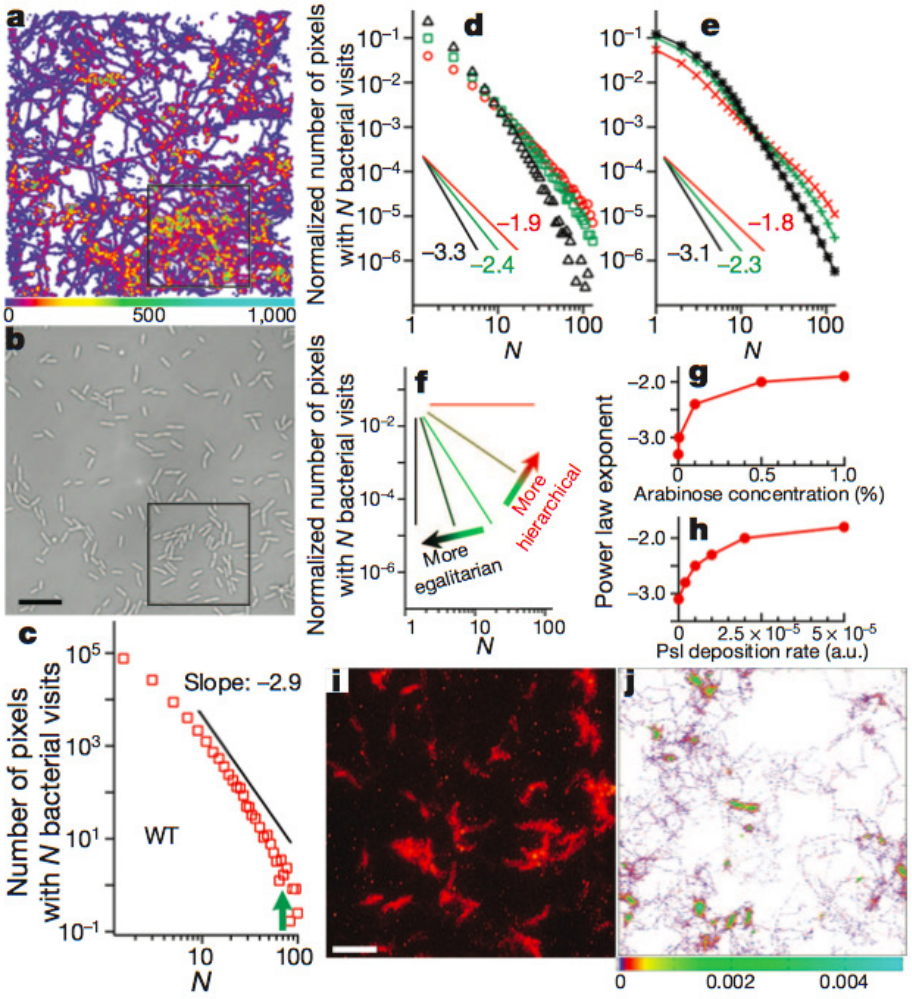

Figure 3.2: Figure taken with permission from [1]. (a) Visit frequency of wild type bacteria after 15.7h, when microcolonies are starting to form. (b) Bright-field image of the bacteria. One can see an accumulation along frequently-visited (and hence Psl-rich) sites [1]. (c) The histogram of the number of visits per pixel approximately decays like a power law with an exponent of -2.9 [1]. The green arrow indicates the onset of deviations from a power law for large visit frequencies [1]. (d) shows the visit frequency distributions for the $\Delta P_{psl}/P_{BAD}-psl$ mutant, which produces Psl at a rate which depends on the arabinose concentration in the environment. The distributions are shown for 0% (triangles), 0.1% (squares) and 1% arabinose (circles). (e) shows comparable results of qualitative simulations in [1], for deposition rates 0, 10^{-5} and 5×10^{-5}, see [1]. (f) Schematic graph - slow power law decay corresponds to hierarchical Psl distributions [1]. (g) and (h) show the power-law exponents in dependence of arabinose concentration and Psl deposition for the $\Delta P_{psl}/P_{BAD} - psl$ mutant. (i) shows a fluorescent visualization of Psl, showing the unequal (hierarchical) Psl distribution for $\Delta P_{psl}/P_{BAD} - psl$ and 1% arabinose [1]. (j) shows the corresponding Psl distribution from the simulations as shown in [1] Scale bars correspond to 10μm.

On the other hand, the distribution of the angle $\Delta\theta$ (see schematics fig. 3.3(b)), i.e. the angle between the bacterial trajectory and the body orientation, is wide. Importantly, with increasing Psl deposition the $\Delta\theta$ distribution narrows down (compare figs. 3.3 (c) and (d)), showing that Psl stabilizes the bacterial trajectory and increases the correlation between orientation of the bacterial body and the moving direction [78].

The goal of our theoretical approach is to explore in a rigorous way how the motion of a single microorganism in response to an EPS trail leads to the formation of a microcolony in the collective case. To deepen the understanding of the central principles and mechanisms of motion, and to explain experimental results in a clear way, we will first derived the underlying equations of motion for a generic pili-propelled microorganism influenced by an EPS trail. This derivation can also be found in the supplement of our recent publication [78].

Following the derivation, we will study the effects exopolysaccharide deposition can have on a single bacterium. Most importantly, we will see that a self-deposited trail can lead to anomalous diffusion and even trapping. Cells interacting with other trails, on the other hand, can show oscillations, trail following, but also orthogonal trail escapes.

After that, we will show that, in the collective case, our model can directly explain many collective characteristics at the early stages of biofilm formation, like for example power-law distributions of visit frequencies and a smaller visited surface fraction

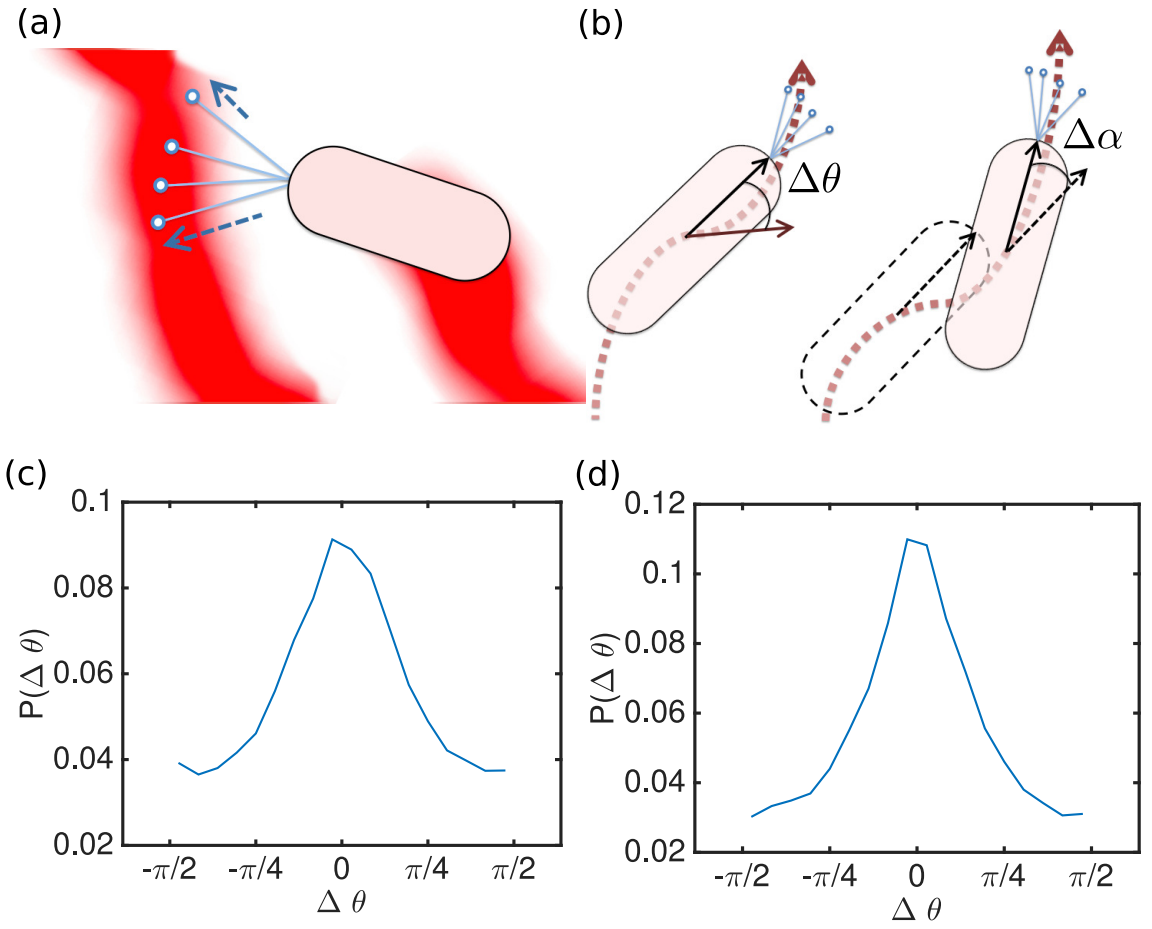

Figure 3.3: (a) Sketch of the bacterial model used in this thesis. Microorganisms secrete an exopolysaccharide (EPS, like for example Psl) trail. They move forward by attaching their pili (light blue) to the surface and retracting them. In general, the attachment/detachment rates and retraction forces will be dependent on the EPS concentration ψ. (b) illustrates the meaning of the angles $\Delta\theta$ (left) and $\Delta\alpha$ (right). $\Delta\theta$ is the angle between the microorganism orientation and trajectory (dotted line), smoothened over 21 time steps of 3s each using a Savitsky-Golay filter of third order [78]. $\Delta\alpha$ is the difference in orientation between two timesteps of 3s [78]. (c) and (d) depict the experimentally measured $\Delta\theta$ distributions for the mutant $\Delta P_{psl}/P_{BAD} - psl$, whose Psl secretion is induced by arabinose in the environment. In (c) we see the $\Delta\theta$ distribution for 0% arabinose, corresponding to a very low Psl secretion, whereas in (d) the Psl secretion is high with 1% arabinose. For distributions of $\Delta\alpha$ see fig. 3.17. It is worth noting that the $\Delta\theta$ distributions are much wider than the ones for $\Delta\alpha$ and that they narrow down with increasing Psl secretion. Figure taken with permission from [78].

with increasing exopolysaccharide secretion.

3.3 Model Derivation

We consider a microorganism of length ℓ, as shown in fig. 3.4. In agreement with the currently known geometry of P. Aeruginosa [1] we will assume that the N type-IV pili located at one tip (or both tips) of the microorganism will attach to/detach from a surface and pull the microorganism forward. In general, these attachment/detachment processes, as well as the pulling force, will be dependent on a possible exopolysaccharide (EPS) coating of the surface, since sticky, slowly-diffusing exopolysaccharides will alter the surface properties [78]. In this way, the type-IV pili enable the microorganisms to sense and react to exopolysaccharides without having to rely on a complex internal chemotactic sensing mechanism [1, 78].

The type-IV pili in our model are assumed to be approximately symmetrically arranged around the microorganism tip $\boldsymbol{r}_0$ (see fig. 3.4) and the direction unit vectors of the pili are denoted as $\hat{\boldsymbol{e}}_i,\ i = 1, \ldots, N$ [78]. Each of these pili (located at $\boldsymbol{r}_0 + \ell_p \hat{\boldsymbol{e}}_i$) will randomly attach to/detach from the surface, with EPS-dependent attachment and detachment rates $\lambda(\psi_i)$ and $\mu(\psi_i)$. Once attached, it will exert a pulling force $f_0(\psi_i)\hat{\boldsymbol{e}}_i$ on the tip of the microorganism. Here, ψ_i is a short-hand notation for the EPS concentration at the tip of pilus i, i.e. $\psi_i = \psi(\boldsymbol{r}_0 + \ell_p \hat{\boldsymbol{e}}_i)$ [78]. Let us also define an indicator function $\Theta_i = 1$ if the pilus is attached and $\Theta_i = 0$ if it is detached. Θ_i will then have a mean value of

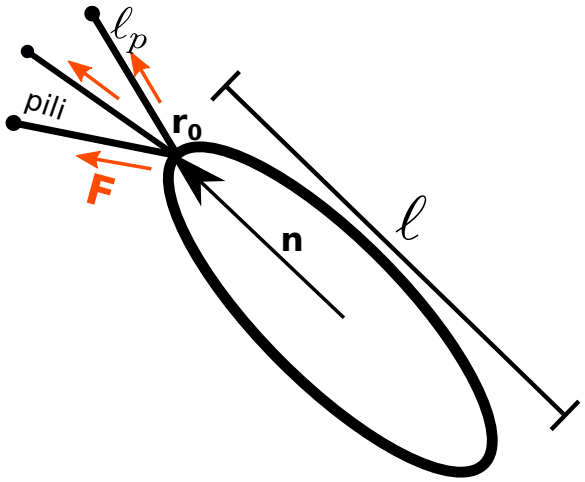

Figure 3.4: Microscopic model: the microorganism has type-IV pili of length ℓ_p, which can attach to a surface and pull the microorganism forward with a generically EPS-dependent force. Originating at a bacterial pole $\boldsymbol{r}_0$, the pili point in different directions $\hat{\boldsymbol{e}}_i,\ i = 1, \ldots, N$, such that the pili tips are located at the positions $\boldsymbol{r}_0 + \ell_p \hat{\boldsymbol{e}}_i$. A pilus pulling force $f_0(\psi_i)\hat{\boldsymbol{e}}_i$ on the microorganism tip $\boldsymbol{r}_0$ is only generated if the pilus is attached to the surface and in general the attachment and detachment rates $\lambda(\psi_i)$ and $\mu(\psi_i)$ will be dependent on the EPS concentration $\psi_i = \psi(\boldsymbol{r}_0 + \ell_p \hat{\boldsymbol{e}}_i)$ at the end of pilus i. Taken with permission from [78]

$$\bar{\Theta} = \langle \Theta_i \rangle = \frac{\lambda(\psi)}{\lambda(\psi) + \mu(\psi)} \tag{3.1}$$

and a standard deviation

$$\sigma = \sqrt{\langle (\Theta_i - \bar{\Theta})^2 \rangle} = \sqrt{\frac{\lambda(\psi)\mu(\psi)}{(\lambda(\psi) + \mu(\psi))^2}} \tag{3.2}$$

[78]. The total force from all the pili, which is exerted on the bacterial tip, will then be

$$\boldsymbol{F} = \sum_i \hat{\boldsymbol{e}}_i f_0(\psi_i)\Theta_i \tag{3.3}$$

We can rewrite $\Theta_i = \bar{\Theta} + \delta\Theta_i$, and expand $\psi_i = \psi(\boldsymbol{r}_0 + \ell_p \hat{\boldsymbol{e}}_i) \approx \psi(\boldsymbol{r}_0) + \ell_p(\boldsymbol{\nabla}\psi|_{\boldsymbol{r}_0} \cdot \hat{\boldsymbol{e}}_i)$, such that

$$\begin{aligned} \boldsymbol{F} = &\sum_i \hat{\boldsymbol{e}}_i f_0(\psi)\bar{\Theta}(\psi) + \sum_i \hat{\boldsymbol{e}}_i l_p(\boldsymbol{\nabla}\psi \cdot \hat{\boldsymbol{e}}_i)\partial_\psi(f_0\bar{\Theta}) \\ &+ \sum_i \hat{\boldsymbol{e}}_i f_0(\psi_i)\delta\Theta_i, \end{aligned} \tag{3.4}$$

see [78]. The pili direction vectors $\hat{\boldsymbol{e}}_i$ can be rewritten in terms of the microorganism orientation axis vector $\hat{\boldsymbol{n}}$ (see fig. 3.4) and the vector orthogonal to the long microorganism axis $\hat{\boldsymbol{n}}^\perp = \hat{\boldsymbol{e}}_z \times \hat{\boldsymbol{n}}$, reading $\hat{\boldsymbol{e}}_i = \cos\vartheta_i \hat{\boldsymbol{n}} + \sin\vartheta_i \hat{\boldsymbol{n}}^\perp$ [78]. As

mentioned before, it is reasonable to assume that the pili are approximately symmetrically distributed around the microorganism tip (in case of a strong asymmetry the pili would generate a strong net torque in one preferred direction and the microorganism would rotate around oneself), and hence we can neglect terms in the above equation that sum over odd quantities, like $\langle \sin\vartheta_i \rangle = \frac{1}{N}\sum_i \sin\vartheta_i$ or $\langle \cos\vartheta_i \sin\vartheta_i \rangle = \frac{1}{N}\sum_i \cos\vartheta_i \sin\vartheta_i$ [78]. The above equation then reads

$$\begin{aligned}\boldsymbol{F} =& N\langle\cos\vartheta_i\rangle f_0(\psi)\bar{\Theta}(\psi)\hat{\boldsymbol{n}} + N\langle\sin^2\vartheta_i\rangle\ell_p\partial_\psi\left(f_0(\psi)\bar{\Theta}(\psi)\right)\left(\boldsymbol{\nabla}\psi\cdot\hat{\boldsymbol{n}}^\perp\right)\hat{\boldsymbol{n}}^\perp \\ &+ N\langle\cos^2\vartheta_i\rangle\ell_p\partial_\psi\left(f_0(\psi)\bar{\Theta}(\psi)\right)(\boldsymbol{\nabla}\psi\cdot\hat{\boldsymbol{n}})\,\hat{\boldsymbol{n}} \\ &+ \hat{\boldsymbol{n}}\sum_i \cos\vartheta_i f_0(\psi_i)\delta\Theta_i + \hat{\boldsymbol{n}}^\perp\sum_i \sin\vartheta_i f_0(\psi_i)\delta\Theta_i\end{aligned} \tag{3.5}$$

If the attachment events of two different pili are independent of each other we have $\langle\delta\Theta_i(t)\delta\Theta_j(t)\rangle = \sigma^2(\psi)\delta_{ij}$, where δ_{ij} is the Kronecker symbol [78]. Moreover, we can calculate the auto-correlation of the attachment as $\langle\delta\Theta_i(t)\delta\Theta_j(t')\rangle = \sigma^2(\psi)\delta_{ij}e^{-(\lambda+\mu)|t-t'|}$ [78]. In our derivation we are interested in time scales much longer than the average attachment/detachment times, and hence we can approximate this auto-correlation as a delta function

$$\langle\delta\Theta_i(t)\delta\Theta_j(t')\rangle \approx \frac{\sigma^2(\psi)}{\lambda(\psi)+\mu(\psi)}\delta_{ij}\delta(t-t') = \frac{\lambda(\psi)\mu(\psi)}{\left[\lambda(\psi)+\mu(\psi)\right]^3}\delta_{ij}\delta(t-t') \tag{3.6}$$

[78]. With this we get for the mean square fluctuations parallel to $\hat{\boldsymbol{n}}$

$$\begin{aligned}&\left\langle \left(\hat{\boldsymbol{n}} \sum_i \cos\vartheta_i f_0(\psi_i)\delta\Theta_i(t)\right)^2\right\rangle = \sum_i \cos^2\vartheta_i f_0^2(\psi_i)\sigma^2(\psi_i) = \\ &N\langle\cos^2\vartheta_i\rangle f_0^2(\psi)\sigma^2(\psi) + N\langle\cos^3\vartheta_i\rangle \ell_p \partial_\psi (f_0^2(\psi)\sigma^2(\psi))(\boldsymbol{\nabla}\psi\cdot\hat{\boldsymbol{n}}).\end{aligned} \tag{3.7}$$

Analogously, for the mean square fluctuations parallel to $\hat{\boldsymbol{n}}^\perp$ we get

$$\begin{aligned}&\left\langle \left(\hat{\boldsymbol{n}}^\perp \sum_i \sin\vartheta_i f_0(\psi_i)\delta\Theta_i(t)\right)^2\right\rangle = \sum_i \sin^2\vartheta_i f_0^2(\psi_i)\sigma^2(\psi_i) = \\ &N\langle\sin^2\vartheta_i\rangle f_0^2(\psi)\sigma^2(\psi) + N\langle\sin^2\vartheta_i\cos\vartheta_i\rangle \ell_p \partial_\psi (f_0^2(\psi)\sigma^2(\psi))(\boldsymbol{\nabla}\psi\cdot\hat{\boldsymbol{n}}).\end{aligned} \tag{3.8}$$

[78]. In a scenario where $f_0(\psi)\sigma(\psi)$ is only weakly dependent on the EPS concentration ψ, the gradient terms of the order of $|\boldsymbol{\nabla}\psi|$ can be neglected in the mean square fluctuations. But even in a more general case where the dependence on $|\boldsymbol{\nabla}\psi|$ is present, these terms will just slightly alter the fluctuation strengths in the parallel and perpendicular directions and are not expected to introduce any new phenomena or behaviour to the equations otherwise. For this reason, in our derivation we will neglect the gradient dependence of the fluctuations but keep them in the deterministic part of eq. (3.5) [78].

Furthermore, as the attachment/detachment of pili is modeled as a set of N random independent events, we can expect that the overall fluctuations can be well

approximated by a Gaussian for $N \gg 1$ [78]. Hence, we will model the fluctuations in attachment in terms of Gaussian Langevin noise parallel and perpendicular to the microorganism body axis $\hat{\boldsymbol{n}}$, i.e.

$$\begin{aligned}\boldsymbol{F} =& N\langle\cos\vartheta_i\rangle f_0(\psi)\bar{\Theta}(\psi)\hat{\boldsymbol{n}} + N\langle\sin^2\vartheta_i\rangle\ell_p\partial_\psi\left(f_0(\psi)\bar{\Theta}(\psi)\right)\left(\boldsymbol{\nabla}\psi\cdot\hat{\boldsymbol{n}}^\perp\right)\hat{\boldsymbol{n}}^\perp \\ &+ N\langle\cos^2\vartheta_i\rangle\ell_p\partial_\psi\left(f_0(\psi)\bar{\Theta}(\psi)\right)(\boldsymbol{\nabla}\psi\cdot\hat{\boldsymbol{n}})\,\hat{\boldsymbol{n}} \\ &+ N\sqrt{\frac{\langle\cos^2\vartheta_i\rangle f_0^2(\psi)\sigma^2(\psi)}{\lambda(\psi)+\mu(\psi)}}\eta_\parallel\hat{\boldsymbol{n}} + N\sqrt{\frac{\langle\sin^2\vartheta_i\rangle f_0^2(\psi)\sigma^2(\psi)}{\lambda(\psi)+\mu(\psi)}}\eta_\perp\hat{\boldsymbol{n}}^\perp\end{aligned} \tag{3.9}$$

where $\langle\eta_{\parallel/\perp}\rangle = 0$, $\langle\eta_\parallel(t)\eta_\parallel(t')\rangle = \delta(t-t')$, $\langle\eta_\perp(t)\eta_\perp(t')\rangle = \delta(t-t')$ and $\langle\eta_\parallel(t)\eta_\perp(t')\rangle = 0$ [78].

The force generated by the pili acts on the tip of the microorganism and will hence both propel and rotate it. In a viscous environment we can neglect inertial effects and consider the centre-of-mass velocity as proportional to the force [78]. This leads to the equation

$$\begin{aligned}\frac{d\boldsymbol{r}}{dt} &= \frac{1}{\gamma_\parallel}\boldsymbol{F}_\parallel + \frac{1}{\gamma_\perp}\boldsymbol{F}_\perp = v(\psi)\hat{\boldsymbol{n}} + A(\psi)(\boldsymbol{\nabla}\psi\cdot\hat{\boldsymbol{n}}^\perp)\hat{\boldsymbol{n}}^\perp + B(\psi)(\boldsymbol{\nabla}\psi\cdot\hat{\boldsymbol{n}})\hat{\boldsymbol{n}} \\ &+ \sqrt{2D_\parallel}\,\eta^\parallel\hat{\boldsymbol{n}} + \sqrt{2D_\perp}\,\eta^\perp\hat{\boldsymbol{n}}^\perp,\end{aligned} \tag{3.10}$$

Since the noise strengths $\sqrt{2D_\parallel}$ and $\sqrt{2D_\perp}$ in general depend on the local EPS concentration $\psi(\boldsymbol{r})$, the above equation is incomplete without resolving the ambiguity

where the noise should be evaluated. As highlighted in [79], a stochastic differential equation could be interpreted in an Itô or in a Stratonovich sense, or as something in-between. Phrasing the problem in Itô notation [1], we need to have an a priori rule from the microscopic dynamics at which position $\boldsymbol{r} + \alpha d\boldsymbol{r}$ the noise should be evaluated ($\alpha = 0$ corresponds to the Itô approach, whereas $\alpha = 1/2$ for Stratonovich) within an infinitesimal time step dt [78]. Here, a general interpretation with $\alpha \neq 0$ modifies the prefactors $A(\psi)$ and $B(\psi)$. In Itô notation, the prefactors in eq. (3.10) read [78]:

$$
\begin{aligned}
D_{\parallel}(\psi) &= \frac{N}{2} \left\langle \cos^2 \vartheta_i \right\rangle \frac{f^2(\psi)}{\gamma_{\parallel}^2} \frac{\lambda(\psi)\mu(\psi)}{[\lambda(\psi)+\mu(\psi)]^3}, \\
D_{\perp}(\psi) &= \frac{N}{2} \left\langle \sin^2 \vartheta_i \right\rangle \frac{f^2(\psi)}{\gamma_{\perp}^2} \frac{\lambda(\psi)\mu(\psi)}{[\lambda(\psi)+\mu(\psi)]^3}, \\
v(\psi) &= N \left\langle \cos \vartheta_i \right\rangle \frac{f(\psi)}{\gamma_{\parallel}} \frac{\lambda(\psi)}{\lambda(\psi)+\mu(\psi)}, \\
A(\psi) &= N \left\langle \sin^2 \vartheta_i \right\rangle \frac{\ell_p}{\gamma_{\perp}} \partial_{\psi} \left[f(\psi) \frac{\lambda(\psi)}{\lambda(\psi)+\mu(\psi)} \right] + \alpha \partial_{\psi} D_{\perp}(\psi), \\
B(\psi) &= N \left\langle \cos^2 \vartheta_i \right\rangle \frac{\ell_p}{\gamma_{\parallel}} \partial_{\psi} \left[f(\psi) \frac{\lambda(\psi)}{\lambda(\psi)+\mu(\psi)} \right] + \alpha \partial_{\psi} D_{\parallel}(\psi).
\end{aligned}
\tag{3.11}
$$

Since the pulling force acts on the microorganism tip $\boldsymbol{r}_0$, it will also generate a torque on the microrganism:

$$
\boldsymbol{\tau} = \frac{\ell}{2} \hat{\boldsymbol{n}} \times \boldsymbol{F} = \frac{\gamma \ell}{2} \hat{\boldsymbol{n}} \times \left[A(\psi)(\boldsymbol{\nabla}\psi \cdot \hat{\boldsymbol{n}}^{\perp})\hat{\boldsymbol{n}}^{\perp} + \sqrt{2D_{\perp}}\, \eta^{\perp} \hat{\boldsymbol{n}}^{\perp} \right]. \tag{3.12}
$$

[1] i.e. evaluating all the terms at $\boldsymbol{r}$ but keeping track of additional terms that enter if we evaluate $\psi(\boldsymbol{r} + \alpha d\boldsymbol{r})$ at $\alpha \neq 0$ at each time step

In a viscous environment inertial effects can be neglected and the angular velocity $\boldsymbol{\omega}$ will be proportional to the torque,

$$\frac{d\hat{\boldsymbol{n}}}{dt} = -\hat{\boldsymbol{n}} \times \boldsymbol{\omega} = -\frac{1}{\gamma_{\text{rot}}}\, \hat{\boldsymbol{n}} \times \boldsymbol{\tau} = -\chi(\psi)\hat{\boldsymbol{n}} \times [\hat{\boldsymbol{n}} \times \boldsymbol{\nabla}\psi] + \sqrt{2D_r(\psi)}\, \eta^{\perp}\hat{\boldsymbol{n}}^{\perp}. \quad (3.13)$$

The other parameters in eq. (3.13) are:

$$\chi(\psi) = \frac{\ell\ell_p}{2\gamma_{\text{rot}}} N \langle \sin^2 \vartheta_i \rangle \partial_\psi \left[f(\psi)\, \frac{\lambda(\psi)}{\lambda(\psi) + \mu(\psi)} \right] + \alpha \partial_\psi D_r, \quad (3.14a)$$

and

$$D_r = \left(\frac{\gamma_\perp \ell}{2\gamma_{\text{rot}}} \right)^2 D_\perp. \quad (3.14b)$$

For the multiplicative noise in eq. (3.13), we choose a general interpretation $\alpha \neq 0$. It is important to note that the rotational noise is proportional to $\eta_\perp$, meaning that the same stochastic fluctuations in the perpendicular direction will move the microorganism and rotate it at the same time, increasing the correlation between trajectory and body orientation. In our simulations we have taken into account the common origin of the translational and rotational noise.

We can express all the system constants in terms of $v(\psi)$ and $D_r(\psi)$ as

$$
\begin{aligned}
D_{\parallel}(\psi) &= \left[\frac{4\gamma_{\rm rot}^2 c_2}{\ell^2\gamma_{\parallel}^2(1-c_2)}\right] D_r(\psi), \\
D_{\perp}(\psi) &= \left(\frac{2\gamma_{\rm rot}}{\gamma_{\perp}\ell}\right)^2 D_r(\psi), \\
\chi(\psi) &= \left[\frac{\gamma_{\parallel}\ell\ell_p(1-c_2)}{2\gamma_{\rm rot}c_1}\right] \partial_\psi v(\psi) + \alpha\partial_\psi D_r(\psi), \\
A(\psi) &= \left[\frac{\ell_p(1-c_2)\gamma_{\parallel}}{c_1\gamma_{\perp}}\right] \partial_\psi v(\psi) + \alpha\left(\frac{2\gamma_{\rm rot}}{\gamma_{\perp}\ell}\right)^2 \partial_\psi D_r(\psi), \\
B(\psi) &= \left[\frac{\ell_p c_2}{c_1}\right] \partial_\psi v(\psi) + \alpha\left[\frac{4\gamma_{\rm rot}^2 c_2}{\ell^2\gamma_{\parallel}^2(1-c_2)}\right] \partial_\psi D_r(\psi),
\end{aligned}
\tag{3.15}
$$

where $c_1 = \langle\cos\vartheta_i\rangle$ and $c_2 = \langle\cos^2\vartheta_i\rangle$ are assumed to be Psl independent [78].

The equations above, describing the microorganism motion in response to the EPS field ψ, have been microscopically derived. But we also need to specify the shape of the trail which the microorganisms secrete. For the largest part of the paper, we will assume that the deposited trail has a Gaussian shape with a thickness δ, which approximately corresponds to the thickness of the microorganism, in consistency with the assumption that the deposited EPS is sticky and does not diffuse very much.

$$
\partial_t\psi(\boldsymbol{r}_i, t) = k\sum_i \frac{1}{2\pi\delta^2}\exp[-(\boldsymbol{r}-\boldsymbol{r_i})^2/2\delta^2] \tag{3.16}
$$

Our choice of a Gaussian for the microorganism's EPS trail is motivated by the assumption that EPS just secreted from the microorganism pores will initially diffuse but then the diffusion will come to an effective stop due to the stickiness of exopolysac-

charides. Similar models have been applied in previous studies [62]. However, we expect that the qualitative dynamics of the microorganisms will not majorly depend on the trail shape chosen, as long as the trail has a finite thickness approximately corresponding to the microorganism thickness. In particular, other trail shapes – like e.g. rectangular or triangular trails – are more easily analytically tractable and can provide interesting insights.

3.4 Simplified Model Equations

If we compare the above equations (3.10) and (3.13) to (2.1), we will in particular notice that the dependence on the chemotactic gradient $\nabla\psi$ here not only enters in the positional, but also in the orientational differential equation. The reason for this is the anisotropy of the pili distribution around the microorganism, sketched in fig. 3.4 for P. Aeruginosa, where all the pili are distributed around one bacterial pole. The form of this term suggests that the bacterium will try to align with the direction of a gradient. If a microorganism enters an already existing trail, it will initially try to orient itself orthogonally to the trail because the EPS gradient would point inwards. But once it reaches the center of the trail function, the trail gradient will change signs and rotate the microorganism in the opposite direction. As a result, one possible consequence of trail alignment could be oscillatory trail-following, where the microorganism would oscillate between trail boundaries but on the average be aligned with the trail.

Autochemotaxis is a different effect that would influence the dynamics. If the EPS-producing pores are distributed around the whole microorganism body, we can expect that the microorganisms will also interact with their own trails. Other than in the previous scenario of following a self-deposited trail, the microorganisms will often be "in the center" of their own trail, where $\nabla\psi \approx 0$ and thus they initially might not be able to feel the alignment effects of their trail. However, as the interaction strength χ and the noise increase, the microorganisms might sense small deviations from the center of the trail, or they might sense the boundaries of the previously self-deposited trail, which might cause changes of direction and rotations.

In this section, we will try to better understand possible effects of trail alignment for a single microorganism. To do this, we will regard a simplified version of the above model. To isolate the effects of the alignment term from other effects, we will simplify eq. (3.10) to

$$\frac{d\boldsymbol{r}(t)}{dt} = v_0\hat{\boldsymbol{n}} \tag{3.17a}$$

and keep (3.13) as:

$$\frac{d\hat{\boldsymbol{n}}}{dt} = -\chi\hat{\boldsymbol{n}} \times [\boldsymbol{n} \times \boldsymbol{\nabla}\psi] + \sqrt{2D_r}\eta\hat{\boldsymbol{n}}^{\perp} \tag{3.17b}$$

This approximation is valid if the term $v_0\hat{\boldsymbol{n}}$ is much larger than all the other

terms in eq. (3.10). This is true if the pulling force of a single pilus i, $f_0(\psi_i) \approx f_{\text{const}} + f_{01}(\psi_i)$, has a dominant, Psl-independent contribution $f_{\text{const}} \gg f_{01}(\psi_i)$. While this will in general not be the case, such a model simplification is helpful for a better understanding of the effects of trail alignment.

3.5 Effective Autochemotaxis of Trail-Secreting Cells

We will first discuss the effect of auto-chemotaxis in terms of the simplified model for microorganism movement introduced in the section above. This section will be based on the article by Kranz, Gelimson, Zhao, Wong, and Golestanian [77]. For this publication, Till Kranz carried out the analytical calculations for mean squared displacements, based on the simplified model described above derived by Anatolij Gelimson. Kun Zhao and Gerard Wong provided experimental data for the angle distributions. Anatolij Gelimson provided simulations for the angle distrubutions shown in the paper and also carried out simulations to investigate the limit of strong coupling between microorganism and trail, which could not be accessed analytically. The whole work was supervised by Ramin Golestanian, who contributed to all parts of the publication.

As a starting point, we take the simplified model above, given by eqs. (3.17a) and (3.17b). We can rewrite eq. (3.17b) for the microorganism orientation $\hat{\boldsymbol{n}} = (\cos\varphi, \sin\varphi)$ in terms of the orientation angle φ as

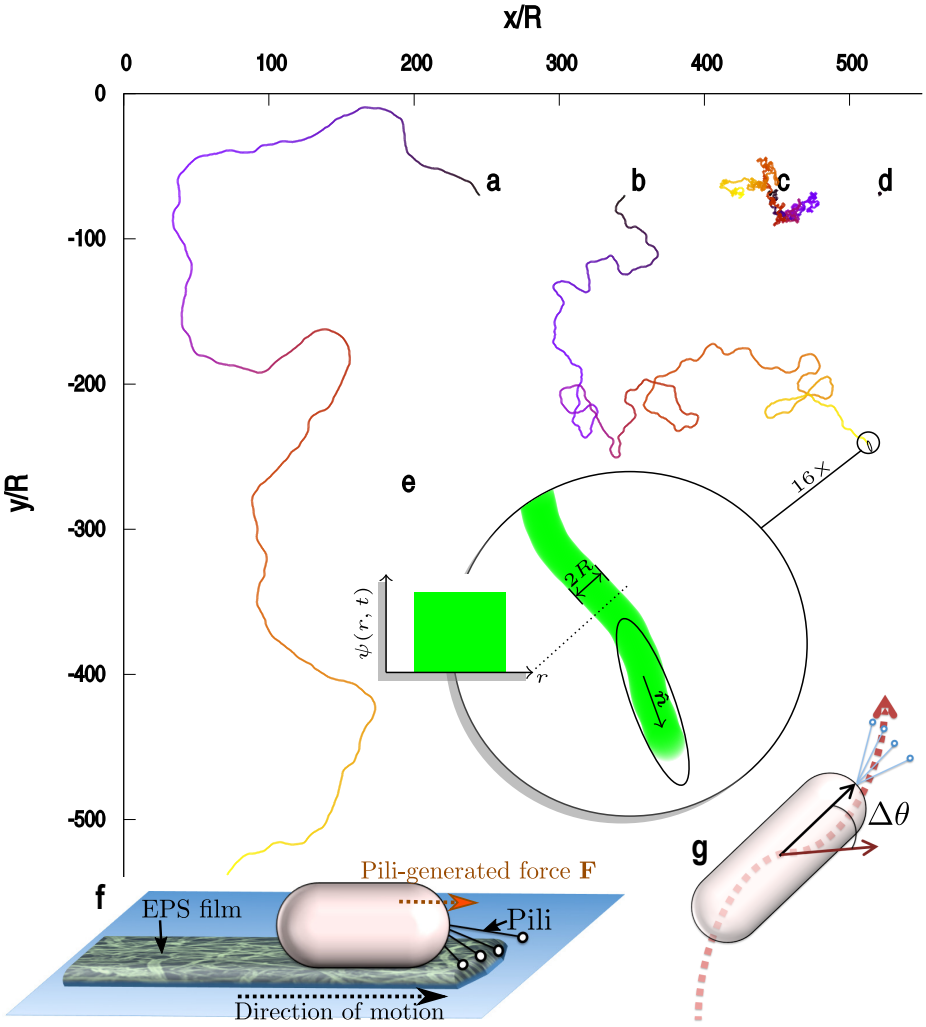

Figure 3.5: (a-d) show example realizations of microorganism trajectories for the rectangular trail model. The rotational diffusion constant was set to $D_r = 10^{-2}/\tau$. The effective interaction strength between the Psl trail and the microorganism orientation Ω is varied between (a) $\Omega\tau = 0$, (b) $\Omega\tau = 1.2$ and (c) $\Omega\tau = 1.85$ (slightly below the localization transition), and (d) $\Omega\tau = 2.15$ (above the localization transition). (e) shows the deposited rectangular trail and the bacterial orientation vector, (f) shows a schematic interaction between the exopolysaccharide/Psl film and the bacterial pili and (g) depicts a sketch of the angle $\Delta\theta$ [see also fig. 3.3 and [77]]. Taken with permission from [77]

$$\frac{d\varphi}{dt} = \chi \partial_{\perp}\psi(\boldsymbol{r}(t), t) + \eta(t) \tag{3.18a}$$

where $\partial_{\perp}\psi(\boldsymbol{r}(t), t) = \hat{\boldsymbol{n}}^{\perp} \cdot \nabla\psi(\boldsymbol{r}(t), t)$ and $\langle \eta(t)\eta(t') \rangle = 2D_r\delta(t - t')$ [77].

For the shape of the trail function deposited by a single microorganism located at $\boldsymbol{r}(t)$, to simplify calculations, we will choose

$$\partial_t\psi(\boldsymbol{r}', t) = k\mathcal{H}\left(\delta^2 - |\boldsymbol{r}' - \boldsymbol{r}(t)|^2\right)/\pi\delta^2 \tag{3.18b}$$

where $\mathcal{H}(r)$ denotes the Heaviside step function and 2δ is the thickness of the trail [77]. This rectangular trail defines a microscopic time scale $\tau = \delta/v_0$ as a characteristic time for the microorganism to cross a trail [77]. Example trajectories of this model for $D_r\tau = 10^{-2}$, as well as a schematics of the rectangular trail and Psl deposition, is shown in fig. 3.5.

After a short-time expansion of eqs. (3.17a) and (3.18b), one finds the stochastic integral equation [77]

$$\partial_{\perp}\psi(t) = \frac{\Omega}{\tau}\int_0^{\tau} du(\tau - u)\left[\partial_{\perp}\psi(t - u) + \eta(t - u)/\chi\right] \tag{3.19}$$

where $\Omega = k\chi\tau/\pi R^3$ is an effective interaction strength. For an explicit calculation

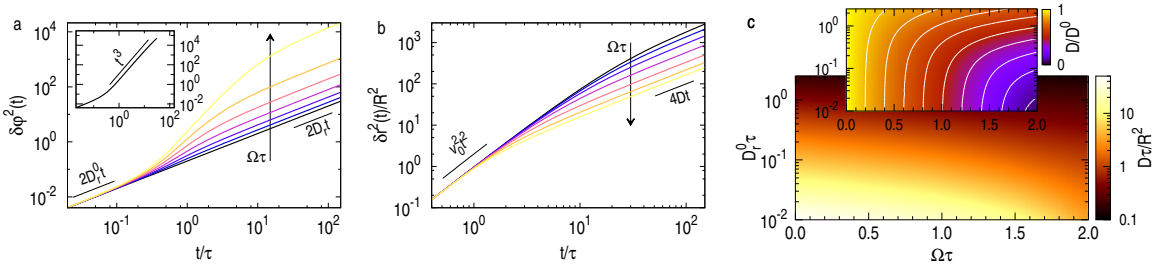

Figure 3.6: (a) Rotational and (b) translational mean squared displacement normalized by the trail width R (here: δ) as a function of non-dimensional time τ, for different Psl interaction strengths $\Omega = 0,\ 0.4,\ 0.7,\ 1.0,\ 1.53,\ 1.6,\ 1.9$. The rotational diffusion constant is set to $D_r\tau = 0.1$. As the inset of (a) shows, for intermediate timescales the rotational MSD can be superdiffusive (and even superballistic). For short and long times, however, the mean squared displacement is always diffusive. (c) shows the dependence of the effective diffusion constant D (called D^{eff} in this thesis) on the initial rotational diffusion D_r and on the Psl interaction strength Ω. In the inset we see how Psl deposition modifies the effective diffusion coefficient. D in this graphics corresponds to the effective diffusion and $D^0 = v_0^2/2D_r$ is the translational diffusion constant in absence of an EPS trail. One can see that for $\Omega\tau \to 2$ the diffusion decreases significantly [77]. Taken with permission from [77]

of this, see [77]. A Fourier transformation of eq. (3.19) gives

$\chi\partial_\perp\psi(\omega) = [\lambda^{-1}(i\omega) - 1]\tilde{\eta}(\omega)$ with [77]

$$\lambda(i\omega) = 1 - \frac{\Omega\tau}{i\omega\tau}\left[1 + \frac{1}{i\omega\tau}(e^{-i\omega\tau} - 1)\right] \tag{3.20}$$

This result can be plugged into eq. (3.18a), which gives $\frac{d\varphi}{dt} = \Xi(t)$ with $\tilde{\Xi}(\omega) = \tilde{\eta}(\omega)/\lambda(i\omega)$ [77], which can be used to obtain an expression for the angular mean square displacement $\delta\varphi^2 = \langle(\varphi(t) - \varphi(0))^2\rangle$ and the translational mean square displacement $\delta r^2(t) = \langle(\boldsymbol{r}(t) - \boldsymbol{r}(0))^2\rangle$ [77].

Here, we will only briefly summarise the main results:

- The short-time expansion approximation breaks down for $\Omega\tau > 2$, meaning that we do not expect a steady-state motion for a strong coupling between trail and microorganism $\Omega\tau > 2$ [77]. Simulations show that $\Omega\tau > 2$ corresponds to the case where the microorganisms become trapped by their trail.

- The rotational mean square displacement (MSD) is initially diffusive with $\delta\varphi^2 = 2D_r t$ for small times ($t \ll \tau$), crosses over to a super-diffusive regime and then becomes asymptotically diffusive again for $t \gg \tau/(1 - \Omega\tau/2)$, $\delta\varphi^2 = 2D_r^{\text{eff}} t$, with an effective diffusion constant given by $D_r^{\text{eff}}/D_r = 1 + \Omega\tau/2 \frac{1+\Omega\tau/2}{(1-\Omega\tau/2)^2}$, which diverges for $\Omega\tau \to 2$, indicating trapping [77]. See fig. 3.6a for rotational MSD diagrams.

- The translational MSD is initially ballistic as $\delta r^2(t) = v_0^2 t^2$ for $t \ll \tau$, but then becomes diffusive with $\delta r^2(t) = 4Dt$ for larger times. For large rotational diffusions, $(D_r\tau)^{-1} < 1 + \Omega\tau/2$, the effective asymptotic diffusivity is given by $D^{\text{eff}}/D = \sqrt{\pi D_r/2\Omega} e^{D_r/2\Omega} \text{erfc}(\sqrt{D_r/2\Omega})$, where $D = v_0^2/2D_r$ [77]. See fig. 3.6b and c for translational MSD diagrams.

- For small rotational diffusions, $D_r\tau \ll 2[1 - \Omega\tau/2]^3/[2 - \Omega\tau + \Omega^2\tau^2/2]$, on the other hand, we asymptotically have

$$D^{\text{eff}}/D = D_r/D_r^{\text{eff}} \left[1 - \frac{D_r^2\tau^2}{6} \frac{\Omega\tau(1 + \Omega\tau/2)^3}{(1 - \Omega\tau/2)^6}\right] \tag{3.21}$$

- Close to the limit of strong EPS coupling the asymptotic diffusivity behaves as $D^{\text{eff}}/D = \Gamma(3/4)(D_r\tau)^{2/3} + D_r\tau/3$, i.e. it becomes independent of $\Omega\tau$ and

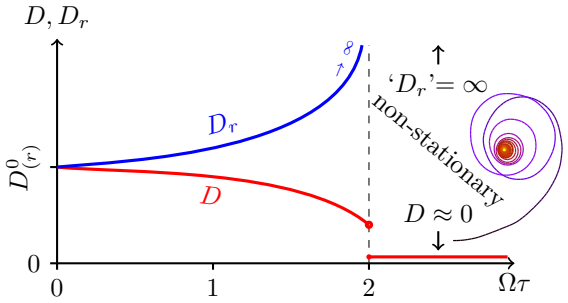

Figure 3.7: Schematic sketch of the effects of the EPS interaction Ω on the effective rotational and translational diffusion constants. While the rotational diffusion constant diverges for $\Omega\tau \to 2$, the translational diffusion is expected to go a constant value and drop to zero above the threshold $\Omega\tau > 2$ [77]. As shown in the numerical simulations, the expected behaviour at $\Omega\tau > 2$ in the long run is trapping, sketched here. Taken with permission from [77]

converges to a finite value for $\Omega\tau \to 2$ [77].

The crossover behaviour for rotational and translational MSD is visualised in figure 3.6. Figure 3.7 shows the dependence of the asymptotic diffusion constants on $\Omega\tau$ [77].

To further investigate the behaviour for the inaccessible regime $\Omega\tau > 2$ we implemented numerical simulations for the stochastic equations (3.18). On a computation cluster, we generated realisations of equations (3.18) using forward variable time-stepping.

As a basic timestep we chose $\mathrm{d}t = 0.01\tau$, but divided it into smaller steps whenever the change in angle was larger than $0.01\mathrm{rad}/\mathrm{d}t$. The simulation was carried out on a grid corresponding to $200\delta \times 200\delta$, with δ corresponding to the characteristic trail width. The grid had a resolution of 3600 points per δ^2. The other parameters were

chosen as $v_0 = 1\delta/\tau$ and $D_r = 0.01/\tau$.

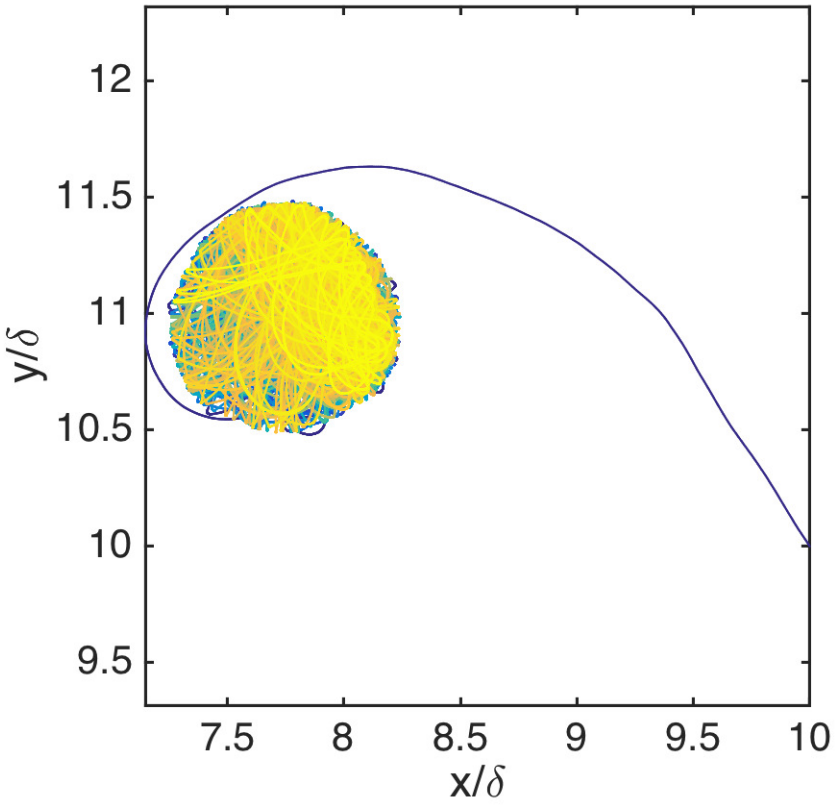

Figure 3.8: Simulation outcome for a typical microorganism trajectory above the trapping threshold $\Omega\tau > 2$. Here, $\Omega\tau = 2.01$. The other parameters were the same as in fig. 3.5, with $v_0 = \delta/\tau$ and $D_r\tau = 0.01$. The spatial resolution is 3600 points per δ^2. The numerical simulation was run for a time $T = 1000\tau$ over several realisations and the microorganism did not escape the self-deposited EPS trap. This suggests that $D^{\text{eff}} < \delta^2/1000\tau$, which is 5×10^5 times smaller than the diffusion constant D in absence of EPS deposition, in agreement with the conjecture that the microorganism becomes trapped for $\Omega\tau > 2$.

A typical resulting trajectory is shown in figure 3.8. Here, $\Omega = 2.01$. The color coding represents different times, with darker colors for short times and lighter colors for longer times. As we can see, while the motion initially is directional, the microorganism quickly becomes trapped in its own trail. The width of the self-generated trap

is of the same order as the trail radius $R = \delta$. Within the long simulation time of $T = 1000\tau$ and over several realizations, the microorganism did not escape the trap, suggesting an effective diffusion constant $D^{\text{eff}} < \delta^2/1000\tau$, which is 5×10^5 times smaller than the diffusion constant D in absence of EPS deposition.

3.6 Simplified Model: Oscillatory Trail-Following and Orthogonal Trail Escapes

In the previous chapter we saw that the interaction with a self-deposited trail can lead to an enhanced rotational diffusion and transition to trapping for strong coupling between trail and microorganism. A mechanism to increase the local EPS concentration and to localize the microorganism is of utmost importance at the early stages of microcolony formation, since exopolysaccharides increase microorganism attachment to a surface and act as an attractant to other individuals [1].

However, if the self-deposited EPS film was to promote social colony formation, the bacteria should also be able to interact with the EPS trails of other bacteria, and preferentially find sites with a high EPS concentration. In this section, we will show that the model microorganisms are able to follow existing trails. The reason for this is that the Psl gradients perpendicular to a EPS trail face towards the inside of a trail. As a result, if a microorganism deviates from the center a trail it follows, the inward facing gradient will try to reorient the bacterium towards the inside again. As we will show in this section, this can result in oscillatory trail following with an oscillation frequency that is dependent on the EPS coupling strength.

But the possible effects of the alignment term in eq. (3.17b) are even more diverse: If the orientation of the microorganism becomes almost orthogonal with respect to the trail, for example due to noisy reorienation, the gradient alignment becomes very

weak, as can be seen from eq. (3.17b), enabling the microorganism to escape the trail.

To examine the mechanisms of trail following and escape, we have performed numerical simulations of the simplified model given in eqs. (3.17).

In the previous chapter we assumed that the microorganisms deposit a rectangular trail, see eq. (3.18b), for an easier analytic treatment. But while this was a good approximation for analytics, a more realistic EPS trail will have finite gradients rather than abrupt jumps at the boundaries. A plausible choice for a trail shape is a Gaussian, given by equation (3.16) [62]. Most of our numerical simulations in the following will assume a Gaussian trail, given by eq. (3.16). But for comparison of the trail shape effects, and for simpler analytical treatment, we will also regard a "triangular trail" (or cone-shaped trail) of the form:

$$\partial_t \psi(\boldsymbol{r}', t) = k \cdot \max\left(0, \delta - |\boldsymbol{r}' - \boldsymbol{r}(t)|\right) / \delta^3 \tag{3.22}$$

To better understand the range of possible interactions with existing trails deposited by other individuals, let us consider a simple geometry where a horizontal EPS trail already exists on a surface, fig. 3.9 and where a microorganism interacts with the existing trail according to equations (3.17). One can see that, in the case of a low rotational diffusion D_r (here, $D_r = 0.01/\tau$) and a sufficiently large interaction strength χ, the microorganisms can follow the existing trail in an oscillatory manner,

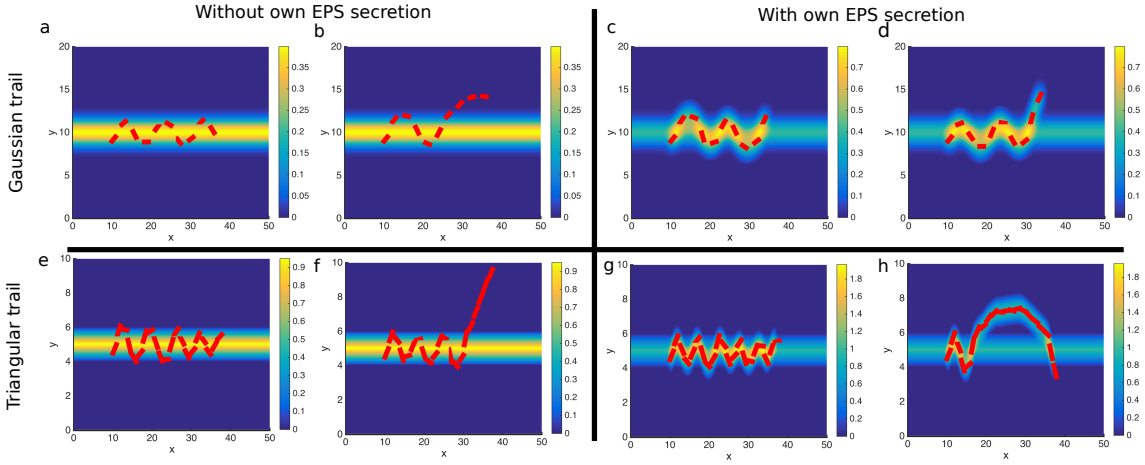

Figure 3.9: Typical behaviour around an existing EPS trail, located at $y = 5\delta$. (a-d) show random microorganism oscillations and escape events for a Gaussian trail, whereas in (e-h) typical oscillation and escape events are shown in the case of a triangular trail. In (a)–(b) and (e)–(f) the microorganism is interacting with the existing EPS trail only and does not secrete its own EPS, whereas in (c–d) and (g)–(h) the microorganism also deposits its own trail. The simulation parameters are $D_r = 0.01/\tau$, $\delta = 1$, $v_0 = 1\delta/\tau$. In the case of no own trail secretion, (a, b, e, f) we have $k = 0/\tau$, whereas microorganisms secreting their own EPS are assumed to do so at a rate $k = 1/\tau$. In (a-d), Gaussian trail, we have $\chi = 1.5\delta^3/\tau$ and in (e-h), triangular trail, we have $\chi = 0.5\delta^3/\tau$. These two values were chosen such that the average effective interaction with the trail is approximately the same for a triangular and a gaussian trail.

or escape the trail.

The oscillations observed in fig. 3.9 are of particular interest – at first sight, eq. (3.17b) would suggest that the microorganism would align itself with the EPS gradient it senses, i.e. perpendicular to an existing trail. While this is true and can lead to an escape event, there is also the scenario that the microorganism will follow the existing trail and where EPS gradients at the trail boundaries will stabilize the trail-following in an oscillatory manner.

To gain a better understanding of different dependencies, let's neglect the noise contribution in eq. (3.17) and regard a bacterium that does not secrete any EPS and follows a horizontal triangular trail located at $y = 0$. This calculation is analogous to the one in [80]:

$$\frac{\partial \boldsymbol{r}(t)}{\partial t} = \frac{\partial}{\partial t}(x(t), y(t))^T = v_0(\cos(\varphi), \sin(\varphi))^T \tag{3.23a}$$

$$\frac{\partial \varphi}{\partial t} = \chi \partial_\perp \psi(\boldsymbol{r}(t), t) = \chi \partial_y \psi \cos(\varphi) \tag{3.23b}$$

If the microorganism is located inside the triangular trail it will perceive $\partial_y \psi$ as a constant. If we, for simplicity, assume that the bacterium is located inside the lower half of the trail, the equation will simplify to $\frac{d\theta}{dt} = \Xi \cos(\theta)$, with $\Xi = \chi \partial_y \psi$. This equation can be solved by separating variables and gives

$$\varphi(t) = 2\arctan\left[\tan(\varphi_0/2 + \pi/4)e^{\Xi t}\right] - \pi/2 \tag{3.23c}$$

We can see immediately that the time the microorganism needs to change its direction will be of the order of $1/\Xi$ and that, if the microorganism did not encounter a gradient facing the opposite direction once it reached $y > 0$, it would align itself in the direction of $\partial_y \psi$, i.e. orthogonally to the trail.

If we plug the above expression for $\varphi(t)$ into eq. (3.23a) we get

$$x(t) = x_0 + \frac{2v_0}{\Xi}\left[\arctan\left(\tan(\varphi_0/2 + \pi/4)e^{\Xi t}\right) - \varphi_0/2 - \pi/4\right] \tag{3.23d}$$

and

$$y(t) = y_0 + v_0 t + \frac{v_0}{\Xi}\ln\left[\frac{\tan^2(\varphi_0/2 + \pi/4) + e^{-2\Xi t}}{\tan^2(\varphi_0/2 + \pi/4) + 1}\right] \tag{3.23e}$$

Let's regard different limits of these equations, as well as implications for the trail following model:

1. In the case that $\varphi_0 \approx \pi/2$, where the microorganism is aligned with the gradient, we have $\varphi(t) \to \pi/2$, $x \approx 0$ and $y(t) \approx y_0 + v_0 t$, i.e. a persistent walk in the gradient direction.

2. In the case of $\varphi_0 \approx -\pi/2$ the microorganism faces in the opposite direction of

the gradient. This implies $\varphi(t) \approx -\pi/2$ as long as $t \ll t_{\text{turn}} = -\frac{1}{\Xi}\ln(\tan(\varphi_0/2+\pi/4))$. This timescale goes to infinity for $\varphi(t) \to -\pi/2$. In this limit we will have $x(t) \approx x_0$ and $y = y_0 - v_0 t$. Thus, a microorganism which approximately faces in the opposite direction of the gradient will not feel the influence of the gradient and persistently walk in the direction $\varphi(t) \approx -\pi/2$ at a velocity v_0. In the case of a triangular trail this means that the microorganism will easily escape the trail if the time it would have needed for turning around is much larger than the time it takes for it to cross the trail, i.e. if $t_{\text{turn}} \gg \delta/v_0$

3. For intermediate values of φ_0 the timescale for an alignment with the gradient is given by $t_{\text{turn}} = -1/\Xi \ln(\tan(\varphi_0/2 + \pi/4))$, which is finite. If the microorganism walks towards the trail boundary and if $t_{\text{turn}} \lesssim \delta/v_0$, it will be turned towards the other side of the trail. Once it reaches the other side of the trail it will encounter a gradient in the opposite direction, which will turn it again towards the other side of the trail, resulting in oscillations. We can estimate that the amplitude Δy will be of the order of $\Delta y \sim \left| v_0 t_{\text{turn}} + v_0/\Xi \ln\left[\frac{\tan^2(\varphi_0/2+\pi/4)+e^{-\Xi t_{\text{turn}}}}{\tan^2(\varphi_0/2+\pi/4)+1}\right]\right| \approx v_0/\Xi \left|\ln\left(\tan(\varphi_0/2+\pi/4)\right)\right|$ and the period $\Delta x \sim 4\frac{v_0}{\Xi}\left|\arctan\left(\tan(\varphi_0/2+\pi/4)e^{\Xi t_{\text{turn}}}\right) - \varphi_0/2 - \pi/4\right| \approx 2\frac{v_0}{\Xi}|\varphi_0|$ for small φ_0.

The deterministic theory above is of course only expected for be valid in the case of small rotational noise D_r. For larger values of D_r we expect an increase in escape events from the existing horizontal trail (fig. 3.9). For small and intermediate noise values, however, we expect good agreement for a horizontal triangular trail and no self-secreted EPS. A comparison between theory and simulations is shown in fig.

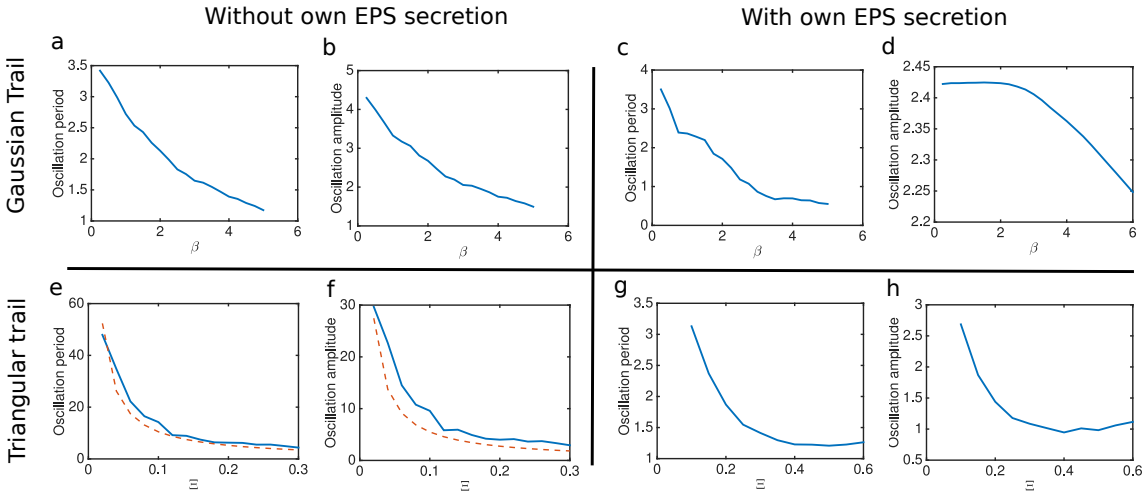

Figure 3.10: Oscillation amplitudes and periods for following an existing horizontal trail, see fig. 3.9, for different trail shapes and EPS coupling strengths, averaged over 100 runs of 100τ each. Only cases where the microorganisms were following the trail were counted, whereas trail escapes were discarded. The initial orientation is $\varphi_0 = \pi/6$ and $D_r = 0.01\tau$. (a-b) show the oscillation periods and amplitudes for a microorganism that follows the horizontal Gaussian trail but does not secrete EPS on its own. As expected from the deterministic theory, the amplitude and oscillation period decays with increasing coupling χ. (c-d) shows the same setup, but here the microorganisms are able to secrete their own EPS. One can see in (c) that the oscillation period is not greatly influenced by the self-secreted trail, presumably because the microorganism is always located at the center of its own trail, where $\nabla\psi_{\text{self}} \approx 0$ over the radius $\sim \delta = 1$.The Gaussian trail seems to introduce a regime where the oscillation amplitude is only weakly dependent on χ. (e-f) show the oscillation period and amplitude for an existing triangular trail and no own trail secretion. As predicted by the deterministic theory, both trail period and amplitude decay with increasing EPS coupling Ξ. The red dotted lines show the estimated values for (e) the period $\Delta x \sim 2\frac{v_0}{\Xi}|\varphi_0|$ and (f) the amplitude $\Delta y \sim \left|\ln\left(\tan(\varphi_0/2 + \pi/4)\right)\right|$. (g-h) a self-deposited triangular trail reduces both the oscillation periods and amplitudes by an order of 10. The reason is that the triangular trail shape introduces a gradient jump at the location of the microorganism. In (a-d), Gaussian trail, we have $\chi = 1.5\delta^3/\tau$ and in (e-h), triangular trail, we have $\chi = 0.5\delta^3/\tau$ (or $\Xi = 0.5/\tau$, since $\partial_y\psi = 1/\delta^3$). These two values were chosen such that the average effective interaction with the trail is approximately the same for a triangular and a gaussian trail.

3.10(e) and (f), where the red dotted lines correspond to the approximate values (e) $\Delta x \sim 2\frac{v_0}{\Xi}|\varphi_0|$ and (f) $\Delta y \sim \left|\ln\left(\tan(\varphi_0/2+\pi/4)\right)\right|$. The initial orientation in the simulations is $\varphi_0 = \pi/6$ and the rotational diffusion is $D_r = 0.01\tau$.

It is interesting to go beyond the approximation of a triangular trail and no self-deposited EPS and study other scenarios. Fig. 3.10 shows the oscillation periods and amplitudes for Gaussian and triangular trails, with and without self-secreted EPS in addition to a horizontal existing trail. In fig. 3.10 (a)–(d) the existing horizontal trail, as well as the self-deposited trail (c)–(d), are Gaussian. (a)–(b) show the oscillation periods and amplitudes for a microorganism that follows the horizontal Gaussian trail but does not secrete EPS on its own. In consistance with the deterministic theory, the amplitude and oscillation period decays with increasing coupling χ. (c)–(d) show the same setup, but here the microorganisms are able to secrete their own EPS. One can see in (c) that the oscillation period is not greatly influenced by the self-secreted trail, presumably because the microorganism is always located at the center of its own Gaussian trail, where $\nabla\psi_{\text{self}} \approx 0$ over the radius $\sim \delta = 1$. But interestingly, the self-deposited trail seems to significantly confine the microorganism.

In the case of a self-deposited triangular trail in addition to an existing triangular trail, both the amplitude and period drop by an order of 10 compared to the case of no EPS self-deposition, see fig. 3.10 (g)–(h). The reason is that the self-deposited EPS trail introduces a large gradient jump at the position of the microorganism. These steep gradients, which are always present around the microorganism as they are self-secreted, strongly disrupt the oscillatory behaviour, resulting in a shorter oscillation

period, smaller amplitudes and large fluctuations in amplitudes.

Figure 3.11 shows the effects rotational diffusion D_r can have on oscillations and periods. We see the same trends both for Gaussian (a-d) and triangular (e-h) trails – initially both oscillation amplitudes and periods sharply increase for increasing rotational diffusion. The reason is that random rotational noise disrupts the coherence of the oscillation and effectively decreases the influence of the gradient alignment term.

We also want to test our intuition that a microorganism will preferentially escape a trail at an angle of around 90°, since eq. (3.18a) implies that the EPS gradient of the existing trail will not be felt if the microorganism is oriented orthogonally to the gradient. In order to confirm this we ran a set of simulations where we placed the microorganism at the centre of the trail and varied the orientation between $\varphi_0 = 0°$ and $\varphi_0 = 180°$ degrees relative to the existing trail. For each degree in orientation the simulations was run 200 times for $t = 10\tau$ and we tracked the proportion of simulation runs where the microorganism escaped the trail (i.e. where $y(t) - y_{\text{trail center}} > 2\delta$). The results are shown in fig. 3.12.

Both for Gaussian and for triangular trails one can see that the optimal escape angle is $\varphi_0 = 90°$, with almost 100% escape events, fig. 3.12. But while for the Gaussian trail there are no major differences between the EPS-secreting and non-secreting individuals, fig. 3.12(a), there is a big difference for triangular trails, fig. 3.12(b). For flat angles relative to the trail, $\varphi_0 < 30°$ and $\varphi_0 > 150°$, the proportion of escape events is significantly enhanced, whereas for sharp angles $60° < \varphi_0 <$

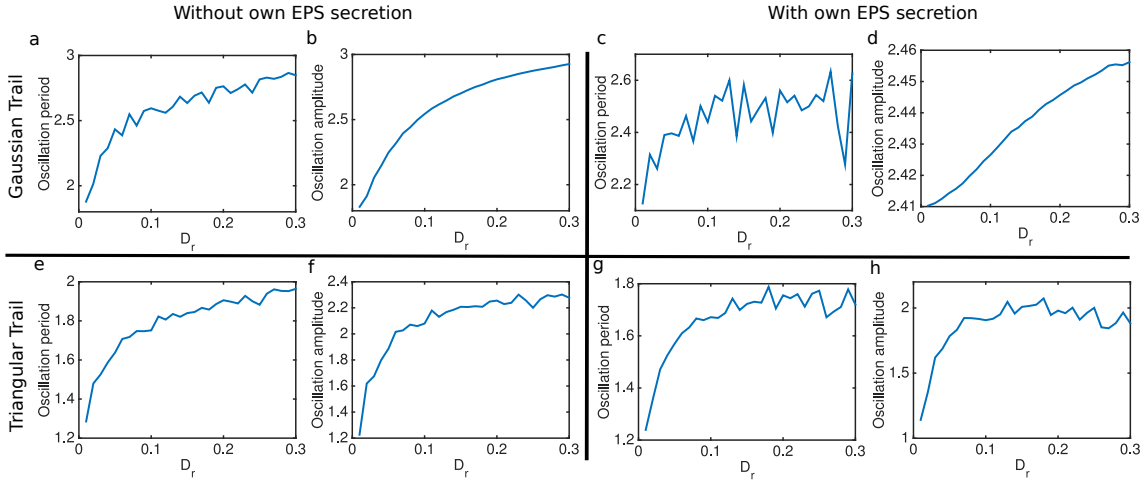

Figure 3.11: Oscillation amplitudes and periods for following an existing horizontal trail, see fig. 3.9, for different trail shapes and different values for the rotational diffusion D_r, averaged over 100 runs of 100τ each. The initial orientation is $\varphi_0 = \pi/6$ and D_r is varied between $0.01/\tau$ and $0.3/\tau$. (a)–(b) show the oscillation periods and amplitudes for a microorganism that follows the horizontal Gaussian trail but does not secrete EPS on its own. Rotational diffusion disrupts oscillations and hence amplitudes and periods increase with increasing diffusion. Eventually both amplitudes and periods saturate. (c)–(d) shows the same setup, but here the microorganisms are able to secrete their own EPS. One can see that the overall trend is the same, an increase in amplitude and period with increasing D_r, and eventually a saturation for large D_r. However, the increase of amplitudes and periods with increasing D_r is smaller since the additional self-deposited EPS trail can partly counteract the de-stabilizing effect of rotational diffusion on oscillations. (e)–(f) show the oscillation period and amplitude for an existing triangular trail and no own trail secretion. Also here both amplitude and period increase with D_r and eventually saturate, highlighting that rotational diffusion slightly de-correlates oscillations. (g-h) show that the same trend is preserved for trail-depositing microorganisms. In (a)–(d), Gaussian trail, we have $\chi = 1.5\delta^3/\tau$ and in (e)–(h), triangular trail, we have $\chi = 0.5\delta^3/\tau$. These two values were chosen such that the average effective interaction with the trail is approximately the same for a triangular and a gaussian trail.

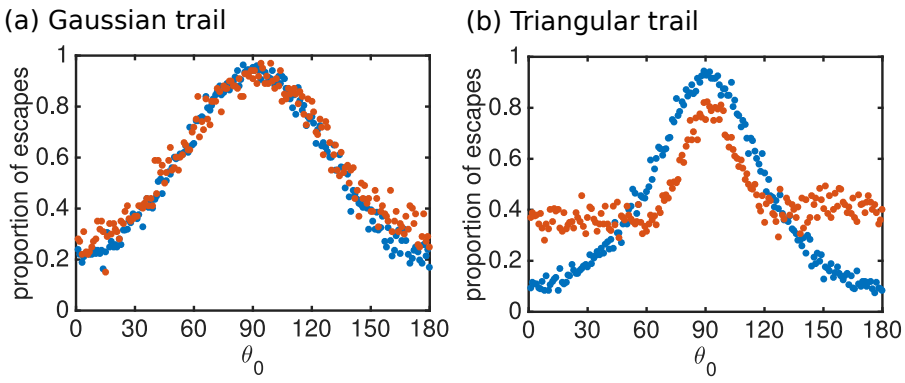

Figure 3.12: Proportion of escape events for a microorganism placed in the center of a trail, with a starting angle φ_0 varied between 0° and 180°. For each point we ran 200 simulations for $t = 10\tau$ each and counted the fraction of cases where the microorganism escapes the existing horizontal trail (escape events). Blue dots correspond to the case where the microorganism does not secrete EPS on its own, and for the red dots it deposits its own EPS trail in addition to the existing horizontal trail. (a) shows the data for Gaussian trails. As expected, the proportion of escape events peaks at $\varphi_0 = 90°$, and even almost becomes 100%. There is no major difference between EPS-secreting individuals and non-secreting ones. (b) shows the results for triangular trails. Also here the optimal escape angle is $\varphi_0 = 90°$, with almost 100% escape events. In the case of a trail-depositing organism the escape rate at small angles is significantly enhanced for flat angles, and slightly decreased for sharp angles. $\chi = 0.5\delta^3/\tau$ here both for triangular and rectangular trails

120° there are slightly lower escapes. The reason for this is that at the tip of the microorganism the self-deposited trail is cone-shaped, see eq. (3.22). Hence, at a flat angle the cone will partly cancel out the gradient of the existing trail, providing the microorganism a path to escape with less resistance. In the case of an initial orientation at a sharp angle, however, the cone will slightly enhance the gradient of the existing horizontal trail and thus make an escape slightly more difficult. However, the latter effect is small because the microorganism will not feel the EPS gradients very strongly if it is at a sharp angle relative to the gradient. Similar effects also seem to occur for a Gaussian trail, see fig. 3.12 (a), but they are weaker since the microorganism is located at the peak of a Gaussian and does not perceive the effects of its own trail as much.

3.7 Full Model: Trail Following and Trail Alignment

In this section we will briefly discuss the mechanisms how the full model derived in chapter 3.3 can lead to trail following. As in the section above, we will consider a geometry where a microorganism interacts with an existing trail. As an important difference compared to the simplified model, we now not only have a gradient alignment term proportional to χ, but also gradient-dependent displacement terms proportional to $A(\psi)$ and $B(\psi)$, which tend to displace the bacterium towards the center of the trail [78].

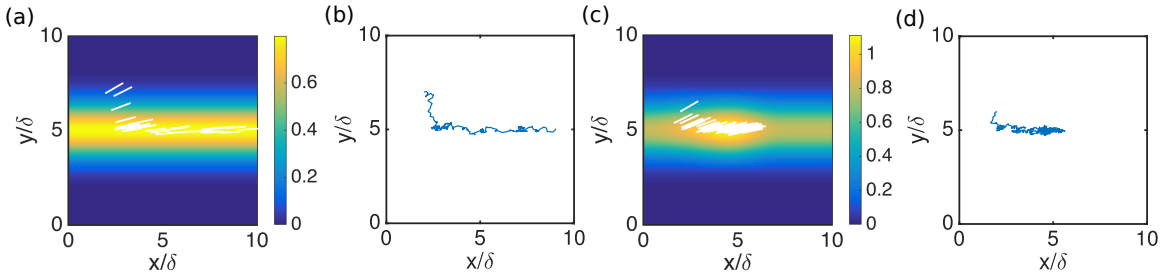

Figure 3.13: Typical behaviour of a bacterium around an existing horizontal Gaussian Psl trail, located at $y = 5\delta$. All parameters are derived from experiments, see chapter 3.8. (a) shows the Psl trail (color-coded) bacterial positions and orientations (white), taken every 0.15 s [78]. Starting from an off-trail position and an orientation of 30° away from the trail (top left), the microorganism quickly moves towards the trail, aligns and follows the trail. (b) shows the corresponding bacterial trajectory. (c) and (d) show the same setup, but take into account that a bacterium also secretes its own Psl trail. In this case the bacterium can also be slowed down in a Psl-rich region along the trail, enabling local accumulation and a rich-get-richer behaviour. [78]

A typical result can be seen in Fig. 3.9. Starting outside the center of an exisiting trail and facing away from the trail at an angle of 30° [top left in figs. 3.13(a)–(b)] the microorganism quickly moves towards the center of the trail, aligns with it and follows it. A similar behavior can also be observed in the case that a bacterium deposits its own Psl [Figs. 3.13 (c)–(d)], but the bacterium can also get trapped (or slowed down) on an existing trail, enabling a local accumulation of Psl in an already Psl-rich region [78].

As already seen for the simplified model, trail-following is possible because of the orientational term $\chi(\psi)\hat{\boldsymbol{n}} \times [\boldsymbol{n} \times \boldsymbol{\nabla}\psi]$ in eq. (3.13). The reason is that the term reorients the bacterium in the direction of the Psl gradient, i.e towards the inside of a trail. Also here, once the microorganism passes the trail center, the gradient changes signs and the alignment terms will try to reorient the microorganism towards the trail

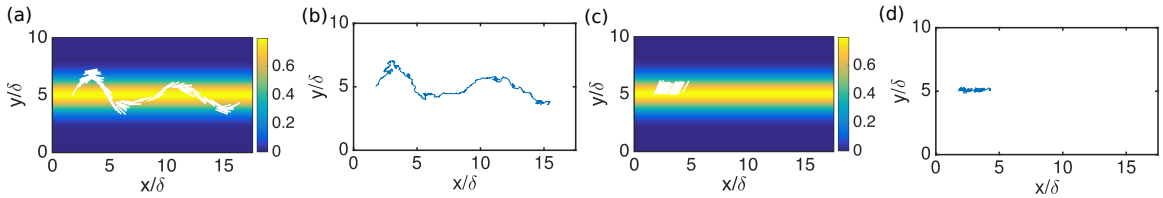

Figure 3.14: Typical behaviour of a bacterium around an existing Gaussian Psl trail (color-coded), located at $y = 5\delta$ [78]. Here we study the influence of the gradient alignment terms proportional to $\chi(\psi)$ and the displacement terms proportional to $A(\psi)$ and $B(\psi)$ separately. All parameters are derived from experiments, see chapter 3.8. Snapshots of bacterial positions and orientations (white) were taken every 0.15 s. In (a) and (b) only gradient alignment proportional to $\chi(\psi)$ is considered, by setting parallel and perpendicular displacement terms proportional to $A(\psi)$ and $B(\psi)$ to zero. [78] In (c) and (d) we set the $\chi(\psi)$ to zero and keep the terms proportional to $A(\psi)$ and $B(\psi)$ [78]. (a) As in the simplified model above, starting from an orientation of 30° away from the trail (left), the bacterium follows the trail in an oscillatory manner (b) shows the bacterial trajectory and oscillations along the trail. (c) and (d) shows a typical trajectory without the orientational alignment term but with the translational and rotational displacement terms proportional to $A(\psi)$ and $B(\psi)$. The bacterium can move to the center of the trail but trail following is decreased because the bacterium stays at a 30° angle relative to the trail and cannot reorient. Taken with permission from [78]

center again, resulting in oscillatory trail following [78].

But as an additional influence, the displacement terms $A(\psi)(\boldsymbol{\nabla}\psi \cdot \hat{\boldsymbol{n}}^{\perp})\hat{\boldsymbol{n}}^{\perp}$ and $B(\psi)(\boldsymbol{\nabla}\psi \cdot \hat{\boldsymbol{n}})\hat{\boldsymbol{n}}$ in eq. 3.10, try to maximize the local Psl concentration by moving the micrrorganism towards the peak of the Psl concentration, i.e. towards the center of an existing trail [78].

To examine the influence of the orientational alignment term and the gradient displacement terms separately, we first set the terms proportional to $A(\psi)$ and $B(\psi)$ to zero and keep the parameter $\chi(\psi)$. A typical outcome is shown in figs. 3.14(a) and (b), which shows oscillations and trail following. On the other hand, the terms proportional to $A(\psi)$ and $B(\psi)$ will move the bacterium towards the center of the trail, but the lack of reorientation does not allow efficient trail-following, see figs. 3.14 (c)–(d) and [78].

The sketch in fig. 3.15 summarises the influence of the algnment term and gradient-dependent displacement terms. The alignment term proportional to $\chi(\psi)$ leads to oscillations and trail-following (a). The displacement terms proportional to $A(\psi)$ and $B(\psi)$, in turn, are efficient in moving the microorganisms towards the trail center, but are unable to promote efficient movement along the trail (b).

The combination of gradient-dependent displacement and alignment with the gradient constitutes a robust mechanism for the attraction of bacteria to existing Psl trails and for the movement along Psl-rich regions.

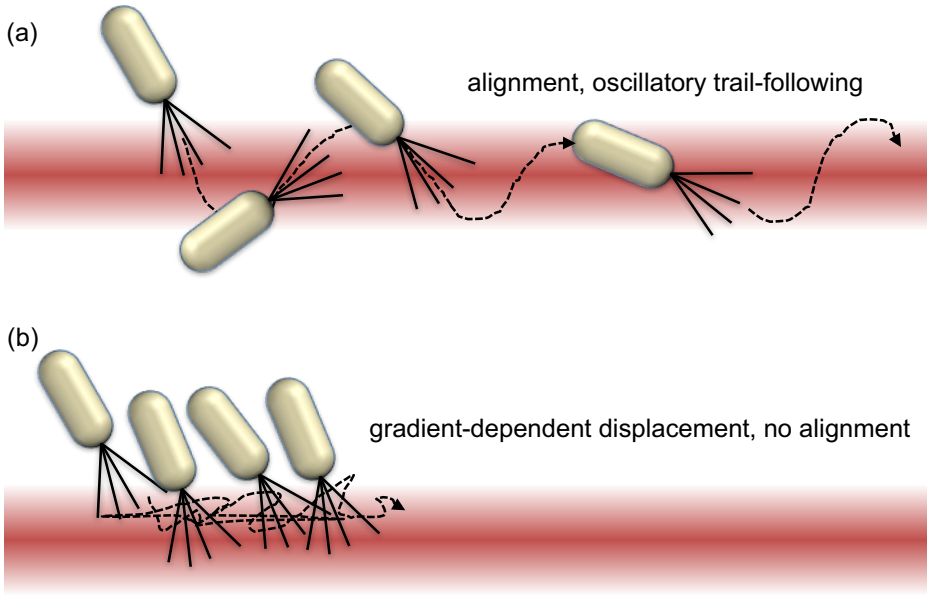

Figure 3.15: Sketch of the influence of gradient alignment (a), versus gradient displacement (b). While gradient alignment reorients the microorganism and enables trail-following (a), gradient displacement moves the microorganism towards the trail center but is unable to promote trail-following by itself.

3.8 Comparison of Experiments and Theory for Single Bacteria

In the following we will compare the general Type-IV pili model with experiments. In this section we will directy relate the model constants to experimental observables of motion for single P. Aeruginosa bacteria, see section 3.1 and [1]. For this we will regard the full model for the motion of a single pili-propelled microorganism i, as derived earlier:

$$\begin{aligned}\frac{d\boldsymbol{r}_i}{dt} =& v(\psi)\hat{\boldsymbol{n}}_i + A(\psi)(\boldsymbol{\nabla}\psi\cdot\hat{\boldsymbol{n}}_i^{\perp})\hat{\boldsymbol{n}}_i^{\perp} + B(\psi)(\boldsymbol{\nabla}\psi\cdot\hat{\boldsymbol{n}}_i)\hat{\boldsymbol{n}}_i \\ &+ \sqrt{2D_{\parallel}}\eta_i^{\parallel}\hat{\boldsymbol{n}}_i + \sqrt{2D_{\perp}}\eta_i^{\perp}\hat{\boldsymbol{n}}_i^{\perp}\end{aligned} \tag{3.24a}$$

$$\frac{d\hat{\boldsymbol{n}}_i}{dt} = -\chi(\psi)\hat{\boldsymbol{n}}_i\times[\hat{\boldsymbol{n}}_i\times\boldsymbol{\nabla}\psi] + \sqrt{2D_r(\psi)}\eta_i^{\perp}\boldsymbol{n}_i^{\perp} \tag{3.24b}$$

$$\partial_t\psi(\boldsymbol{r}_i,t) = k\sum_i \frac{1}{2\pi\delta^2}\exp[-(\boldsymbol{r}-\boldsymbol{r_i})^2/2\delta^2] \tag{3.24c}$$

where $\boldsymbol{r}_i$ is the position of a microorganism i and $\hat{\boldsymbol{n}}_i = (\cos\varphi_i(t), \sin\varphi_i(t))^T$ is its orientation. As derived in section 3.3, the rotational noise is proportional to the orthogonal noise $\eta_i^{\perp}\hat{\boldsymbol{n}}_i^{\perp}$, which means that the same orthogonal fluctuation will translate and rotate the microorganism, increasing the correlation between orientation and trajectory [78]. This is an interesting result of the derivation and we will also keep this dependence in our simulations. We have here chosen a Gaussian shape for

the trail to account for intitial weak diffusion, and for consistency with other trail shape models employed in literature [62].

The pre-factors of the above equations are related and can be expressed in terms of $v(\psi)$ and $D_r(\psi)$ as:

$$
\begin{aligned}
D_{\parallel}(\psi) &= \left[\frac{4\gamma_{\mathrm{rot}}^2 c_2}{\ell^2\gamma_{\parallel}^2(1-c_2)}\right] D_r(\psi), \\
D_{\perp}(\psi) &= \left(\frac{2\gamma_{\mathrm{rot}}}{\gamma_{\perp}\ell}\right)^2 D_r(\psi), \\
\chi(\psi) &= \left[\frac{\gamma_{\parallel}\ell\ell_p(1-c_2)}{2\gamma_{\mathrm{rot}}c_1}\right] \partial_\psi v(\psi) + \alpha\partial_\psi D_r(\psi), \\
A(\psi) &= \left[\frac{\ell_p(1-c_2)\gamma_{\parallel}}{c_1\gamma_{\perp}}\right] \partial_\psi v(\psi) + \alpha\left(\frac{2\gamma_{\mathrm{rot}}}{\gamma_{\perp}\ell}\right)^2 \partial_\psi D_r(\psi), \\
B(\psi) &= \left[\frac{\ell_p c_2}{c_1}\right] \partial_\psi v(\psi) + \alpha\left[\frac{4\gamma_{\mathrm{rot}}^2 c_2}{\ell^2\gamma_{\parallel}^2(1-c_2)}\right] \partial_\psi D_r(\psi),
\end{aligned}
\tag{3.25}
$$

with ℓ as the length of the microorganism, ℓ_p as the pilus length and $\gamma_{\parallel}$, $\gamma_{\perp}$, γ_{rot} as the friction coefficients for the parallel, perpendicular and rotational motion. $c_1 = \langle\cos\vartheta_p\rangle$ and $c_2 = \langle\cos^2\vartheta_p\rangle$ are average values involving the pili orientation angles ϑ_p with respect to the microorganism orientation $\hat{\boldsymbol{n}}$, see fig. 3.4 [78].

In consistency with experiments [1, 78], we set the length of a P. Aeruginosa bacterium to approximately $\ell \approx 2\,\mu$m and the typical length of a pilus ℓ_p to the same value. The bacterium width was measured as $0.5\,\mu$m in experiments [1, 78] and since the Psl trail secreted from its body is effectively non-diffusive we can assume that the trail width 2δ will be of the same order of magnitude, $\delta = 0.25\,\mu$m [78]. Since P.

Aeruginosa bacteria are approximately rod-like, we can estimate that $\gamma/\gamma_{\text{rot}} \approx 5/\ell^2$ and that $\gamma_\perp/\gamma_\parallel \approx 1.2$ [81]. Hence we have $D_\parallel/D_\perp \approx 1.5\, c_2/(1-c_2)$, where all values have been rounded [78]. From experiments for the translational mean square displacement in absence of Psl we find a total diffusion $D_{\text{total0}} = 1.1 \times 10^{-2} \mu\text{m}^2\,\text{s}^{-1}$, which is composed of parallel and perpendicular diffusion, such that $D_{\text{total0}} = D_{\parallel 0} + D_{\perp 0} = D_{\perp 0}[1+c_2\gamma_\perp^2/(1-c_2)\gamma_\parallel^2]$ [78]. We can determine $D_{r0} \approx 3.6\times 10^{-3}\,\text{s}^{-1}$ and hence $D_{\perp 0} = 2.3 \times 10^{-3} \mu\text{m}^2\,\text{s}^{-1}$, determine from the rotational mean square displacement in fig. 3.16 (b). We get $c_2 = \langle \cos^2 \vartheta \rangle \approx 0.7$ [78]. In our simulations we approximate $c_1 = \langle \cos \vartheta \rangle \approx \sqrt{c_2} = 0.8$, where all values have been rounded [78].

In case of small Psl concentrations ψ, we can Taylor-expand $v \approx v_0 + v_1\psi$ and $D_r \approx D_{r0} - D_{r1}\psi$. The signs in the Taylor expansions account for the intuition that the bacterial velocity will to a first approximation increase with ψ due to better attachment and pili pulling. Furthermore, better attachment to the surface will decrease random behaviour and hence we expect $D_r(\psi)$ to decrease with increasing ψ. This behaviour is also consistent with the microscopic model, which relates these quantities to the attachment rate $\lambda(\psi)$, and the detachment rate $\mu(\psi)$, see section 3.3. If we assume that attachment and friction are increased with ψ and that detachment is decreased, we will get an increase in v and a decrease in $D_\perp$ with increasing ψ.

At the shortest timescale we have resolved, the translational mean squared displacement in absence of polysaccharides has no propulsive component, see figure 3.16 (a), and hence we set $v_0 \approx 0$. In addition, we note from figure 3.16 (b) that the rotational mean squared displacement only has a weak Psl dependence for the

$\Delta \mathrm{P}_{psl}/\mathrm{P}_{BAD}$-*psl* mutant and hence we can also set $D_{r1} \approx 0$ [78]. The Psl secretion rate k always appears in combination with v_1 and hence only the combination kv_1 is a parameter that has not been directly extracted from the experiment [78].

The parameters in the stochastic simulations were chosen such that they correspond to the experimental parameters. The unit of length was 1 pixel = 0.06536μm and the unit of time was 1 frame = 3s. For all our simulations, we regarded all the above parameters as characteristic constants of the bacteria. Furthermore, we set $v_1 = 1(\text{pixel})^3/\text{frame} = 9.3 \times 10^{-5} \mu\text{m}^3\,\text{s}^{-1}$ and only varied k between simulation runs, in consistency a situation where the Psl production is dependent on an external factor (like the arabinose concentration in the substrate for the PBAD-psl).

As a complication in an experimental setting, we also need to take into account that the number of P. Aeruginosa bacteria in general fluctuates due to surface attachment, detachment, growth and death processes in a nontrivial way. For better comparability of samples with different numbers of bacteria on the surface, we have followed Zhao et al. [1] and compared samples with a similar number of total bacterial visits, i.e. the sum of the number of bacteria in all frames $S_{\text{visits}} = \sum s_i$, where s_i is the number of bacteria on the surface in frame i [1, 78]. An approach like this ensures comparable conditions for exposure of the surface to bacterial motion and Psl secretion. For a more detailed motivation, see [1].

Figure 3.17 (a) shows the match between theoretical and experimental angle distributions for $\Delta\theta$ and figure 3.17 (b) for $\Delta\alpha$. As in the experiments, the distributions for

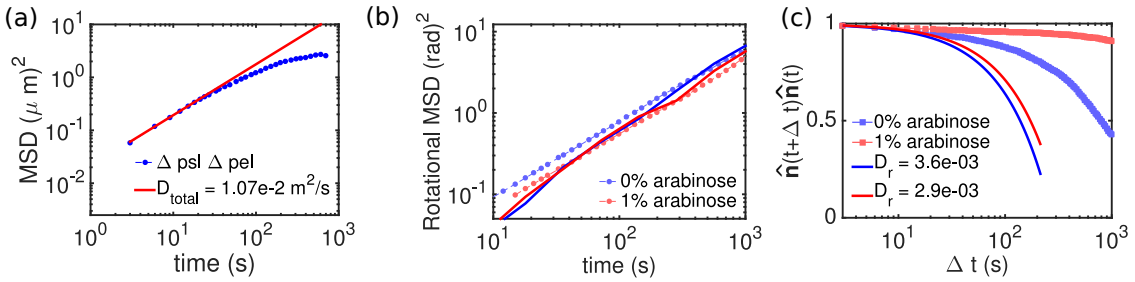

Figure 3.16: (a) Translational mean square displacement for the $\Delta psl\Delta pel$ mutant, which does not produce any exopolysaccharides. For short times the motion is purely diffusive, without a propulsive component v_0. The corresponding total diffusion constant was determined as $D_{\text{total}0} = D_{\parallel 0} + D_{\perp 0} \approx 1.1 \times 10^{-2}\mu\text{m}^2\,\text{s}^{-1}$. For longer times mobile bacteria will detach, such that only non-mobile bacteria contribute to the mean squared displacement, resulting in a flattening of the experimental MSD. (b) shows a comparison between theoretical (lines) and experimental (dots) rotational MSD for $\Delta\text{P}_{psl}/\text{P}_{BAD}$-$psl$ and 0% arabinose (blue, low Psl production, $k = 0.073\,\text{s}^{-1}$ in simulations), and 1% arabinose (red, high Psl production, $k = 0.18\,\text{s}^{-1}$ in simulations) [78]. (c) shows the orientational correlation function $\langle\hat{\boldsymbol{n}}(t+\Delta t)\hat{\boldsymbol{n}}(t)\rangle$ (dots), as well as best fits for extracting D_r in the short time approximation $\langle\hat{\boldsymbol{n}}(t+\Delta t)\hat{\boldsymbol{n}}(t)\rangle \approx 1 - \langle[\varphi(t+\Delta t) - \varphi(t)]^2\rangle/2$. This yields similar values for D_r as (b). Taken with permission from [78].

$\Delta\theta$ are much wider than for $\Delta\alpha$. And whereas the $\Delta\alpha$ distributions are not strongly influenced by Psl production, the distributions for $\Delta\theta$ narrow down with increasing Psl. Comparing simulations and experiments, we determined that the experimental data for a low Psl production rate ($\Delta P_{psl}/P_{BAD}$-*psl* with 0% arabinose in the environment) is best fitted by $k = 0.073, s^{-1}$, whereas for a high Psl production (1% arabinose in the environment) the best match was for $k = 0.18\, s^{-1}$. For intermediate values of arabinose in the environment, the corresponding theoretical Psl production rates k can be found in fig. 3.19(a) [78].

3.9 Comparison of Experiments and Theory for Microcolony Formation

We now want to simulate our model, which was calibrated with single bacteria experimental data, on a macroscopic scale in order to examine whether the experimental predictions on colony formation are reproduced. Using single-particle tracking algorithms Zhao at al. [1] could show that the pili-mediated motility of P. Aeruginosa is the driving factor in the biofilm formation at early stages. Type IV pili interaction with existing Psl trails effectively leads to a self-feedback (or "rich get richer") effect where surface regions with a lot of Psl attract more bacteria, thereby further increasing the Psl concentration there. As a result, P. Aeruginosa bacteria tend to accumulate in just a few locations, whereas a lot of regions remain unvisited or visited only a couple times by the bacteria [1, 78]. We have quantitatively compared the

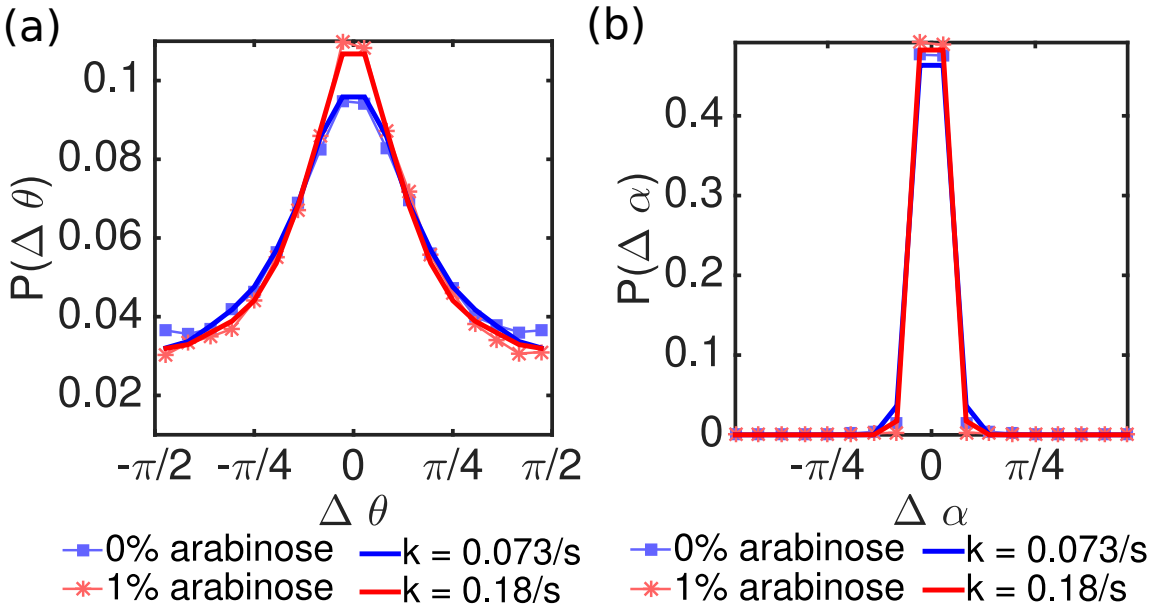

Figure 3.17: Experimental (dots) and theoretical (lines) angle distributions $\Delta\theta$ and $\Delta\alpha$, see schematics in fig. 3.3 (b). The error per angle measurement is $\pm 5°$ and about $400,000$ angle measurements were carried out at early stages before the formation of microcolonies. $\Delta\theta$ is the angle between the current body orientation and the trajectory of the bacterium, smoothed over 21 points using a Savitsky-Golay filter of third order. The trajectory points have been recorded at intervals of 3 s using a particle tracking algorithm. $\Delta\alpha$ is the difference in bacterial axis orientation between two timesteps of 3 s. (a) shows the fit between theoretical and experimental $\Delta\theta$ distributions for 0% arabinose (blue) and 1% arabinose, whereas (c) and (d) show the match of theoretical and experimental $\Delta\alpha$ distributions. For 0% arabinose the best match was $k = 0.073\,\mathrm{s}^{-1}$, see (a) and (c), whereas for 1% arabinose the best fit was achieved for $k = 0.18\,\mathrm{s}^{-1}$, see (b) and (d) [78]. For intermediate k values, see fig. 3.19 (a) and [78]. Taken with permission from [78].

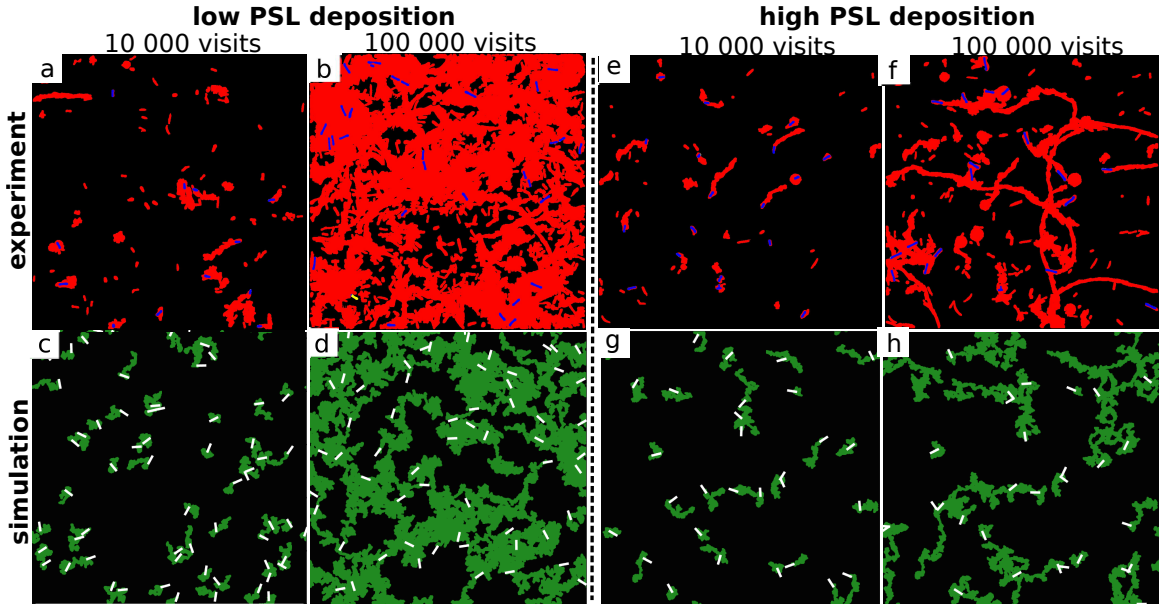

Figure 3.18: Snapshots of typical surface coverages and bacterial locations from experiments (red) and simulations (blue). (a)–(d) correspond to a P. Aeruginosa mutant which deposits very little Psl, whereas in (e)–(h) the Psl secretion is high. The experimental data was obtained using the P. Aeruginosa mutant $\Delta \mathrm{P}_{psl}/\mathrm{P}_{BAD}$-*psl*, which increases Psl production in the presence of arabinose in the environment. (a)–(b) show that the $\Delta \mathrm{P}_{psl}/\mathrm{P}_{BAD}$-*psl* mutant under 0% arabinose visits most of the surface sites after a total of $S_{\mathrm{visits}} = 100,000$ visits. (c)–(d) show a corresponding simulation result for low Psl production ($k = 0.073\,\mathrm{s}^{-1}$ corresponding to 0% arabinose for the mutant $\Delta \mathrm{P}_{psl}/\mathrm{P}_{BAD}$-*psl*). One can see in (d) that most of the surface has been covered after a long cumulative time. (e)–(f) show the experimental outcome for 1% arabinose, i.e. high Psl secretion. The visited area fraction is then much smaller and bacteria tend to aggregate mode. Simulations in (g)–(h) show a similar result for a high Psl production ($k = 0.18\,\mathrm{s}^{-1}$, corresponding to 1% arabinose for the mutant $\Delta \mathrm{P}_{psl}/\mathrm{P}_{BAD}$-*psl*). (h) shows that the surface visits and Psl deposition are concentrated over a small surface area and that bacteria accumulate in Psl-rich spots. Taken with permission from [78]

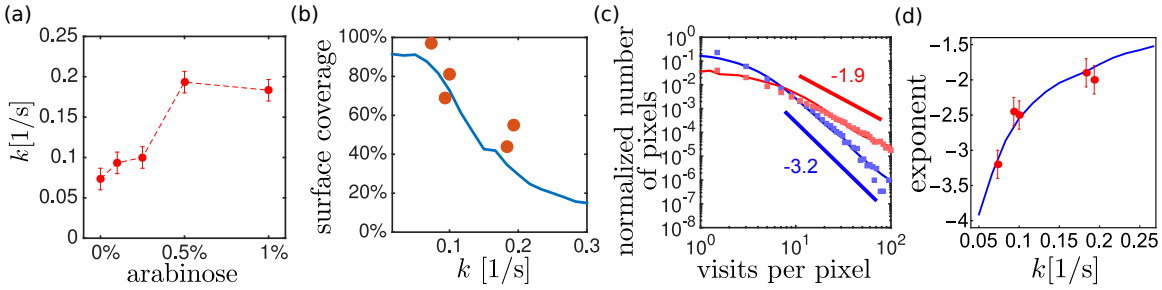

Figure 3.19: (a) Experimental arabinose concentrations $C_{\text{ara}} = (0\%, 0.1\%, 0.25\%, 0.5\%, 1\%)$ and the corresponding values for the Psl secretion $k = (0.073, 0.093, 0.1, 0.19, 0.18)\,\text{s}^{-1}$ determined from the single-bacteria angle distributions in figs. [see Figs. 3.17(a)–3.17(b)]. (b)–(d) Comparison between experiments (dots) and theory (lines) for the collective colony formation in $\Delta\text{P}_{psl}/\text{P}_{BAD}$-*psl*. The collective results were obtained without any additional fitting. (b) Percentage of the surface visited by 30 bacteria after the simulational equivalent of 13.8h ($S_{\text{visits}} = 500,000$), in dependence on the Psl production rate k. The red dots show experimental measurements for 0%, 0.1%, 0.25%, 0.5% and 1% arabinose [with the corresponding k values from (a)]. The experimental error was $\pm 10\%$ for 0%, 0.1% and 1% arabinose. For 0.25% and 0.5% the experimental sample size was too small to determine the error. (c) The self-feedback mechanism of high Psl concentrations attracting Psl-depositing bacteria leads to a power-law distribution in the number of visits per pixel, shown for 0% (blue dots) and 1% (red dots) arabinose. The corresponding distributions from simulations are shown as solid lines with the same colors. The power law exponent depends on the Psl rate k, becoming more hierarchical (slower decay) with increasing Psl production. [78]. [78]. (d) Comparison between experimental (red dots with error bars) and simulated (blue line) power-law exponents [78]. The estimated fitting errors are ± 0.1 for simulations and ± 0.2 for experiments. Taken with permission from [78].

experimental findings to simulations of collective behaviour and the results can be seen in figure 3.19. Figures 3.18 (a)–(h) show typical snapshots of visited sites from experiments and theory. For a small Psl production rate, figs. 3.18 (a)–(d), the Psl trail is weak and the bacterial behaviour is essentially diffusive for long times. As a result, in case of a low Psl production, most surface sites are visited in the long run as there is no or only a weak preference for certain sites (Psl coverage is low everywhere). This corresponds to a high long-time surface coverage for long times, see fig. 3.19 (b). Weak Psl interaction also means that the power-law distribution of visits and Psl coverage will decay very quickly, i.e. it will be more egalitarian with almost all surface sites having a similar number of bacterial visits. The power-law exponent is small in case of low Psl production, see figs. 3.19 (c) and (d).

In the case of a high Psl deposition, however, as can be seen from figures 3.18 (e)–(h), Psl-rich surface sites are preferentially visited by the bacteria. These bacteria deposit additional Psl at these sites, hereby attracting even more visits. The result is a "rich get richer" mechanism and an accumulation of bacteria at only a few sites, facilitating microcolony formation. In this case, bacteria only cover a small surface fraction even for long times, as seen from fig. 3.19 (b). The Psl distribution becomes more hierarchical, with few sites visited frequently and many sites only infrequently. Consistently with rich-get-richer behaviour, the resulting Psl distributions behave like power laws over a long range, with a slow decay, meaning that high Psl concentrations are likely to occur, see figs. 3.19 (c) and (d) [78].

As noted by Zhao et al. [1], the Pareto-type power-law distribution of visits

frequency per surface sites (and consequently of secreted Psl) is similar to wealth distributions in capitalist economies [1, 76, 78]. As experiments with the arabinose-dependent Psl producer $\Delta P_{psl}/P_{BAD}$-*psl* suggest, the power-law exponents increase from -3.1 to -1.8 with increasing Psl deposition [1, 78]. As can be seen from figs. 3.19 (c) and (d), the power law decay and exponents encountered in theory and experiments are in good quantitative agreement, suggesting that the theoretical model derived in this chapter is capable of explaining the main experimental results. [78].

3.10 Network Model for Collective Behaviour of P. Aeruginosa

In this chapter, we will try to get a better understanding of the "rich-get-richer" mechanism leading to colony formation by drawing an analogy with a preferential attachment network [75,76]. We base our calculations on the pili-mediated chemotaxis model derived above and in [78] and develop an analytical network theory which can be used to approximately predict the power-law exponents of the Psl distribution. A comparison of the calculated power-law exponents shows a relatively good agreement of the approximate network theory with experiments and simulations, as seen in fig. 3.20.

We take a mean-field approach to a growing bacterial colony, where all spatial sites can be visited by the bacteria at each time step τ with some probability, and

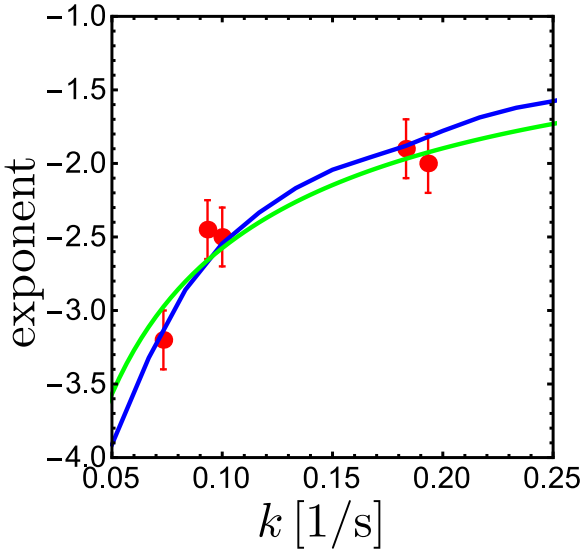

Figure 3.20: Power law exponents of the frequency distribution of the Psl concentration for a large total visit number ($S_{\text{visits}} = 500,000$), with experimental and simulational exponents from fig. 3.19. Comparison between experiments (red dots), simulations (blue line) and analytical theory (green line)

we take into account that sites with previous Psl deposition are more likely to be visited again. In this approximation we will ignore spatial correlations and assume that each bacterium is equally likely to visit a given surface site. This approximation is expected to become accurate in the case of a dense colony where every site is in the proximity of one or several bacteria.

To be precise, a new site (i.e. yet Psl-less site) is visited with a probability $p(t)$, whereas an existing site is visited with a probability $1 - p(t)$, where the conditional probability for picking a particular site out of the ones visited is proportional to the number of previous visits. This description is equivalent to the Yule-Simon network theory for preferential attachment scenarios [75], and we can analogously derive expressions for the distribution of Psl depositions and visits to particular sites [75]. Defining $f(i,t)$ as the number of sites with exactly i visits before time τ we can write

down the balance equations [75]

$$f(i,t+\tau) - f(i,t) = K(t)[(i-1)f(i-1,t) - if(i,t)] \tag{3.26a}$$

for $i \neq 1$ and

$$f(1,t+\tau) - f(1,t) = p(t) - K(t)f(1,t) \tag{3.26b}$$

for $i = 1$.

These equations take into account that the probability of visiting a new site is proportional to the number of visits that have already occurred at the site. By this assumption, the probability that a site that has been visited $i-1$ times will be visited again during the next time step will be proportional to $(i-1)f(i-1,t)$, with a proportionality constant $K(t)$ [75].

The total probability of picking any existing site at time t is $1-p(t)$ and therefore $K(t)\sum_i if(i,t) = K(t)t = 1-p(t)$. The probability distribution is assumed to "equilibrate" for large times and the "equilibrium" condition is that $f(i,t+\tau) \sim f(i,t)$. Due to normalisation this condition gives $f(i,t+\tau) = (1+p(t)/n_t)f(i,t)$, where $n_t = \int^t p(t')\mathrm{d}t'$ is the total number of visited sites [75]. Plugging this into eqs. (3.26) finally gives the recursion relation

$$f(i,t) = \frac{i-1}{i + \frac{p(t)t}{n_t}\frac{1}{1-p(t)}} \sim i^{-\left(1+\frac{p(t)t}{(n_t(1-p(t)))}\right)}, \tag{3.27}$$

see [75]. The approximation in [75] used the assumption that $p(t)$ varies only slowly for large t. In order to apply the Yule-Simon theory to our problem we need an expression for $p(t)$, i.e. of the probability at which new sites are visited. To obtain an expression we regard bacteria which secrete a trail of exopolysaccharides (Psl), to which pili are able to preferentially attach and pull the bacteria forward.

We rewrite eq. (3.17b) for the orientation vector $\hat{\boldsymbol{n}}_i$ in terms of the angle φ_i with the x-axis as

$$\begin{aligned} \partial_t \varphi_i &= \chi(\psi)(\cos(\varphi)\partial_y \psi - \sin(\varphi)\partial_x \psi) + \sqrt{2D_r}\eta \\ &\approx \chi \partial_y \psi + \sqrt{2D_r}\eta \quad \text{if } \varphi \approx 0 \end{aligned} \tag{3.28a}$$

$\varphi \approx 0$ locally is just a simplification that can always be achieved by rotating the coordinate axes. It can be approxinately rewritten as

$$\Delta\varphi \approx \chi(\psi)\partial_y \psi \Delta t + \sqrt{2D_r \Delta t} g(1) \tag{3.28b}$$

where $g(1)$ is a random number from a Gaussian distribution with mean 0 and variance 1. We will take $\Delta t = 2\delta/v$, i.e. as the time it takes to cross the Psl trail and we set for the velocity $v \approx v_1 \frac{k}{2\pi\delta^2} \exp\left(\frac{0}{2\delta^2}\right)$, i.e. the velocity at the peak value of the Gaussian trail in eq. (3.16).

To make progress in our approximate network theory we assume that the domi-

nance of the random noise component of eq. (3.28b) will always lead to the exploration of a new site, while the dominance of alignment to the Psl field will always lead to a further visit of a site with Psl on it. The condition for the exploration for a new site would therefore be that the random component proportional to $g(1)$ dominates the equation for $\Delta\varphi$. Setting $c(t) \sim \chi\partial_y\psi\sqrt{\Delta t}/\sqrt{2D_r}$ this gives

$$p(t) = P(g(1) > c) = 1 - \int_{-c}^{c} \frac{1}{\sqrt{2\pi}} e^{-s^2/2} ds \tag{3.28c}$$

Finally, $\partial_y\psi$ is approximated as proportional to the maximum descent of a Gaussian times the expected number of visits to a site over the observation period t, which under the influence of diffusion scales as $\ln(t/\Delta t)$ in two dimensions. In total, our estimate for a typical Psl gradient is therefore $\partial_y\psi \sim k\frac{1}{2\pi}\exp(-1/2)\ln t/\Delta t$. With this estimate we have

$$c(t) = \epsilon\chi k\frac{1}{2\pi}\exp(-1/2)\ln(t/\Delta t)\sqrt{\Delta t}/\sqrt{2D_r} \tag{3.28d}$$

where ϵ is a proportionality constant of order one, accounting for the approximate nature of the rough calculation. From the calculations in chapter 3.8 we can determine $\chi \approx 8.4 \times 10^{-4}\mu\mathrm{m}^3/\mathrm{s}$. With all the other constants determined from experiments (see chapter 3.8, we are left with just the proportionality constant ϵ, which is a priori unknown since we have not carried out a full calculation and since we have neglected spatial correlations. The best agreement between exponents was achieved for a proportionality constant $\epsilon = 0.32$. Plugging this into eq. (3.27) and evaluating

the visit distribution numerically gives the blue line in fig. 3.20 and it is in close agreement with our results from simulations and experiments.

This simple analytical description relies on approximations but it is still in surprisingly good agreement with experimental and simulatonal data from chapter 3.8, which could suggest that the power-law exponents observed in experiments are more conditioned by the underlying principle of preferential attachment than by the exact details of the interaction between the bacterium and the trail.

3.11 Discussion

In summary, based on microscopic interactions observed in experiments we have derived a model for the chemotactic motion of a single bacterium under the influence of an effectively non-diffusing self-deposited trail. As an important consequence of pili-mediated motion we found orientational alignment with the gradient, which is crucial for explaining experimental measurements for rotational diffusion.

In the context of autochemotaxis, orientational alignment can lead to enhanced rotational diffusion and shows a sharp transition to trapping behaviour. In the case that the microorganisms interact with an existing trail, however, the alignment term can lead to oscillatory trail-following and thus stabilise microorganism trajectories which would otherwise be distupted by orientational noise. If a microorganism is approximately perpendicular to an existing exopolysaccharide trail, it can escape the

trail.

Using single-bacteria experiments we have extracted the microscopic parameters and shown that the angle distribuitions can be quantitatively reproduced. All of the model parameters have been determined from experimental data. Following that, we have simulated the same model without additional fits for multiple bacteria and shown that microcolony formation due to pili-mediated motion is in quantitative agreement with experiments for P. Aeruginosa and that the microscopically derived model can reproduce the hallmarks of the long-time collective microcolony formation, like preferential surface attachment to Psl-rich sites leading to a rich-get-richer mechanism, as characterized by power-law distributions. The corresponding power-law exponents have been predicted quantitatively.

To gain a better understanding of the power-law behaviour characterized by Pareto-type Psl distributions we have devised a simple network theory calculation, which analytically describes how the trail-following mechanism of P. Aeruginosa and preferential visits to Psl rich surface areas results in power laws. Despite the approximate nature of the calculations we were able to reproduce the power law exponents from experiments and simulations. For future research it would be interesting to investigate whether universal network theory can provide additional insights into the structures of large bacterial colonies that are otherwise difficult to study analytically.

Remarkably, the underlying trail-alignment model is purely mechanistic and relies on surface-dependent pulling and attachment/detachment rather than a more com-

plicated chemical sensing mechanism found in other bacteria. Therefore we were able to directly relate it to physical observables, both for the short-time single-bacteria case and for the long-time collective case. Our results show that trail following and gradient-induced trail alignment constitute an important yet little-studied mechanism for microcolony formation, which is potentially employed by a variety of surface-active bacteria like Myxococcus Xanthus and Neisseria Gonorrhoae.

Chapter 4

Summary and Outlook

The defining idea of this thesis was to develop a theoretical framework to better understand chemotaxis, and to show that theoretical Physics can give us insights into bacterial and cellular colony formation. As an important feature our theoretical models were coarse-grained and were derived from universal principles like gradient following and surface attachment. As such, we believe that our approaches could provide insights into a wide range of bacterial and cellular systems, even if the exact microscopic interactions are distinct from each other.

The first part of this thesis was devoted to a colony of cells (or bacteria), which secrete fast-diffusing chemicals. As an addition, we also took cell division into account and found that chemotactic and cell division effects are of a similar order of relevance. The interplay between these two effects determines the long-time and large-scale behaviour of the colony. We used the principle of scale invariance to study

phase transitions and collective effects, applying Dynamical Renormalization Group techniques known from Solid-State Physics and Soft Matter. As an important result, we found a phase where chemotaxis and growth are controlled and were able to calculate critical exponents for different dimensions. However, there is also a phase where chemotaxis becomes irrelevant compared to growth and where growth and death processes dominate. A short analysis of relevant orders of magnitude suggests that our system could be a simple model to explain the sharp transition between controlled interaction and uncontrolled birth/death processes in cancer cells. For future research, it would be interesting to test our predictions in controlled experiments, for example with stem cells or cancer cells. In addition, a throrough theoretical examination of additional features, like for example a chemical-dependent division rate, a large but finite chemical diffusion rate, as well as sticky attachment at later stages of colony formation, could provide a lot interesting insights.

In the second part of our thesis we focused on interactions between microorganisms in the opposite limit: the limit of non-diffusive secreted chemicals. Bacteria like Pseudomonas Aeruginosa leave a trail of sticky polysaccharides on a surface, which can be considered effectively non-diffusive and which acts as a memory of previous locations. Following experimental guidance, we have derived differential equations for the microorganism motion, solely assuming general mechanical interactions between trail and the microorganism motion apparatus (here: Type IV pili). We were interested in the underlying principles of trail-following and the effects of autochemotaxis due to self-secreted cells. We found that autochemotaxis leads to an enhanced rotational

diffusion for long time scales and reduces translational diffusion. Above a threshold for the coupling between trail and microorganism, the microorganisms transition into an effectively trapped state. In the case that the microorganisms interact with an existing trail, we have shown that oscillatory behaviour between trail boundaries stabilises trail-following and provides a mechanism for moving along high concentrations of polysaccharides. However, if fluctuations reorient the microorganism orthogonally to an existing trail, escape events are very likely. The combination between movement along polysaccharide-rich areas and escapes provides an effective mechanism for spatial exploration and discovery of high polysaccharide concentrations. To verify our models, we have quantitatively compared observables from theory and experiments for P. Aeruginosa. In the case of single-bacteria movement, we have confirmed that the anglular deviations between trajectory and orientation increase for increasing polysaccharide deposition, whereas differences in orientation angles over time are roughly the same. We were able to derive all theoretical constants from single-bacteria experiments. On the larger scale of microcolony formation, we have confirmed that polysaccharide deposition leads to a self-feedback mechanism where polysaccharide-rich surface sites get "richer" by getting visited more frequently, in consistency with experiments. The corresponding polysaccharide distributions show power law behaviour and the exponents from our theoretical prediction are in agreement with experimental data. To understand the power-law behaviour we have devised a simple network calculation that models preferential attachment to polysaccharide-rich sites. In this thesis we tried to keep our research as general as possible, but for the experimental part we clearly had Pseudomonas Aeruginosa in mind. As shown in [77],

however, from a mathematical perspective there is no need to restrict ourselves to one particular geometry, as long as we can assume physical interactions between a trail and Type-IV pili and an anisotropic pili distribution along the microorganism body. Our model could provide interesting insights for other example systems, Myxococcus Xanthus and Neisseria Gonorrhoae [73] and we expect very similar behaviour, even though additional effects (like for example that M. Xanthus can reverse direction by disassemblin pili at one pole and assembling them at another) would need to be taken into account.

Appendix A

Growth-Coagulation Model for Logistic Growth

In chapter 2 we derived the equations for a chemotactic system under the influence of growth, for example logistic growth. Logistic growth models have been derived for many different microscopic systems [82]. Here we will provide a simple derivation of a noisy logistic growth model, to provide one possible expression for the noise strength M. The same derivation can also be found in the supplement of [49]. The process we will focus on is called the growth-coagulation process [49, 82] and is defined as

$$A \to A + A \quad \text{with rate } \gamma \tag{A.1a}$$

and

$$A + A \to A \quad \text{with rate } \chi, \tag{A.1b}$$

(see also [49, 82])

The rate equation for the probability $P(n,t)$ of finding n particles at time t is then

$$\partial_t P(n,t) = \gamma(n-1)P(n-1,t) + \chi(n+1)\frac{n}{2V}P(n+1,t) - \gamma n P(n,t) + \chi n \frac{n-1}{2V}P(n,t) \tag{A.2a}$$

By Taylor-expanding this equation up to the second order in n, we get the Fokker-Planck equation

$$\partial_t P(n,t) = -\partial_n[\gamma n P(n,t) - \chi n \frac{n-1}{2V}]P(n,t) + \frac{1}{2}\partial_n^2[\gamma n P(n,t) + \chi n \frac{n-1}{2V}]P(n,t). \tag{A.2b}$$

Hence, if we do not take into account chemotactic contributions, the Langevin equation for the density $C = n/V$ can be written as

$$\frac{dC}{dt} = \lambda C(1 - \frac{C}{C_0}) + \frac{1}{\sqrt{V}}\sqrt{(\gamma - \chi/(2V))C + \chi/2C^2}\eta \tag{A.2c}$$

with $\lambda = (\gamma - \chi/2V)$ and $C_0 = 2\gamma/\chi + 1/V$. When expanding around C_0, as we did in eq. (2.4), we get for the particle fluctuation noise $\sqrt{2M} \sim \frac{1}{\sqrt{V}}\sqrt{C_0}$ [49].

Bibliography

[1] K. Zhao, B. S. Tseng, B. Beckerman, F. Jin, M. L. Gibiansky, J. J. Harrison, E. Luijten, M. R. Parsek, and G. C. L. Wong. Psl trails guide exploration and microcolony formation in pseudomonas aeruginosa biofilms. *Nature*, 497(7449):388–391, 2013.

[2] M. L Gibiansky, W. Hu, K. A Dahmen, W. Shi, and G. C. L. Wong. Earthquake-like dynamics in myxococcus xanthus social motility. *Proc. Natl. Acad. Sci.*, 110(6):2330–2335, 2013.

[3] M. P. Brenner, L. S. Levitov, and E. O. Budrene. Physical mechanisms for chemotactic pattern formation by bacteria. *Biophys. J.*, 74(4):1677 – 1693, 1998.

[4] F. Ramos, C. López, and M. A. Munoz E. Hernández-García. Crystallization and melting of bacteria colonies and brownian bugs. *Phys. Rev. E*, 77, 2008.

[5] E. O. Budrene and H. C. Berg. Complex patterns formed by motile cells of escherichia coli. *Nature*, 349(6310):630, 1991.

[6] D.E. Woodward, R. Tyson, M.R. Myerscough, J.D. Murray, E.O. Budrene, and H.C. Berg. Spatio-temporal patterns generated by salmonella typhimurium. *Biophys. J.*, 68(5):2181 – 2189, 1995.

[7] M. E. Cates, D. Marenduzzo, I. Pagonabarraga, and J. Tailleur. Arrested phase separation in reproducing bacteria creates a generic route to pattern formation. *Proc. Natl. Acad. Sci.*, 107(26):11715–11720, 2010.

[8] M. E. Cates. Diffusive transport without detailed balance in motile bacteria: does microbiology need statistical physics? *Rep. Prog. Phys.*, 75(4):042601, 2012.

[9] M. E. Cates and J. Tailleur. When are active brownian particles and run-and-tumble particles equivalent? consequences for motility-induced phase separation. *Europhys. Lett.*, 101(2):20010, 2013.

[10] J. Tailleur and M. E. Cates. Statistical mechanics of interacting run-and-tumble bacteria. *Phys. Rev. Lett.*, 100(21), 2008.

[11] J. Tailleur and M. E. Cates. Sedimentation, trapping, and rectification of dilute bacteria. *Europhys. Lett.*, 86(6):60002, 2009.

[12] T. B. Liverpool and M. C. Marchetti. Instabilities of isotropic solutions of active polar filaments. *Phys. Rev. Lett.*, 90:138102, Apr 2003.

[13] T. B. Liverpool and M. C. Marchetti. Rheology of active filament solutions. *Phys. Rev. Lett.*, 97:268101, Dec 2006.

[14] A. Baskaran and M. C. Marchetti. Enhanced diffusion and ordering of self-propelled rods. *Phys. Rev. Lett.*, 101:268101, Dec 2008.

[15] A. Baskaran and M. C. Marchetti. Hydrodynamics of self-propelled hard rods. *Phys. Rev. E*, 77:011920, Jan 2008.

[16] R. Golestanian. Collective behavior of thermally active colloids. *Phys. Rev. Lett.*, 108(3), 2012.

[17] A. Baskaran and M. C. Marchetti. Statistical mechanics and hydrodynamics of bacterial suspensions. *Proc. Natl. Acad. Sci.*, 106(37):15567–15572, 2009.

[18] J. Toner and Y. Tu. Flocks, herds and schools: A quantitative theory of flocking. *Phys. Rev. E*, 58(4), 1998.

[19] T. Vicsek. Universal patterns of collective motion from minimal models of flocking. In *Self-Adaptive and Self-Organizing Systems, 2008. SASO '08. Second IEEE International Conference on*, pages 3 –11, oct. 2008.

[20] T. B. Liverpool and M. C. Marchetti. Bridging the microscopic and the hydrodynamic in active filament solutions. *Europhys. Lett.*, 69(5):846, 2005.

[21] T. Vicsek and A. Zafeiris. Collective motion. *Phys. Rep.*, 2012.

[22] T. Vicsek, A. Czirók, E. Ben-Jacob, I. Cohen, and O. Shochet. Novel type of phase transition in a system of self-driven particles. *Phys. Rev. Lett.*, 75:1226–1229, Aug 1995.

[23] V. Schaller, C. Weber, C. Semmrich, E. Frey, and A. R. Bausch. Polar patterns of driven filaments. *Nature*, 467(7311):73–77, September 2010.

[24] S. Ramaswamy. The mechanics and statistics of active matter. *Annu. Rev. Cond. Mat. Phys.*, 1(1):323–345, 2010.

[25] H. C. Berg and D. A. Brown. Chemotaxis in escherichia coli analysed by three-dimensional tracking. *Nature*, 239(5374):500–504, 1972.

[26] D. Bray, M. D. Levin, and C. J. Morton-Firth. Receptor clustering as a cellular mechanism to control sensitivity. *Nature*, 393(6680):85–88, 1998.

[27] P. Cluzel, M. Surette, and S. Leibler. An ultrasensitive bacterial motor revealed by monitoring signaling proteins in single cells. *Science*, 287(5458):1652–1655, 2000.

[28] T. L. Min, P. J. Mears, I. Golding, and Y. R. Chemla. Chemotactic adaptation kinetics of individual escherichia coli cells. *Proc. Natl. Acad. Sci.*, 109(25):9869–9874, 2012.

[29] V. Sourjik and H. C. Berg. Functional interactions between receptors in bacterial chemotaxis. *Nature*, 428(6981):437–441, 2004.

[30] E. F. Keller and L. A. Segel. Model for chemotaxis. *J. Theor. Biol.*, 30(2):225–234, 1971.

[31] J. Swift and P. C. Hohenberg. Hydrodynamic fluctuations at the convective instability. *Phys. Rev. A*, 15:319–328, Jan 1977.

[32] F. Ginelli and H. Chaté. Relevance of metric-free interactions in flocking phenomena. *Phys. Rev. Lett.*, 105:168103, Oct 2010.

[33] E. Ben-Jacob, I. Cohen, and H. Levine. Cooperative self-organization of microorganisms. *Adv. Phys.*, 49(4):395–554, 2000.

[34] J. Toner. Birth, death, and flight: A theory of malthusian flocks. *Phys. Rev. Lett.*, 108(8):088102, 2012.

[35] M. Dworkin and D. Kaiser. Cell interactions in myxobacterial growth and development. *Science*, 230(4721):18–24, 1985.

[36] D. Forster, D. Nelson, and M. J. Stephen. Large-distance and long-time properties of a randomly stirred fluid. *Phys. Rev. A*, 16, 1977.

[37] M. J. Tindall, S. L. Porter, P. K. Maini, G. Gaglia, and J. P. Armitage. Overview of mathematical approaches used to model bacterial chemotaxis i: the single cell. *Bull. Math. Biol.*, 70(6):1525–1569, 2008.

[38] M. J. Tindall, P. K. Maini, S. L. Porter, and J. P. Armitage. Overview of mathematical approaches used to model bacterial chemotaxis ii: bacterial populations. *Bull. Math. Biol.*, 70(6):1570–1607, 2008.

[39] M. Vert, K.-H. Hellwich, M. Hess, P. Hodge, P. Kubisa, M. Rinaudo, F. Schué, et al. Terminology for biorelated polymers and applications (iupac recommendations 2012). *Pure Appl. Chem.*, 84(2):377–410, 2012.

[40] M. E. Davey and G. A. O'Toole. Microbial biofilms: from ecology to molecular genetics. *Microbiol. Mol. Biol. Rev.*, 64(4):847–867, 2000.

[41] E. Medina, T. Hwa, M. Kardar, and Y.-C. Zhang. Burgers equation with correlated noise: Renormalization-group analysis and applications to directed polymers and interface growth. *Phys. Rev. A*, 39, 1989.

[42] K. G. Wilson. The renormalization group: Critical phenomena and the kondo problem. *Rev. Mod. Phys.*, 47(4):773, 1975.

[43] D. Hanahan and R. A. Weinberg. Hallmarks of cancer: the next generation. *Cell*, 144(5):646–674, 2011.

[44] S. J. Singer and A. Kupfer. The directed migration of eukaryotic cells. *Annu. Rev. Cell Biol.*, 2(1):337–365, 1986.

[45] M. A. Herrero and J. J. L. Velázquez. Chemotactic collapse for the keller-segel model. *J. Math. Biol.*, 35(2):177–194, 1996.

[46] P.-H. Chavanis and C. Sire. Anomalous diffusion and collapse of self-gravitating langevin particles in d dimensions. *Phys. Rev. E*, 69(1):016116, 2004.

[47] P.-H. Chavanis. A stochastic keller–segel model of chemotaxis. *Commun. Nonlinear Sci. Numer. Simul.*, 15(1):60–70, 2010.

[48] J. Toner and Y. Tu. Long-range order in a two-dimensional dynamical xy model: how birds fly together. *Phys. Rev. Lett.*, 75(23):4326, 1995.

[49] A. Gelimson and R. Golestanian. Collective dynamics of dividing chemotactic cells. *Phys. Rev. Lett.*, 114(2):028101, 2015.

[50] H. Park, W. Pontius, C. C. Guet, J. F. Marko, T. Emonet, and P. Cluzel. Interdependence of behavioural variability and response to small stimuli in bacteria. *Nature*, 468(7325):819–823, 2010.

[51] P.-H. Chavanis, M. Ribot, C. Rosier, and C. Sire. On the analogy between self-gravitating brownian particles and bacterial populations. *Banach Center Publications*, 1(66):103–126, 2004.

[52] F. A. Chalub, P. A. Markowich, B. Perthame, and C. Schmeiser. Kinetic models for chemotaxis and their drift-diffusion limits. In *Nonlin. Diff. Eq. Mod.*, pages 123–141. Springer, 2004.

[53] D. S. Dean. Langevin equation for the density of a system of interacting langevin processes. *J. Phys. A*, 29(24):L613, 1996.

[54] M. A Nowak. *Evolutionary dynamics*. Harvard University Press, 2006.

[55] D. A. Kessler and H. Levine. Fluctuation-induced diffusive instabilities. *Nature*, 394(6693):556–558, 1998.

[56] J. G. Conlon and C. R. Doering. On travelling waves for the stochastic fisher–kolmogorov–petrovsky–piscunov equation. *J. Stat. Phys.*, 120(3-4):421–477, 2005.

[57] O. Hallatschek and K. S. Korolev. Fisher waves in the strong noise limit. *Phys. Rev. Lett.*, 103(10):108103, 2009.

[58] H. H Iacobson and D. J Amit. First order transitions induced by fluctuations in general φ 4-theories. *Ann. Phys.*, 133(1):57–78, 1981.

[59] J. Cardy. Effect of random impurities on fluctuation-driven first-order transitions. *J. Phys. A*, 29(9):1897, 1996.

[60] I. A. Lubashevsky, A. Heuer, R. Friedrich, and R. Usmanov. Continuous markovian model for lévy random walks with superdiffusive and superballistic regimes. *Europhys. J. B*, 78(2):207–216, 2010.

[61] A. W. Pearlman. Breast cancer—influence of growth rate on prognosis and treatment evaluation. a study based on mastectomy scar recurrences. *Cancer*, 38(4):1826–1833, 1976.

[62] I. D. Couzin and N. R. Franks. Self-organized lane formation and optimized traffic flow in army ants. *Proc. R. Soc. Lond. B Bio.*, 270(1511):139–146, 2003.

[63] I. D. Couzin. Collective cognition in animal groups. *Trends Cogn. Sci.*, 13(1):36–43, 2009.

[64] L. Ma, K. D. Jackson, R. M. Landry, M. R. Parsek, and D. J. Wozniak. Analysis of pseudomonas aeruginosa conditional psl variants reveals roles for the psl polysaccharide in adhesion and maintaining biofilm structure postattachment. *J. Bacteriol.*, 188(23):8213–8221, 2006.

[65] S. B. Carter. Haptotaxis and the mechanism of cell motility. *Nature*, 213:256–260, 1967.

[66] S. Aznavoorian, M. L. Stracke, H. Krutzsch, E. Schiffmann, and L. A. Liotta. Signal transduction for chemotaxis and haptotaxis by matrix molecules in tumor cells. *J. Cell Bio.*, 110(4):1427–1438, 1990.

[67] R. B. Dickinson and R. T. Tranquillo. A stochastic model for adhesion-mediated cell random motility and haptotaxis. *J. Math. Biol.*, 31(6):563–600, 1993.

[68] L. Ma, H. Lu, A. Sprinkle, M. R. Parsek, and D. J. Wozniak. Pseudomonas aeruginosa psl is a galactose-and mannose-rich exopolysaccharide. *J. Bacteriol.*, 189(22):8353–8356, 2007.

[69] M. S. Byrd, I. Sadovskaya, E. Vinogradov, H. Lu, A. B. Sprinkle, S. H. Richardson, L. Ma, B. Ralston, M. R. Parsek, E. M. Anderson, et al. Genetic and biochemical analyses of the pseudomonas aeruginosa psl exopolysaccharide reveal overlapping roles for polysaccharide synthesis enzymes in psl and lps production. *Mol. Microbiol.*, 73(4):622–638, 2009.

[70] G. A. O'Toole and R. Kolter. Flagellar and twitching motility are necessary for pseudomonas aeruginosa biofilm development. *Mol. Microbiol.*, 30(2):295–304, 1998.

[71] J. M. Skerker and H. C. Berg. Direct observation of extension and retraction of type iv pili. *Proc. Natl. Acad. Sci.*, 98(12):6901–6904, 2001.

[72] F. Jin, J. C. Conrad, M. L Gibiansky, and G. C. L. Wong. Bacteria use type-iv pili to slingshot on surfaces. *Proc. Natl. Acad. Sci.*, 108(31):12617–12622, 2011.

[73] B. Maier and G. C. L. Wong. How bacteria use type iv pili machinery on surfaces. *Trends Microbiol.*, 23(12):775–788, 2015.

[74] M. L. Gibiansky, J. C. Conrad, F. Jin, V. D. Gordon, D. A. Motto, M. A. Mathewson, W. G. Stopka, D. C. Zelasko, J. D. Shrout, and G. C. L. Wong. Bacteria use type iv pili to walk upright and detach from surfaces. *Science*, 330(6001):197–197, 2010.

[75] H. A Simon. On a class of skew distribution functions. *Biometrika*, 42(3/4):425–440, 1955.

[76] M. E. J. Newman. Power laws, pareto distributions and zipf's law. *Contemp. Phys.*, 46(5):323–351, 2005.

[77] W. T. Kranz, A. Gelimson, K. Zhao, G. C. L. Wong, and R. Golestanian. Effective dynamics of microorganisms that interact with their own trail. *Phys. Rev. Lett.*, 117(038101), 2016.

[78] A. Gelimson, K. Zhao, C. K. Lee, W. T. Kranz, G. C. L. Wong, and R. Golestanian. Multicellular self-organization of p. aeruginosa due to interactions with secreted trails. *Phys. Rev. Lett.*, 117(17):178102, 2016.

[79] N. G. Van Kampen. Itô versus stratonovich. *J. Stat. Phys.*, 24(1):175–187, 1981.

[80] J. Taktikos, V. Zaburdaev, and H. Stark. Modeling a self-propelled autochemotactic walker. *Phys. Rev. E*, 84(4):041924, 2011.

[81] M. M. Tirado, C. Lopez Martinez, and J. Garcia de la Torre. Comparison of theories for the translational and rotational diffusion coefficients of rod-like macromolecules. application to short dna fragments. *J. Chem. Phys.*, 81(4):2047–2052, 1984.

[82] C. R. Doering, C. Mueller, and P. Smereka. Interacting particles, the stochastic fisher–kolmogorov–petrovsky–piscounov equation, and duality. *Physica A*, 325(1):243–259, 2003.

Appendix B

List of Figures

List of Figures

3.10 Oscillation amplitudes and periods for following an existing horizontal trail, see fig. 3.9, for different trail shapes and EPS coupling strengths, averaged over 100 runs of 100τ each. Only cases where the microorganisms were following the trail were counted, whereas trail escapes were discarded. The initial orientation is $\varphi_0 = \pi/6$ and $D_r = 0.01\tau$. (a-b) show the oscillation periods and amplitudes for a microorganism that follows the horizontal Gaussian trail but does not secrete EPS on its own. As expected from the deterministic theory, the amplitude and oscillation period decays with increasing coupling χ. (c-d) shows the same setup, but here the microorganisms are able to secrete their own EPS. One can see in (c) that the oscillation period is not greatly influenced by the self-secreted trail, presumably because the microorganism is always located at the center of its own trail, where $\nabla\psi_{\text{self}} \approx 0$ over the radius $\sim \delta = 1$.The Gaussian trail seems to introduce a regime where the oscillation amplitude is only weakly dependent on χ. (e-f) show the oscillation period and amplitude for an existing triangular trail and no own trail secretion. As predicted by the deterministic theory, both trail period and amplitude decay with increasing EPS coupling Ξ. The red dotted lines show the estimated values for (e) the period $\Delta x \sim 2\frac{v_0}{\Xi}|\varphi_0|$ and (f) the amplitude $\Delta y \sim \left|\ln\left(\tan(\varphi_0/2 + \pi/4)\right)\right|$. (g-h) a self-deposited triangular trail reduces both the oscillation periods and amplitudes by an order of 10. The reason is that the triangular trail shape introduces a gradient jump at the location of the microorganism. In (a-d), Gaussian trail, we have $\chi = 1.5\delta^3/\tau$ and in (e-h), triangular trail, we have $\chi = 0.5\delta^3/\tau$ (or $\Xi = 0.5/\tau$, since $\partial_y\psi = 1/\delta^3$). These two values were chosen such that the average effective interaction with the trail is approximately the same for a triangular and a gaussian trail. 70

3.11 Oscillation amplitudes and periods for following an existing horizontal trail, see fig. 3.9, for different trail shapes and different values for the rotational diffusion D_r, averaged over 100 runs of 100τ each. The initial orientation is $\varphi_0 = \pi/6$ and D_r is varied between $0.01/\tau$ and $0.3/\tau$. (a)–(b) show the oscillation periods and amplitudes for a microorganism that follows the horizontal Gaussian trail but does not secrete EPS on its own. Rotational diffusion disrupts oscillations and hence amplitudes and periods increase with increasing diffusion. Eventually both amplitudes and periods saturate. (c)–(d) shows the same setup, but here the microorganisms are able to secrete their own EPS. One can see that the overall trend is the same, an increase in amplitude and period with increasing D_r, and eventually a saturation for large D_r. However, the increase of amplitudes and periods with increasing D_r is smaller since the additional self-deposited EPS trail can partly counteract the de-stabilizing effect of rotational diffusion on oscillations. (e)–(f) show the oscillation period and amplitude for an existing triangular trail and no own trail secretion. Also here both amplitude and period increase with D_r and eventually saturate, highlighting that rotational diffusion slightly de-correlates oscillations. (g-h) show that the same trend is preserved for trail-depositing microorganisms. In (a)–(d), Gaussian trail, we have $\chi = 1.5\delta^3/\tau$ and in (e)–(h), triangular trail, we have $\chi = 0.5\delta^3/\tau$. These two values were chosen such that the average effective interaction with the trail is approximately the same for a triangular and a gaussian trail. 73

3.16 (a) Translational mean square displacement for the $\Delta psl\Delta pel$ mutant, which does not produce any exopolysaccharides. For short times the motion is purely diffusive, without a propulsive component v_0. The corresponding total diffusion constant was determined as $D_{\text{total0}} = D_{\parallel 0} + D_{\perp 0} \approx 1.1 \times 10^{-2} \mu\text{m}^2\,\text{s}^{-1}$. For longer times mobile bacteria will detach, such that only non-mobile bacteria contribute to the mean squared displacement, resulting in a flattening of the experimental MSD. (b) shows a comparison between theoretical (lines) and experimental (dots) rotational MSD for $\Delta\text{P}_{psl}/\text{P}_{BAD}$-*psl* and 0% arabinose (blue, low Psl production, $k = 0.073\,\text{s}^{-1}$ in simulations), and 1% arabinose (red, high Psl production, $k = 0.18\,\text{s}^{-1}$ in simulations) [78]. (c) shows the orientational correlation function $\langle \hat{\boldsymbol{n}}(t + \Delta t)\hat{\boldsymbol{n}}(t)\rangle$ (dots), as well as best fits for extracting D_r in the short time approximation $\langle \hat{\boldsymbol{n}}(t + \Delta t)\hat{\boldsymbol{n}}(t)\rangle \approx 1 - \langle[\varphi(t + \Delta t) - \varphi(t)]^2\rangle/2$. This yields similar values for D_r as (b). Taken with permission from [78]. 84

3.17 Experimental (dots) and theoretical (lines) angle distributions $\Delta\theta$ and $\Delta\alpha$, see schematics in fig. 3.3 (b). The error per angle measurement is $\pm 5^\circ$ and about $400,000$ angle measurements were carried out at early stages before the formation of microcolonies. $\Delta\theta$ is the angle between the current body orientation and the trajectory of the bacterium, smoothed over 21 points using a Savitsky-Golay filter of third order. The trajectory points have been recorded at intervals of 3 s using a particle tracking algorithm. $\Delta\alpha$ is the difference in bacterial axis orientation between two timesteps of 3 s. (a) shows the fit between theoretical and experimental $\Delta\theta$ distributions for 0% arabinose (blue) and 1% arabinose, whereas (c) and (d) show the match of theoretical and experimental $\Delta\alpha$ distributions. For 0% arabinose the best match was $k = 0.073\,\text{s}^{-1}$, see (a) and (c), whereas for 1% arabinose the best fit was achieved for $k = 0.18\,\text{s}^{-1}$, see (b) and (d) [78]. For intermediate k values, see fig. 3.19 (a) and [78]. Taken with permission from [78]. 86

3.18 Snapshots of typical surface coverages and bacterial locations from experiments (red) and simulations (blue). (a)–(d) correspond to a P. Aeruginosa mutant which deposits very little Psl, whereas in (e)–(h) the Psl secretion is high. The experimental data was obtained using the P. Aeruginosa mutant $\Delta \mathrm{P}_{psl}/\mathrm{P}_{BAD}$-*psl*, which increases Psl production in the presence of arabinose in the environment. (a)–(b) show that the $\Delta \mathrm{P}_{psl}/\mathrm{P}_{BAD}$-*psl* mutant under 0% arabinose visits most of the surface sites after a total of $S_{\mathrm{visits}} = 100,000$ visits. (c)–(d) show a corresponding simulation result for low Psl production ($k = 0.073\,\mathrm{s}^{-1}$ corresponding to 0% arabinose for the mutant $\Delta \mathrm{P}_{psl}/\mathrm{P}_{BAD}$-*psl*). One can see in (d) that most of the surface has been covered after a long cumulative time. (e)–(f) show the experimental outcome for 1% arabinose, i.e. high Psl secretion. The visited area fraction is then much smaller and bacteria tend to aggregate mode. Simulations in (g)–(h) show a similar result for a high Psl production ($k = 0.18\,\mathrm{s}^{-1}$, corresponding to 1% arabinose for the mutant $\Delta \mathrm{P}_{psl}/\mathrm{P}_{BAD}$-*psl*). (h) shows that the surface visits and Psl deposition are concentrated over a small surface area and that bacteria accumulate in Psl-rich spots. Taken with permission from [78] 87